PROBABILISTIC ANALYSIS OF AIR VOID STRUCTURE AND ITS RELATIONSHIP TO PERMEABILITY AND MOISTURE DAMAGE OF HOT MIX ASPHALT

A Thesis

by

ADHARA CASTELBLANCO TORRES

Submitted to the Office of Graduate Studies of
Texas A&M University
in partial fulfillment of the requirements for the degree of

MASTER OF SCIENCE

December 2004

Major Subject: Civil Engineering

PROBABILISTIC ANALYSIS OF AIR VOID STRUCTURE AND ITS RELATIONSHIP TO PERMEABILITY AND MOISTURE DAMAGE OF HOT MIX ASPHALT

A Thesis

by

ADHARA CASTELBLANCO TORRES

Submitted to Texas A&M University
in partial fulfillment of the requirements
for the degree of

MASTER OF SCIENCE

Approved as to style and content by:

Eyad Masad (Chair of Committee)	Roger Smith (Member)
Charles Glover (Member)	Paul N. Roschke (Head of Department)

December 2004

Major Subject: Civil Engineering

ABSTRACT

Probabilistic Analysis of Air Void Structure and Its Relationship to Permeability and Moisture Damage of Hot Mix Asphalt. (December 2004)

Adhara Castelblanco Torres, B.S., Universidad Nacional de Colombia

Chair of Advisory Committee: Dr. Eyad Masad

The permeability of hot mix asphalt (HMA) is of special interest to engineers and researchers due to the effects that water has on asphalt pavement performance. Significant research has been done to study HMA permeability. However, most of the studies primarily focused on relating permeability to the average percent air voids in the mix. Such relationships cannot predict permeability accurately due to the different distributions of air void structures at a given average percent of air voids. Air void distribution is a function of many factors such as mix design, compaction method, and aggregate properties. Recent advances in X-ray computed tomography and image analysis techniques offer a unique opportunity to better quantify the air void structure and, consequently, predict HMA permeability.

This study is focused on portraying permeability as a function of air void size distribution by using a probabilistic approach that was previously developed by Garcia Bengochea for soils. This approach expresses permeability as a function of the probability density function (pdf) of the air void size distribution. Equations are derived in this thesis to describe this relationship for laboratory specimens compacted using the

linear kneading compactor (LKC) and Superave^{TM} gyratory compactor (SGC) as well as for field cores (labeled as MS). A good correlation exists between permeability and the pdf of the air voids that formed the flow paths (i.e. connected voids).

The relationship between moisture damage, air void structure, and cohesive and adhesive bond energy is also investigated in this study. Moisture damage is evaluated by monitoring changes in mechanical properties due to moisture conditioning. The influence of air void structure on pore pressure is studied using a recently developed program at Texas A&M University that simulates fluid flow and pore pressure in a porous medium. The surface free energy of the aggregates and asphalt are calculated from laboratory measurements using the Universal Sorption Device (USD) and the Wilhelmy Plate method, respectively, in order to test the compatibility of the aggregates with the asphalt in the presence of water.

DEDICATION

To my beloved parents, Jose Ignacio and Flor Lucia

ACKNOWLEDGMENTS

I would like to express my immense gratitude to my advisor and committee chair, Dr. Eyad Masad, for providing me with the opportunity of participating as a research assistant in this study, and most of all for teaching me and guiding me in the process. His particular enthusiasm and thoughtfulness encouraged me all the way through.

My gratitude is extended to Dr. Roger Smith and Dr. Charles Glover for taking part as my committee members. I give special thanks to Dr. Robert Lytton for his valuable contributions. Their feedback in the final completion of this thesis is greatly appreciated.

I would like to thank Dr. Birgisson from the University of Florida for sharing his results from the experimental measurements of HMA mechanical properties that were conducted at the University of Florida, and most of all, for his useful discussions about these measurements. I would also like to thank my colleagues from TTI from whom I received important feedback.

I am especially grateful with my parents for their support and encouragement. This effort is dedicated to them. Bellatrix and Hector, thanks for standing always by my side.

TABLE OF CONTENTS

Page

CHAPTER Page

LIST OF FIGURES

FIGURE Page

FIGURE Page

LIST OF TABLES

TABLE Page

CHAPTER I

INTRODUCTION

The permeability of hot mix asphalt (HMA) is of special interest to engineers and researchers due to the effects that water has on asphalt pavement performance. Water infiltration within the HMA can cause moisture damage that is manifested in the stripping of the binder from the aggregate. Consequently, it is important to take this property into account to better control the factors that may adversely affect HMA performance.

Al Omari et al. (1), indicated that many empirical relationships have been developed to predict permeability of HMA as a function of percent of air voids only. However, the predictions vary considerably among these models due to the wide variability in the air void structure among these mixes have. Therefore, permeability of HMA would be better predicted if the air void size distribution is taken into consideration. In this study, a probabilistic approach is used to quantify the air void structure and relate it to HMA permeability for different types of mixtures. The air void structure is captured using X-ray computed tomography and analyzed using imaging techniques.

This thesis follows the style of the *Transportation Research Record*.

The influence of air void structure on moisture damage is also investigated in this study. A fracture mechanics framework (2) is used to determine the damage that asphalt mixes experience when they are moisture conditioned. A three dimensional program, that was developed recently at Texas A&M University, is used to simulate fluid flow in three dimensional images of HMA and assess pore pressure distribution. Moisture damage is also attributed to an adhesive and/or a cohesive failure of the pavement structure. Therefore, these cohesive and adhesive bond strengths are measured to have a better understanding of the moisture damage and the factors that can cause it.

Problem Statement

Permeability has significant effects on HMA performance. A number of research studies have been completed to study permeability and many empirical models have been developed to relate permeability to the average percent air voids. However, HMA mixes involve a wide range of aggregate size, and a complex distribution of air voids. Therefore, these models cannot accurately predict permeability based on the average percent of air voids only.

A probabilistic approach for the analysis of air void structure leads to a better understanding of how air void distribution influences permeability of asphalt mixtures. This analysis can be achieved through capturing the microstructure of HMA mixes using X-Ray Computed Tomography (CT) imaging.

Moisture damage in HMA is related to air void structure and surface properties of aggregates and binder. Such relationship needs to be established in order to design asphalt mixes with optimum air void distribution and the least moisture damage.

Objective and Scope

The first objective of this study is to portray permeability as a function of air void size distribution and percent air voids using a probabilistic approach. This objective is achieved by using the Capillary Model developed by Garcia-Bengochea which introduces a pore size parameter that can be calculated from continuous data obtained using X-Ray CT imaging (3).

The second objective is to determine the relationship between the air void distribution, pore pressure distribution, material surface properties and moisture damage. This objective is *achieved* through (1) measurements of surface energy of mixture components to analyze their adhesive and cohesive properties, (2) simulation of pore pressure in the HMA microstructure, and (3) measurements of HMA mechanical properties before and after moisture conditioning.

Organization of the Study

Chapter II documents a review of the empirical and analytical models that have been developed to predict permeability of porous media, and the limitations of these models in predicting HMA permeability. This chapter also includes a description of the X-Ray CT imaging technique that was used in this study to capture HMA microstructure of the specimens used in this research.

Chapter III includes the development of a probabilistic permeability model for HMA. The air void size *distribution* was characterized for laboratory specimens that were compacted using the Linear Kneading Compactor (LKC) and Superpave^{TM} gyratory compactor (SGC), as well as for field cores. The relationship that exists

between different air void distributions and permeability measurements is presented. This is accomplished based on the Capillary model developed by Garcia-Bengochea (3). Two different analyses are considered for this purpose; the first one is taking all the voids into account while the second one is considering the connected voids only.

Chapter IV discusses the influence that air void distribution and pressure distribution have on moisture damage. The analysis in this chapter is done on SGC specimens that were prepared with granite and limestone obtained from the University of Florida. Measurements of their mechanical properties before and after conditioning were used to assess their resistance to moisture damage. A three dimensional program for the simulation of fluid flow was used to calculate pore pressure that water exhorts within the microstructure. Furthermore, results of surface energy testing are presented in order to assess the cohesive and adhesive bonding.

Chapter V summarizes the results of the relationship between permeability and air void size distribution. Also, a summary of the findings in regard to the relation between air void size, pore pressure, material surface properties, and moisture damage of HMA is presented. Recommendations are given in regard to the factors that might affect these results.

CHAPTER II

LITERATURE REVIEW

Description of HMA Internal Structure

An asphalt mixture is a composite material that consists of asphalt binder, aggregates, and air voids. The internal structure (or microstructure) refers to the spatial and directional distribution of these constituents in the mix. The internal structure of an asphalt mixture is influenced by aggregate shape and gradation, asphalt binder content, and the degree and method of compaction.

The internal structure determines the ability of water to infiltrate into the mix, and it also controls the retention of moisture within the mix. Therefore, it is important to capture and quantify the internal structure distribution. They were measured in this study using X-ray computed tomography (CT) and image analysis techniques.

Permeability of Porous Media

Different empirical and analytical models have been developed to describe the permeability of porous media. Usually, permeability is described using the Darcy's coefficient of permeability *k*. This coefficient is derived from Darcy's Law which implies that there is a linear relationship between the discharge velocity and the hydraulic gradient, when the flow is laminar (4). Darcy (1856) observed that the discharge velocity of water through a saturated granular soil can be calculated through the empirical expression (4):

$$v = ki \tag{1}$$

where

v = discharge velocity,

i = hydraulic gradient,

k = coefficient of permeability

Essentially, the discharge velocity v represents the quantity of water that percolates per unit of time across a unit area of a section that is normal to the direction of the flow. The coefficient of permeability k is a measure of the ability of water to infiltrate the porous medium. The hydraulic gradient i is the rate of loss of total head h, between two points that are separated an apparent flow distance s, and can be calculated using the following equation (4):

$$i = -\frac{dh}{ds} \tag{2}$$

It has been recognized that the Darcy's coefficient of permeability of porous media can be calculated based on the assumption of laminar flow (4). This has been confirmed in different numerical simulations of various porous media, and hence it has been implied to be applicable to HMA (1).

Permeability Models for Porous Media

Analytical models have been developed to describe flow through porous media. Bear (5) summarized these analytical models into four categories: capillary tube models, fissure models, hydraulic radius models, and resistant to flow models. These models are based on simplified assumptions regarding the distributions of solids and voids, and shape of

air voids. Therefore, they relate permeability to average parameters that describe the internal structure, such as porosity and average aggregate size, and insert a constant shape factor to fit the data. Consequently, they do not really represent the wide range of void and aggregate sizes that exist and that influence permeability.

These models can be expressed in the following general form, (1):

$$K = f(n) \cdot C \cdot D_s^2 \tag{3}$$

Where, K is the absolute permeability, $f(n)$ is a function of porosity or percent air voids, C is an empirical factor that accounts for the air void distribution, and D_s is the average size of particles in a porous medium. A summary of these models is presented in Table 1. At the same time, the absolute permeability K is related to the Darcy's permeability coefficient k as (1):

$$k = K \frac{\gamma}{\mu} \tag{4}$$

Where, γ is the unit weight of the fluid and μ is fluid viscosity.

TABLE 1 Description of permeability analytical models (5)

Model	Permeability	Constants	Remarks
Capillary tubes	$k=Cn\delta^2$	C=1/32 for 1-D tube	Based on Haggen-Poiseuille's Equation
		C=1/96 for 3-D tube	
	$k=CnD^2\int\delta^2\alpha(\delta)d\delta$	C=1/96 for capillarity in orthogonal direction	Tubes are distributed equally in each orthogonal direction
Fissure	$k= Cnb^2$	C=1/12 for parallel fissures of width b	Applicable to fissured rock
Hydraulic Radius	$k=Cn^3D^2/(1-n)^2$	C=1/180 for spherical particles	Kozeny-Carman equation based on Hydraulic Radius
Resistance to Flow	$k=Cn^2D^2/[(1-n)\lambda]$	$\lambda=3\pi$ for single sphere in infinite fluid, $C=\pi/6$ for spherical particles	Based on Stockes' Equation for drag

n: porosity, δ: air void diameter, λ: factor of packing, D: average particle size

Serial Type Models

In order to overcome the assumption that the pore size is constant throughout the porous medium and also that the capillary tubes are uniformly organized, these models intend to include an additional factor known as tortuosity. The tortuosity factor is the ratio between the length of a flow channel with respect to the length of a straight line distance that goes from the inlet to the outlet of a porous medium. Scheidegger (6) included this tortuosity factor into a model that calculates permeability as:

$$k = \frac{1}{96} \cdot \frac{P\overline{\delta^2}}{T^2} \tag{5}$$

Where, $\overline{\delta}$ is the average pore diameter, T is a tortuosity factor and P is the porosity of the model. Also, according to the model, the porosity factor is defined as:

$$P = \frac{3}{4} \cdot n\pi\overline{\delta^2}\frac{s}{x} \tag{6}$$

Where the factor 3 is introduced by considering that each spatial dimension has n capillaries per unit area; x is the length of the model, and s is the length of the capillary tube. This tortuosity factor was also used by Al-Omari et al (1) in a model that calculated HMA permeability which was determined using X-ray CT.

Network Models

None of the models that have been already mentioned take into account the fact that water can branch out by taking different paths and then converge into the same flow path again. The voids in these networks are represented by the nodes on the network. However, this is not a very accurate representation due to the lack of knowledge of the

microstructure distribution. As such, these models were not successful in obtaining reasonable approximations of permeability. Another shortcoming of these network models is the difficulty of replicating the actual microstructure using an idealized network of channels (6).

Probabilistic Models

All the models that have been described above employ average parameters to describe the internal structure and predict permeability. However, Scheidegger (6) established that the correlation between average parameters with permeability is complex because of the strong dependence of flow rate on the area connectivity, shape and tortuosity of pore paths.

Childs and Collis-George (7), proposed a probabilistic based flow model to quantify the distribution of pores which was later modified by Marshall (8). The model uses pore size distribution to calculate permeability through simplified assumptions in regard to connectivity between adjacent sections: 1) Pore size is considered to be a random variable that can be characterized with a known probability distribution. 2) The overall flow between adjacent sections of the porous media is a function of the number of void pairs that are interconnected, and their sizes. 3) The quantity of flow through the pair of connected voids is restricted by the one with the narrower size; and 4) the connection between any pair of pores in two adjacent sections is totally random. Garcia-Bengochea (3) defined empirical correlations that related a pore size parameter based on probability principles to permeability. Under these assumptions the equation that Childs and Collis-George developed for permeability becomes:

$$k = c\frac{\rho g}{\mu}\sum_{x_i=0}^{x_i=R}\sum_{x_j=0}^{x_j=R}\bar{x}^2 \cdot f(x_i)\Delta x_i \cdot f(x_j)\Delta x_j \quad (7)$$

Where, k is the coefficient of permeability, c is an empirical matching factor that is needed to correct the permeability calculated with the model to the measurement at full saturation; ρ is the density of water, g is the gravitational acceleration, μ is the coefficient of absolute viscosity of water, x_i and x_j are void radii, and $\bar{x}$ is the narrowest radii between x_i and x_j. The terms $f(x_i)\ \Delta\ x_i$ and $f(x_j)\ \Delta\ x_j$ are the fraction of pore space occupied by pores with radii between x_i and $x_i + \Delta\ x_i$ and between x_j and $x_j + \Delta\ x_j$ respectively.

Garcia-Bengochea, defined a pore size parameter (PSP) based on probability principles (3):

$$PSP = \sum_{i}^{n}\sum_{j}^{n}\bar{x}^2 P(x_i)P(x_j) \quad (8)$$

Where, n is the total number of pores, x_i and x_j are random pore diameters, $\bar{x}$ is the smaller pore diameter between x_i and x_j, and $P(x)$ is the volumetric frequency of occurrence of pores with diameter within x and $x+\Delta x$.

Following this, an empirical correlation between permeability k and PSP was defined by inserting a shape factor C_s (3).

$$k = C_s \cdot PSP \quad (9)$$

To overcome the empiricism of this expression, Juang and Holtz (9), developed a new model for permeability as a function of the pore size density function, which was

measured from mercury intrusion. By considering a section of a porous medium with thickness Δy, and assuming that its cross sections have identical pore size density functions then, the probability $P(x_i, x_j)$, that pores within diameters x_i to $x+dx_i$ on cross section i, are connected to pores on cross section j within diameters x_j to $x+dx_j$, has two extreme cases:

1) If $\Delta y >> x$, the connection of voids on the adjacent cross sections can be assumed as being completely random. Therefore:

$$P(x_i, x_j) = f(x_i)\, f(x_j)\, dx_i\, dx_j \tag{10}$$

2) If $\Delta y \rightarrow 0$, the connection of voids on the adjacent cross sections is assumed to be completely correlated. Thus:

$$P(x_i, x_j) = f(x_i)\, dx_i = P(x_i) \quad \text{or} \quad P(x_i, x_j) = f(x_j)\, dx_j = P(x_j) \tag{11}$$

Where, $f(x)$ is the pore size density function of the porous medium. Juang and Holts (9) developed Equation 12, for the intermediate case between completely correlated and uncorrelated cases:

$$k = \frac{\rho g n^2}{32\mu} \int_0^\infty \int_0^\infty \overline{x^2} \cdot g(y, x_i, x_j) \cdot f(x_i) \cdot f(x_j) \cdot dx_i \cdot dx_j \tag{12}$$

Where $g(y,x_i,x_j)$ is a connecting function, y is a variable that accounts for tortuosity of flow and $\bar{x}$ is the smallest between x_i, x_j; and $f(x)dx$ represents the proportion of the total pore volume of voids within a diameter range of x and $x+dx$.

Permeability Anisotropy

Permeability anisotropy indicates that the material exhibits different permeability values depending on direction. Permeability anisotropy occurs in a porous medium such as HMA, due to the directional distribution of aggregates and air voids.

Al-Omari and Masad (10) developed a three dimensional fluid flow model to calculate HMA permeability by capturing the microstructure using X-ray CT images. The anisotropy of permeability can be calculated by applying pressure gradients in different directions and calculating the permeability coefficients in these directions.

Moisture Damage

HMA moisture damage is caused by the infiltration of water into the internal structure and moisture susceptibility of the mixture. Moisture damage can be caused by a cohesive failure when the asphalt binder separates or by an adhesive failure when the linkage between the aggregate and the asphalt binder breaks down (2).

The adhesive resistance of a mix depends on the bonding strength between the aggregate and the asphalt binder. If this bond is weak, a failure will occur at the aggregate-asphalt interface; this is commonly known as stripping (11). There are different ways to mitigate stripping of asphalt pavements. Firstly it is important to provide adequate drainage to the pavement structure so that moisture will not remain within the internal structure. Poor compaction is another issue that should be addressed because it can facilitate the penetration of moisture into the mix (11).

In order to obtain a mixture that is not susceptible to stripping, there has to be chemical compatibility between the aggregate and the asphalt binder. Some aggregates

are more susceptible to stripping because of their chemical composition. Siliceous aggregates such as granite and sandstone have been categorized as hydrophilic because they tend to strip much more easily than carbonate aggregates such as limestone (12).

Lytton (13) reported on the surface energy of different binders and aggregates. He demonstrated the importance of selecting aggregates and binder that are compatible in terms of surface energy in order to provide adequate cohesive and adhesive bond strengths in the mix. Lytton (13) presented the methods to calculate the bond energy necessary to resist fracture and the bond energy needed for crack healing. Lytton (13) also linked moisture damage to the asphalt film thickness which is a function of the aggregate properties and mix design.

CHAPTER III

MICROSTRUCTURAL ANALYSIS TO CHARACTERIZE AIR VOID SIZE DISTRIBUTION

Introduction

Scheiddeger (6) developed a definition for the air void size at a given point of the microstructure that could be used to mathematically interpret the pore size distribution as well as its density function. He believed that the pore diameter at any point within the pore space is a random variable and considered it as the largest sphere that holds this point and nonetheless remains entirely inside the pore space. In this way, a pore diameter x, could be assigned to each point within the pore space, and the air void diameter distribution can be established by determining the respective fraction of the pore space that is composed of air void diameters between x and $x + dx$.

Numerous methodologies have been used to characterize the air void size distribution of porous media. These methods include: a) application of probability theory to indirectly determine the air void distribution from a representative grain size distribution; b) scanning electron microscopy techniques; c) capillary suction methods; and d) mercury intrusion techniques. However, the latter was most frequently used to determine the pore size distribution because of its appropriateness (9). This procedure consisted of intruding a non-wetting liquid (mercury) into the porous medium. The surface tension of this liquid resists the entry of the liquid into the pores. Washburn (14)

noticed that this tension could be overcome by an external pressure that is inversely proportional to the diameter size of the pore being intruded. With the powerful features of X-Ray CT imaging techniques, the microstructure of porous media such as HMA can be digitally captured in a three dimensional fashion (15).

Overview of X-Ray Computed Tomography (CT) Imaging

The X-Ray CT imaging technique consists of studying the interior of opaque solid objects in a non-destructive fashion. Two dimensional images or most commonly known as "slices" can be obtained through this process. Each slice reveals the interior of the object on a plane, and if stacked together, the slices can build a three dimensional image of the object. These slices are generally about 1 mm in thickness with an overlap of 0.2 mm in between (15).

The X-Ray system is composed of an X-ray source, a turntable to hold the sample, and a detector. 1 shows a schematic of the system. The source emits X-rays that pass through the solid object while it rotates horizontally. After each complete rotation, an image is produced from the different density measurements that are registered, and are represented by a grey scale.

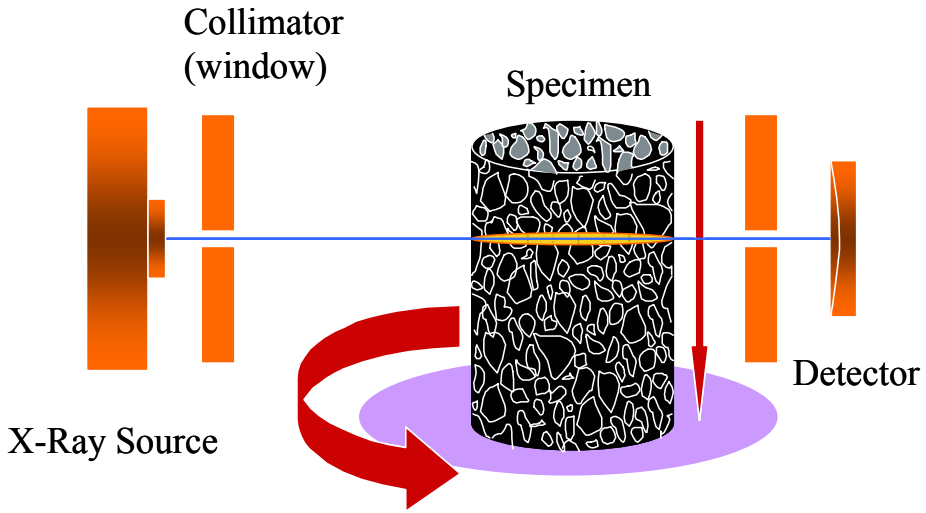

Figure 1 Schematic of the X-ray CT scanner.

Subsequent to scanning each slice, the turntable is shifted downwards, by a fixed distance which is equivalent to the resolution in that direction. The whole procedure is repeated once again to produce the next image, until the whole solid is scanned.

An important issue to take into account when using X-ray CT images is the resolution at which they are taken (number of pixels per unit length of the longitudinal image dimension). The resolution is affected by several factors such as the type and size of the X-ray source and detectors, the distance between the source, the solid and the detector, and the method used for image reconstruction. The image reconstruction consists of representing the object in a grid of picture elements (pixels) if using two dimensions, or volume elements (voxels) if using three dimensions.

The images that were analyzed varied in resolution. The images of the laboratory LKC cores were taken at a resolution in the range of 0.146 to 0.195 mm/pixel. The resolution of the field cores was not the same for all specimens due to

the difference in size (i.e. 0.092, 0.142, 0.186, and 0.195 mm/pixel), and the SGC cores were scanned with a resolution of 0.195 mm/pixel. These images are captured in a grey scale that consists of 256 levels; each level corresponds to a density within the core. Air voids have the lowest intensity of all and are shown in black, which corresponds to level zero.

Description of Mixes

Three sets of specimens were used to find the relationship between the pore size distribution and the permeability. These specimens were categorized as: 1) laboratory specimens compacted using Linear Kneading Compactor (LKC), 2) field cores (MS), and 3) laboratory specimens compacted using Superpave^{TM} Gyratory Compactor (SGC). Details about these mixtures are described in the following sections.

Laboratory Specimens Compacted Using Linear Kneading Compactor (LKC)

The laboratory specimens were prepared with two different types of aggregates, gravel and limestone. The gravel mix had a nominal maximum aggregate size (NMAS) of 12.5 mm, whereas three different mixes were prepared with the limestone having NMAS of 12.5 mm, 19.0 mm, and 25.0 mm, respectively. The samples were cored from slabs with different thicknesses prepared with the Linear Kneading Compactor (LKC). Permeability measurements for these mixes were obtained using the Karol Warner permeameter which is based on the falling head method (16). The properties of these mixes are summarized in Table 2 and Table 3.

TABLE 2 Properties of LKC mixes

Mix	LS12.5	LS19.0	LS25.0	GV12.5
Aggregate	Limestone	Limestone	Limestone	Gravel
NMAS (mm)	12.5	19.0	25.0	12.5
Binder Content (%)	5.4	4.6	4.1	5.9
Maximum Specific Gravity (G_{mm})	2.480	2.512	2.529	2.478

TABLE 3 Permeability and percent air voids of laboratory LKC specimens

Label	Permeability k (10^{-5} cm/s)	% Air Voids n
GV-12.5-76	223	9.18
GV-12.5-79	2049	13.70
GV-12.5-81	6553	14.65
GV-12.5-84	9850	17.37
LS-12.5-79	2984	13.10
LS-12.5-81	1137	11.65
LS-12.5-90	24525	18.83
LS-12.5-83	7949	15.44
LS-25.0-79	1746	14.27
LS-25.0-84	8716	15.38
LS-25.0-91	32350	20.01
LS-19.0-72	0	5.73
LS-19.0-74	0	5.73

Field Cores

The field cores were obtained from seven HMA pavements from different aggregate sources that included NMASs of 9.5, 12.5 and 19.0 mm. The gradation of these specimens passed above or below the restricted zone. In-place permeability of these cores was measured with the national Center for Asphalt Technology field permeability device. The percent air voids were measured using the Corelock device. More

information on these measurements is given by Al-Omari et al. (1). The properties of these mixes are summarized in Table 4 including the percent air voids and permeability data.

TABLE 4 Properties of field core mixes

Label	Gradation	NMAS (mm)	Permeability k (10^{-5} cm/s)	% Air Voids n
MS1 - 1	Above	12.5	697	13.90
MS1 - 4	Above	12.5	10	6.60
MS1 - 6	Above	12.5	37	7.00
MS1 - 7	Above	12.5	1	4.40
MS1 - 8	Above	12.5	1	5.60
MS2 - 6	Below	12.5	0	5.30
MS2 - 7	Below	12.5	49	9.50
MS2 - 9	Below	12.5	76	7.10
MS2 - 11	Below	12.5	119	6.90
MS4 - 7	Below	9.5	120	8.80
MS4 - 11	Below	9.5	54	8.20
MS4 - 14	Below	9.5	291	9.00
MS5 - 1	Below	19.0	3333	7.40
MS5 - 3	Below	19.0	30	5.40
MS5 - 4	Below	19.0	348	8.50
MS5 - 11	Below	19.0	4960	10.60
MS5 - 12	Below	19.0	244	7.20
MS6 - 6	Above	19.0	269	8.70
MS6 - 7	Above	19.0	1386	11.00
MS6 - 8	Above	19.0	656	9.60
MS6 - 13	Above	19.0	1	6.00
MS6 - 14	Above	19.0	178	7.50
MS7 - 3	Below	9.5	0	4.70
MS7 - 6	Below	9.5	28	7.20
MS7 - 9	Below	9.5	527	10.60
MS7 - 13	Below	9.5	327	9.50
MS8 - 10	Below	19.0	13477	10.60
MS8 - 11	Below	19.0	16307	9.60
MS8 - 12	Below	19.0	1619	7.60
MS8 - 13	Below	19.0	17789	12.60

Laboratory Specimens Compacted Using Superpave™ Gyratory Compactor (SGC)

These specimens were obtained from two different studies on moisture susceptibility conducted at the University of Florida by Birgisson, Roque and Page (2), (17). The specimens were prepared using granite aggregate from Georgia and limestone aggregate from Florida. These two types of aggregates are commonly used throughout Florida. Experience has shown that the limestone does not have significant potential for stripping whereas the granite does. The limestone and granite mixes will be denoted hereafter as WR and GA, respectively.

Both types of mixes were prepared with coarse aggregate, fine aggregate, screenings, and mineral filler that were blended together in different proportions to make six different HMA mixtures, respectively. A limestone mixture that was previously designed by Florida Department of Transportation (FDOT) was used to produce a coarse-graded (C1) and fine-graded mixtures (F1). The coarse gradation refers to passing below the restricted zone, while the fine gradation refers to passing above the restricted zone. Two more gradation designs were used by varying the coarse and fine proportions of the original mixture. Hence, six limestone mixtures of 12.5-mm nominal maximum aggregate size were prepared, three of them from the coarse gradation (C), and the other three from the fine gradation (F): C1, C2, C3, F1, F2, F3/C4. The dual designation of F3/C4 was used to indicate that the gradation was adjusted to fall under the restricted zone with the purpose of having a higher permeability. The volumetric properties of these mixtures are summarized in Table 5. The six granite mixtures were

of 12.5-mm nominal maximum aggregate size, three of them have coarse gradations (GA-C1, GA-C2, GA-C3), and the other three, have fine gradation, (GA-F1, GA-F2, GA-F3). All specimens were prepared to 7% target percent air voids. The properties of these mixtures are given in Table 6.

TABLE 5 Volumetric properties of limestone SGC specimens

Specimen	WR-C1	WR-C2	WR-C3	WR-F1	WR-F2	WR-F3/C4
Binder Content	6.5	5.8	5.3	6.3	5.4	5.6
Specific gravity of Asphalt	1.035	1.035	1.035	1.035	1.035	1.035
Bulk Specific Gravity	2.235	2.255	2.254	2.244	2.281	2.244
Voids in Mineral Aggregate (%)	15.4	13.8	13.6	15.6	13.2	14
Voids filled with Asphalt (%)	74.1	71.6	70.2	74.2	70.1	71.9
Effective specific gravity of aggregate	2.549	2.545	2.528	2.554	2.565	2.537
Effective asphalt (%)	5.3	4.6	4.5	5.3	4.2	5.5
Theoretical Film Thickness (microns)	11.2	10.1	8.0	9.0	6.9	8.1
Percent of air voids	4.0	3.9	4.0	4.0	3.9	3.9
Permeability (10^{-5} cm/s)	72.37	64.24	29.39	69.63	17.81	9.68
Surface area (m^2/kg)	4.87	4.64	5.68	6.05	6.31	5.64

TABLE 6 Volumetric properties of granite specimens

Specimen	GA-C1	GA-C2	GA-C3	GA-F1	GA-F2	GA-F3
Binder Content	6.6	5.3	5.3	5.7	4.6	5.1
Specific gravity of Asphalt	1.035	1.035	1.035	1.035	1.035	1.035
Bulk Specific Gravity	2.345	2.399	2.391	2.374	2.433	2.404
Voids in Mineral Aggregate (%)	18.5	15.4	15.7	16.6	13.6	15.1
Voids filled with Asphalt (%)	78.5	73.8	74.2	75.9	71.2	73.3
Effective specific gravity of aggregate	2.710	2.719	2.709	2.706	2.725	2.720
Effective asphalt (%)	6.3	4.9	5.0	5.4	4.1	4.6
Theoretical Film Thickness (microns)	19.9	14.3	12.1	13.4	7.7	9.9
Percent of air voids	4.0	4.0	4.1	4.0	3.9	4.0
Permeability (10^{-5} cm/s)	67.50	59.00	56.00	25.33	9.33	34.25
Surface area (m^2/kg)	3.30	3.50	4.20	4.10	5.30	4.90

Overall, the six mixtures of each type of aggregate can be categorized as fine uniformly-graded and fine dense-graded to coarse uniformly-graded and coarse gap-

graded; the corresponding nomenclature of the limestone and granite specimens, coincides with approximately the same gradation (2), (17). The purpose of varying the gradation was to obtain mixtures of different permeability and other volumetric properties but with the same aggregate type, to test the influence of these factors on moisture damage. Following Superpave^{TM} volumetric mix design specifications, the content of asphalt was determined for each mixture by targeting the air void content to 4% at N_{design} of 109 gyrations. The asphalt used was determined to be PG 67-22 (AC-30).

For each mixture, 3 samples were conditioned, according to AASHTO T-283. The SuperPave^{TM} IDT was used to test unconditioned (U) and conditioned (C) samples to measure resilient modulus, creep compliance, and strength. The tensile strength, resilient modulus, fracture energy limit (FE), and creep properties (D_1 and m-value) were determined from these tests. All this data is summarized in Tables 7 and 8. More details about these tests are given in references (2) and (17).

TABLE 7 Mechanical properties of limestone SGC specimens

Label	Property						
	Resilient Modulus (Gpa)	Creep compliance at 100 seconds (1/Gpa)	Tensile Strength (Mpa)	Fracture Energy (kJ/m^3)	Failure Strain (10^{-6})	m-value	D_1
Temperature: 10 °C							
WR-C1 (C)	7.00	1.71	1.33	2.20	2017.0	0.44	1.50E-06
WR-C2 (C)	7.35	2.45	1.27	1.90	1766.0	0.59	1.03E-06
WR-C3 (C)	9.96	1.09	1.62	1.60	1259.0	0.54	5.75E-07
WR-C1 (U)	8.53	1.74	1.59	2.50	1939.0	0.54	9.51E-07
WR-C2 (U)	8.66	2.46	1.28	1.90	1702.0	0.67	7.65E-07
WR-C3 (U)	10.97	0.78	1.92	2.00	1320.0	0.43	7.84E-07
WR-F1 (C)	6.17	3.68	1.56	4.20	3270.0	0.73	9.13E-07
WR-F2 (C)	5.59	3.02	1.56	3.10	2674.7	0.67	9.49E-07
WR-F3 (C)	9.45	1.44	1.77	1.90	1366.0	0.69	4.08E-07
WR-F1 (U)	6.08	3.42	1.57	4.20	3269.0	0.60	1.16E-06
WR-F2 (U)	8.13	1.74	1.81	3.10	2114.0	0.54	1.01E-06
WR-F3/C4 (U)	9.67	1.28	1.98	2.70	1685.0	0.53	7.08E-07

TABLE 8 Mechanical properties of granite SGC specimens

Label	Property						
	Resilient Modulus (Gpa)	Creep compliance at 100 seconds (1/Gpa)	Tensile Strength (Mpa)	Fracture Energy (kJ/m^3)	Failure Strain (10^{-6})	m-value	D_1
Temperature: 10 °C							
GA-C1 (C)	4.08	4.42	1.12	2.90	3350.1	0.66	1.54E-06
GA-C2 (C)	8.35	2.84	1.84	2.80	2055.8	0.65	1.03E-06
GA-C3 (C)	9.07	2.75	1.77	2.10	1610.9	0.6	9.10E-07
GA-C1 (U)	5.1	4.12	1.44	6.00	4763.8	0.62	1.74E-06
GA-C2 (U)	8.79	2.16	2.00	5.00	3122.0	0.59	1.06E-06
GA-C3 (U)	9.99	1.47	1.99	3.80	2406.3	0.57	8.70E-07
GA-F1 (C)	7.05	2.89	1.59	2.80	2145.1	0.63	1.52E-06
GA-F2 (C)	10.1	1.92	1.96	2.30	1351.3	0.56	1.24E-06
GA-F3 (C)	8.14	2.28	1.75	2.10	1638.4	0.6	1.44E-06
GA-F1 (U)	8.45	1.93	1.93	3.70	2428.4	0.57	1.30E-06
GA-F2 (U)	10.2	2.52	2.52	3.60	1803.8	0.48	1.58E-06
GA-F3 (U)	9.95	2.14	2.14	2.80	1757.2	0.56	8.97E-07

Air Void Distribution Results Using X-ray CT Imaging

As described in the previous section, X-ray CT images are produced in a grey scale. To analyze the images, they have to be transformed into a binary format such that the voids can be isolated from the rest of the solids (mastic and aggregates). By doing so, the grey images were transformed such that air voids appeared in black, and all other phases appeared in white. This procedure was done by setting a threshold value of grey intensity such that every pixel with an intensity value above threshold is turned to black and every pixel with an intensity value below the threshold is turned to white.

This threshold was chosen by finding an intensity value such that the percent air voids calculated from the 3-D image matches the measured one. The air void content was measured using the Corelock device for the field and LKC laboratory specimens, and the AASHTO T166 method was used for the SGC granite and limestone specimens.

Figure 2 shows a sample of how a thresholded image on the right looks in comparison to the original grey scale image on the left. It is remarkable how close the air voids can be identified in the binary format. Hence, it is important to rely on accurate measurements of percent air voids as that will affect the appearance of the transformed image and, the calculations based one on the images will be influenced as well.

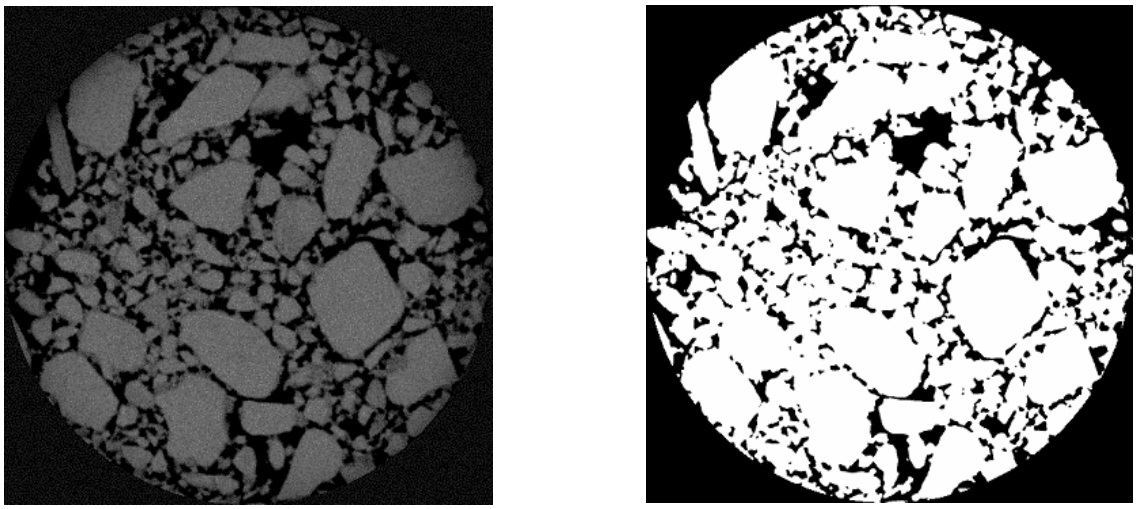

(a) **(b)**

Figure 2 X-ray CT images of an LKC specimen: (a) grey scale image, and (b) thresholded image.

The procedure followed to analyze air void size distribution on the images consisted of preparing a macro written in IPBasic which is a built in language of ImagePro Plus (18). The purpose of this macro is to load the whole set of images and quantify for each of them the area of each air void within the image according to its resolution. Subsequently, the macro calculates an equivalent diameter of each air void by assuming that they have a circular shape. Therefore the output obtained is the whole set of diameters of air voids that exist within a specimen. This data was then used afterwards to determine the air void size distribution for each of the specimens.

As mentioned in the literature review, the permeability models do not account for the great variability of air void sizes that exist within the specimen. This variability is reflected in the porosity on each image of the specimen. It can be seen in Figure 3 that the difference in percentage of air voids along the specimen is remarkable for different

aggregate types (gravel GV and limestone LS), having different nominal maximum aggregate size (NMAS), even though both were compacted with LKC. When comparing these air void distributions with their respective percentage of air voids consigned in Table 3, it becomes meaningful that disaggregate data about the air void content is more significant than an aggregate value for the specimen.

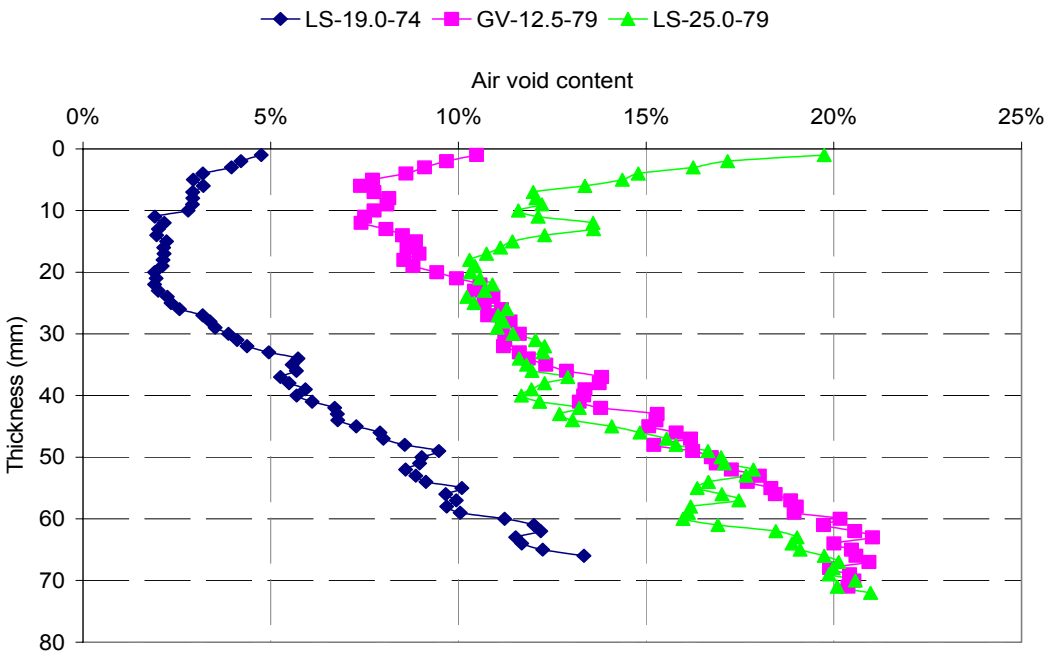

Figure 3 Difference in air void content with thickness for LKC cores.

Figure 4 shows that the porosity of the field cores changes greatly along the thickness of the specimen in regard to the NMAS as observed with the LKC cores, having in particular more air voids toward the top and bottom parts of the specimen. Even though MS5-4 and MS4-7 have a similar percentage of air voids, (i.e. 8.5% and

8.8% respectively), their distribution is different. On the other hand, MS1-1 is shifted to the right because its air void content is greater (13.9%). These details are difficult to capture with a measurement of air void content only.

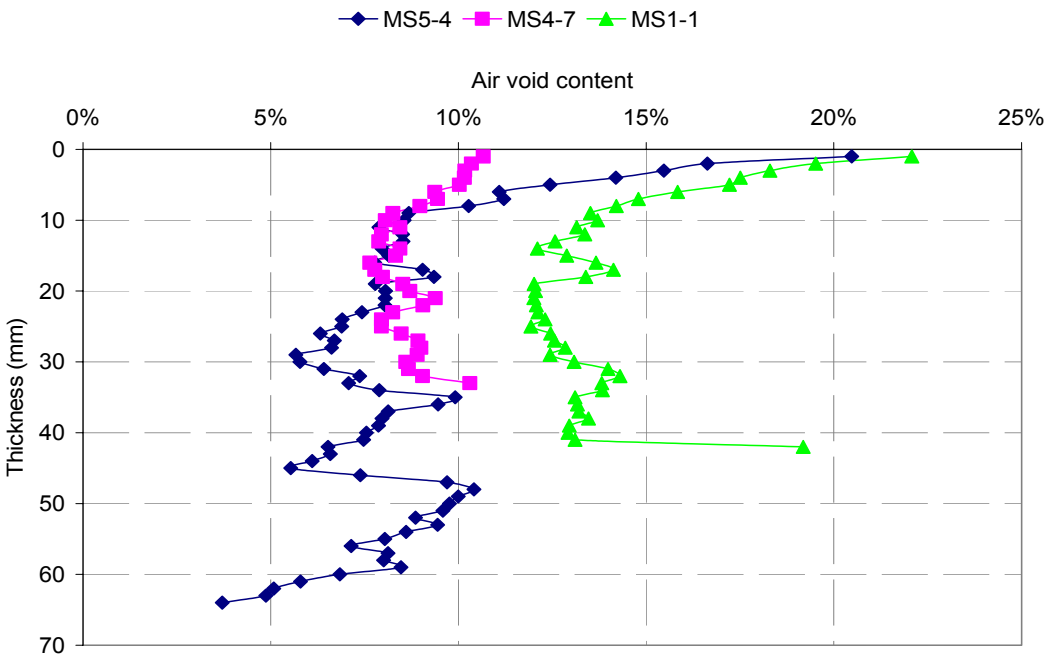

Figure 4 Difference in air void content with thickness for field cores.

The variability of the air void distribution along the thickness of the SGC specimens is also remarkable, as shown in Figures 5 and 6. Even though, these mixtures were compacted using the same method, and they exhibit a common profile distribution of air void content (i.e. more air voids in the top and in the bottom, with generally lower values in the remainder of the specimen), the type of gradation makes a difference. This can be seen in Figures 5 and 6 which show a comparison between the air void

distribution profile for a coarse gradation and a fine gradation for limestone and granite respectively.

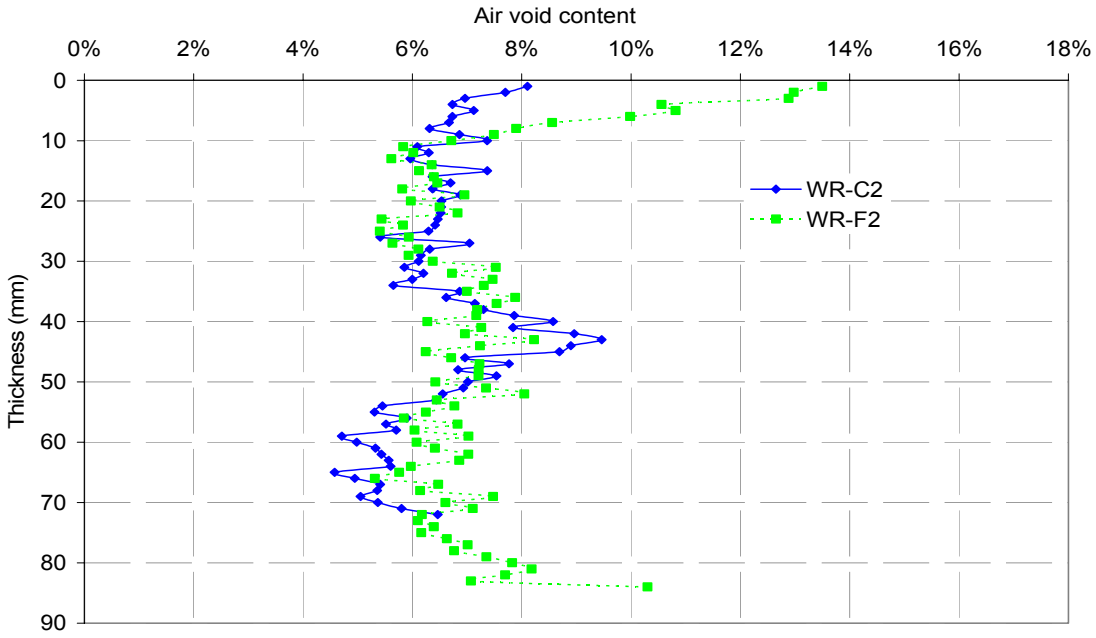

Figure 5 Difference in air void content with thickness for SGC limestone cores.

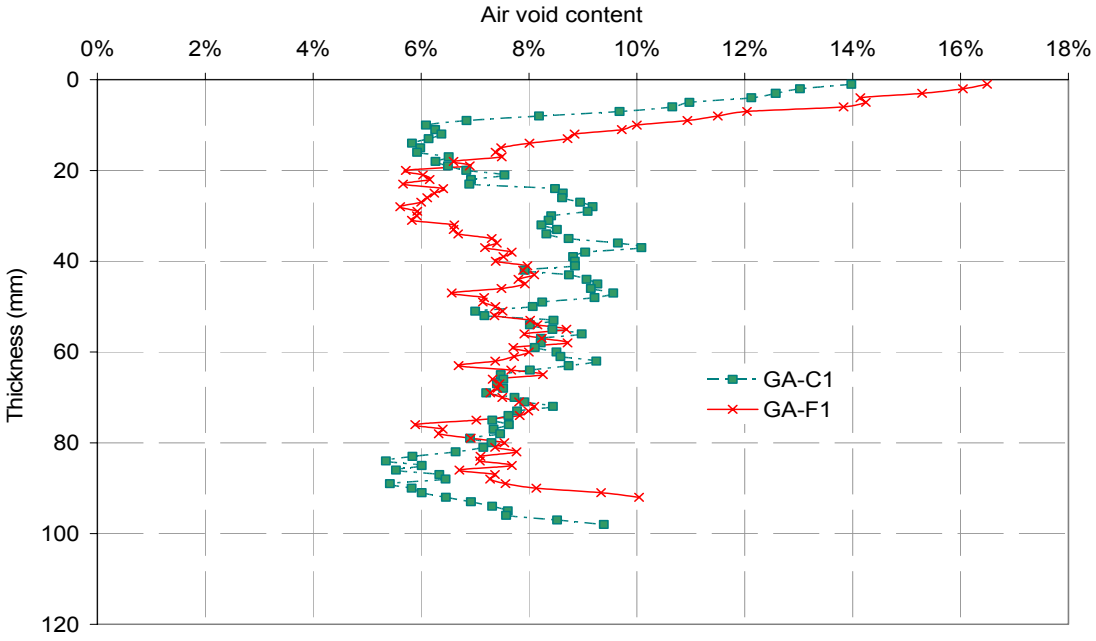

Figure 6 Difference in air void content with thickness for SGC granite cores.

Probabilistic Analysis of Air Void Size and Permeability

The variable diameter capillary model developed by Garcia-Bengochea was used to predict the permeability of the LKC and the field specimens respectively (3). This model is based on a probabilistic approach because it relates the air void size distribution to permeability. Garcia-Bengochea approximated the air void size distribution in a discrete form by measuring the volume of void space occupied by voids within a certain size range. These measurements were conducted using the mercury intrusion technique (3).

This model was applied using the assumption that the probability that air voids on two adjacent sections, or slices of the specimen, are connected is completely

correlated. This assumption was adopted because of the very small distance (i.e. 0.8 mm) between adjacent sections that were captured in the testing. This assumption matches with the extreme case described by Juang and Holtz (9). The permeability is expressed using the Garcia-Bengochea equation as:

$$k = C_s n \sum_i P(x_i) x_i^2 \tag{13}$$

where

k = permeability,

C_s = Shape factor,

n = Porosity or percent air voids,

$P(x_i)$ = volumetric frequency of occurrence of pores with diameters between x_i and dx_i.

From a probabilistic stand point, the summation term is known as the second moment about the origin of the pore size distribution, and it is equivalent to the expected value of the diameter squared, $E(x^2)$. Also, the summation of the volumetric frequency of occurrence is equal to one as expressed in Equation 14. The pore size volumetric frequency can be calculated once the pore size distribution is known.

$$E(x_i^2) = \sum_i P(x_i) x_i^2 \qquad \textit{and} \qquad \sum_i P(x_i) = 1 \tag{14}$$

According to Equation 14 and by substitution in Equation 13, the permeability can be expressed as the product of a shape factor and a pore size parameter (3):

$$\mathrm{k} = \mathrm{C_s PSP}, \qquad \mathrm{PSP} = \mathrm{nE(x^2)} \tag{15}$$

Where, PSP is the pore size parameter that is related to the pore size distribution.

X-ray CT Image analysis allows performing air void measurements in a precise way by measuring continuous data. Hence, the summation in Equation 14 is replaced by an integral over all the diameter sizes. It corresponds to the area under the curve of the product of the diameter squared and the probability density function $f(x_i)$, of a known distribution that fits the pore size data. This can be mathematically expressed as:

$$k = C_s n \int_{d_{\min}}^{d_{\max}} x_i^2 f(x_i) dx = C_s n E(x^2) dx \tag{16}$$

The probability density function was determined by plotting the pore size cumulative probability versus the cumulative probability of a test distribution. These plots are most commonly known as "probability plots" and are available from statistical packages (19). Figure 7 shows an example of the probability plots for an LKC core tested using Weibull and Lognormal distributions. If the distribution of the data matched the test distribution, the data points should cluster around the equality line.

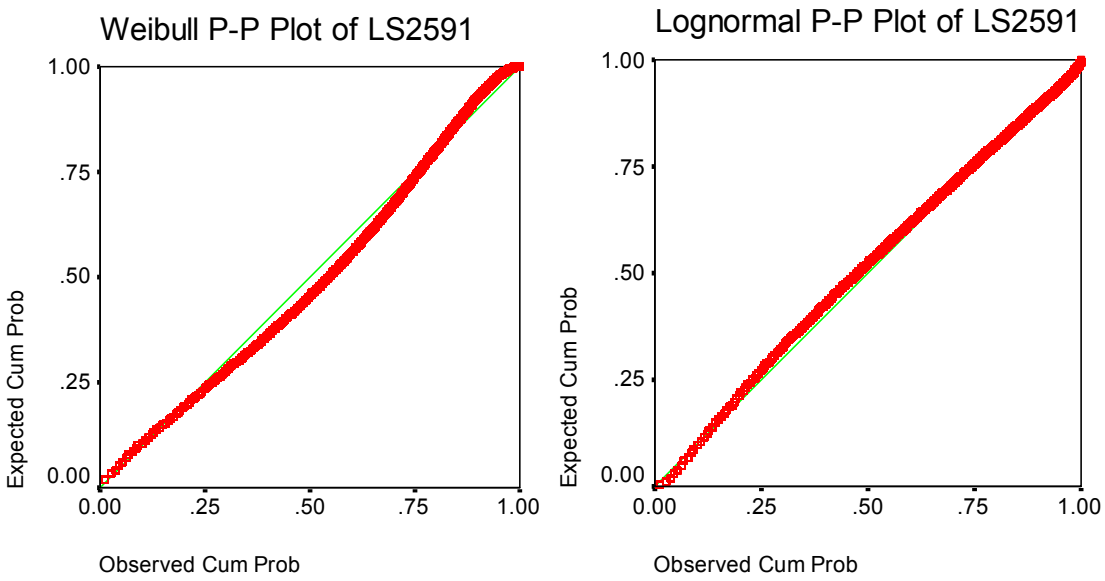

(a) (b)

Figure 7 Examples of probability plots for an LKC core: a) Weibull distribution, and b) Lognormal distribution.

The Pearson correlation coefficient was used to establish the degree of linearity between the cumulative probability of the data and the test distribution. The closer this coefficient is to one, the better the correlation between the two cumulative probabilities is, and thus, the distribution fits the data (19).

According to the probability plots and the Pearson correlation coefficients, there were two distributions that fitted the data the best, Lognormal and Weibull distributions with Pearson correlation coefficients between 0.94 and 0.99. Both of these density functions were used thereafter for the analysis.

The density function of the lognormal distribution is expressed as (20):

$$f(x) = \frac{1}{\sigma \cdot x \cdot \sqrt{2\pi}} \cdot \exp\left(\frac{-(\ln x - \mu)^2}{2 \cdot \sigma^2} \right) \tag{17}$$

where

x = air void diameter,

μ = location parameter,

σ = scale parameter

A lognormally-distributed random variable implies that the logarithm of it is normally-distributed. The location parameter μ can be any real number whereas the scale parameter σ can only be a positive real number. This type of distribution is commonly used to model continuous random data when the distribution is thought to be skewed. The form of the lognormal distribution is skewed to the right; and for a given μ the skewness increases as σ increases.

The density function of the Weibull distribution expression is (20):

$$f(x) = \frac{\beta}{\alpha^{\beta}} \cdot x^{\beta-1} \cdot \exp(-(x/\alpha)^{\beta}) \tag{18}$$

where

α = Scale parameter,

β = Shape parameter

As the shape parameter, β, increases, the peak at the mode becomes larger. Similarly, the random variable x has this distribution if x^{β} is exponentially distributed. Both of these distributions are commonly used to model continuous data, and they are broadly used because of the wide range of shapes that they can take.

The density functions of these distributions were multiplied by the pore diameter squared x_i^2 and integrated to calculate the expected value of the diameter squared as it is

expressed in Equation 16. This integration was numerically calculated by using a macro written in Maple (21). The input to the macro are the parameters of the probability density function (i.e. location, μ, scale, σ, or shape, β) and the minimum and maximum pore diameters (x_{min}, x_{max}) extracted from the image analysis software Image-Pro Plus (18). Consequently, the pore size parameters were calculated by multiplying the integral results by the percent air voids of each core as shown in Equation 15.

Garcia-Bengochea (3) found that when plotting the permeability and the pore size parameter on a logarithmic scale with the permeability as the dependent variable, a linear trend could fit the data. Hence, the relation between permeability and pore size parameter could be expressed as:

$$\text{Log } k = m \log PSP + b \tag{19}$$

Thus, this is the equation of a straight line with *Log k* as the dependent variable, and regression parameters *m,* and *b,* obtained from the fitted curve. Equation 19 can also be written as:

$$k = 10^{b} (PSP)^{m} \tag{20}$$

Equation 20 is equivalent to Equation 15 when $C_s = 10^b$ and $m=1$. The shape factor, C_s, is included in order to account for the effect of the fluid properties, as well as the shape of the voids. This can be seen from the Hagen-Poiseuille equation (4). Figures 8 to 11 show the results of the regression analysis for the LKC and field specimens for the two types of distributions.

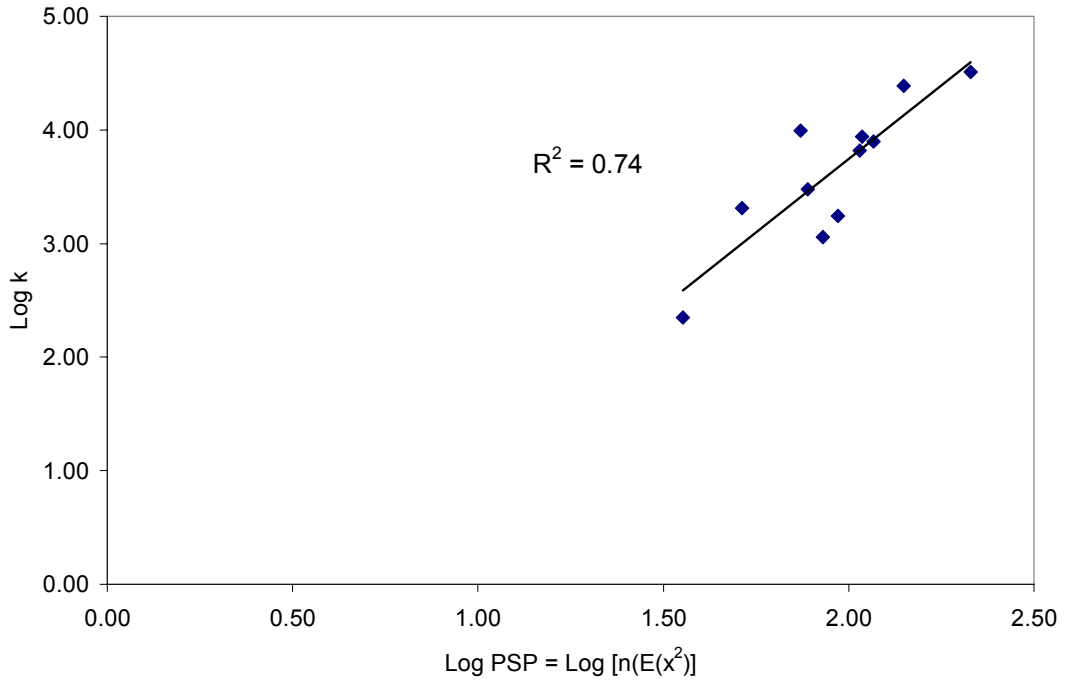

Figure 8 Permeability vs. PSP using Lognormal distribution for LKC specimens.

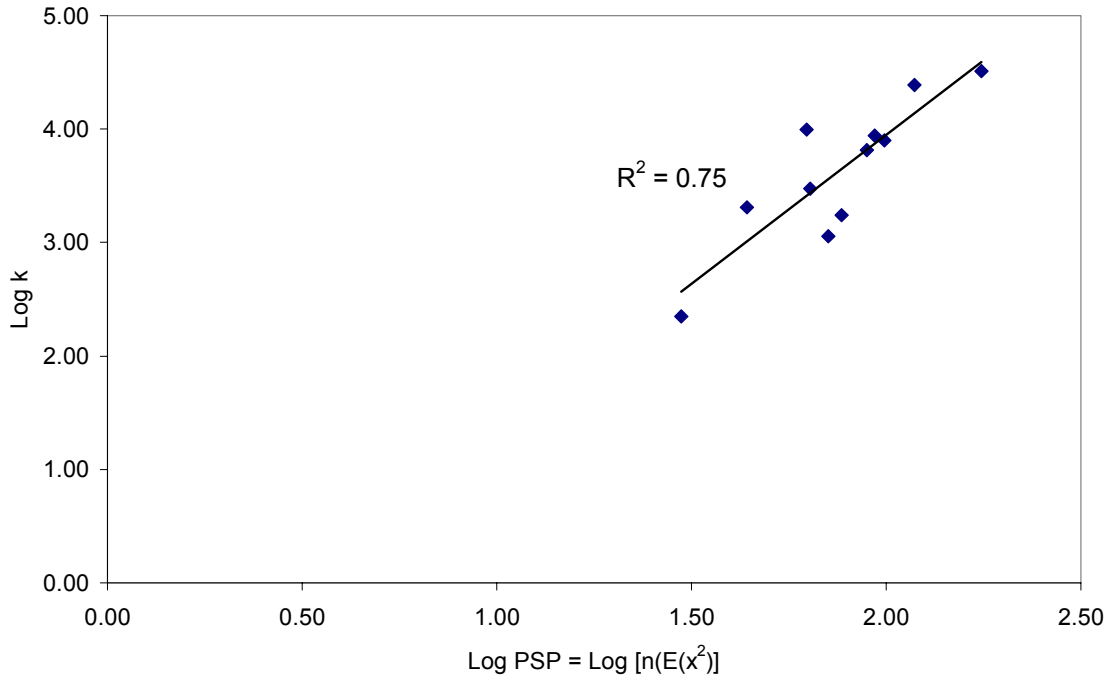

Figure 9 Permeability vs. PSP using Weibull distribution for LKC specimens.

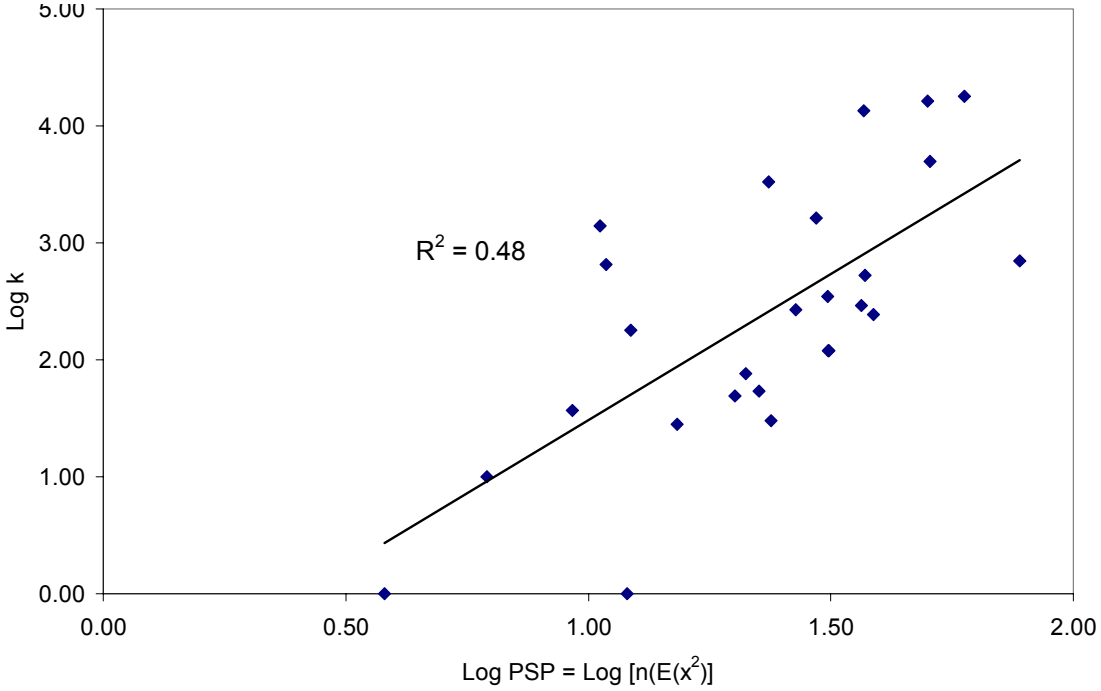

Figure 10 Permeability vs. PSP using Lognormal distribution for field specimens.

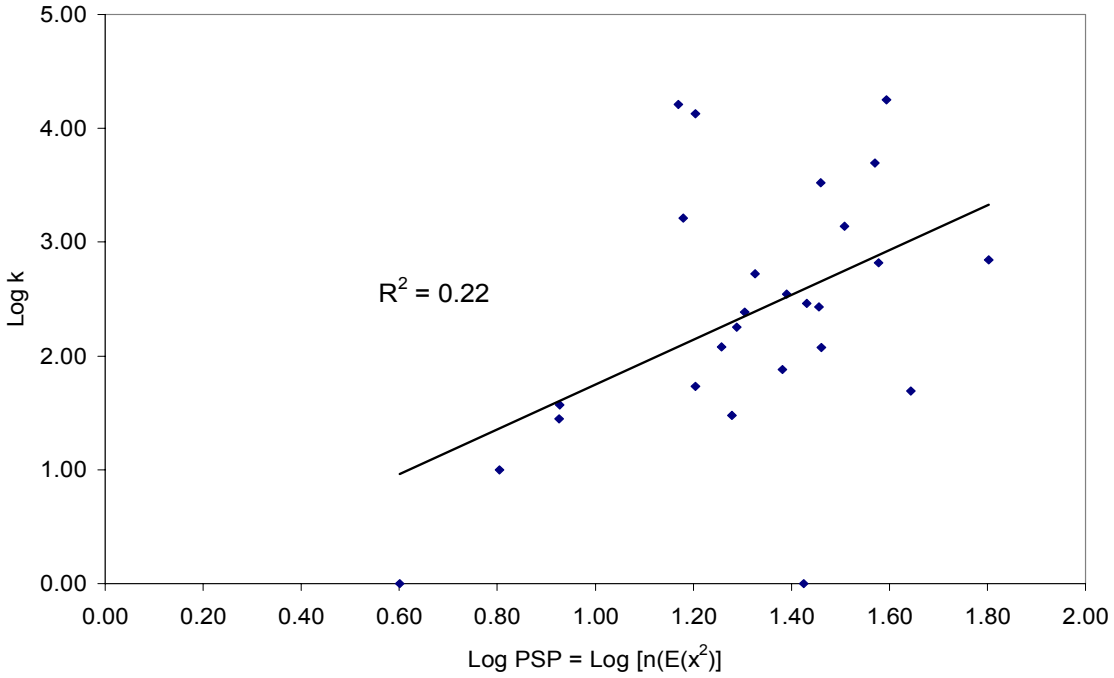

Figure 11 Permeability vs. PSP using Weibull distribution for field specimens.

The correlation coefficients from the regression analysis between the permeability and the pore size parameter in Logarithmic scale are fairly good for the LKC specimens (74% and 75% for lognormal and Weibull distributions, respectively). However, the results are not compelling for the field cores (48% and 22% for Lognormal and Weibull distributions respectively).

Tables 9 and 10 include the summarized data for the two distributions when analyzing LKC specimens while Tables 11 and 12 include the same data for the field specimens.

TABLE 9 PSP calculation for Lognormal distribution and laboratory specimens

Label	Measured Permeability (k) 10^{-5} cm/s	Distribution Parameters		Diameters		$E(x^2)$	Air voids	PSP	Log (PSP)	Calculated Log k
		location	scale	x_{min}	x_{max}	$\int x^2 f(x)dx$	n (%)	$n[E(x^2)]$	Log $n[E(x^2)]$	
		μ	σ							
GV-12.5-76	223	0.150	0.745	0.17	11.84	3.9	9.2	35.7	1.6	2.35
GV-12.5-79	2049	0.105	0.762	0.17	12.73	3.8	13.7	51.5	1.7	3.31
GV-12.5-81	6553	0.451	0.779	0.17	13.33	7.3	14.7	107.2	2.0	3.82
GV-12.5-84	9850	0.156	0.777	0.17	12.64	4.3	17.4	74.2	1.9	3.99
LS-12.5-79	2984	0.331	0.772	0.17	13.99	5.9	13.1	77.4	1.9	3.47
LS-12.5-81	1137	0.451	0.779	0.17	13.33	7.3	11.7	85.3	1.9	3.06
LS-12.5-90	24525	0.433	0.792	0.17	14.67	7.5	18.8	140.7	2.1	4.39
LS-12.5-83	7949	0.477	0.775	0.17	13.11	7.6	15.4	116.6	2.1	3.90
LS-25.0-79	1746	0.356	0.787	0.17	15.91	6.6	14.3	93.5	2.0	3.24
LS-25.0-84	8716	0.425	0.783	0.17	13.32	7.1	15.4	108.5	2.0	3.94
LS-25.0-91	32350	0.511	0.854	0.17	20.70	10.7	20.0	213.7	2.3	4.51

TABLE 10 PSP calculation for Weibull distribution and laboratory specimens

Label	Measured Permeability (k) 10^{-5} cm/s	Distribution Parameters		Diameters		$E(x^2)$	Air voids	PSP	Log (PSP)	Calculated Log k
		scale	shape	x_{min}	x_{max}	$\int x^2 f(x)dx$	n (%)	$n[E(x^2)]$	Log $n[E(x^2)]$	
		α	β							
GV-12.5-76	223	1.658	1.517	0.17	11.84	3.2	9.2	29.8	1.5	2.35
GV-12.5-79	2049	1.607	1.430	0.17	12.73	3.2	13.7	43.9	1.6	3.31
GV-12.5-81	6553	2.264	1.501	0.17	13.33	6.1	14.7	89.4	2.0	3.82
GV-12.5-84	9850	1.700	1.427	0.17	12.64	3.6	17.4	62.4	1.8	3.99
LS-12.5-79	2984	2.011	1.474	0.17	13.99	4.9	13.1	63.9	1.8	3.47
LS-12.5-81	1137	2.264	1.501	0.17	13.33	6.1	11.7	71.1	1.9	3.06
LS-12.5-90	24525	2.249	1.429	0.17	14.67	6.3	18.8	118.3	2.1	4.39
LS-12.5-83	7949	2.319	1.501	0.17	13.11	6.4	15.4	98.8	2.0	3.90
LS-25.0-79	1746	2.079	1.424	0.17	15.91	5.4	14.3	76.8	1.9	3.24
LS-25.0-84	8716	2.223	1.444	0.17	13.32	6.1	15.4	93.5	2.0	3.94
LS-25.0-91	32350	2.519	1.285	0.17	20.70	8.8	20.0	175.7	2.2	4.51

TABLE 11 PSP calculation for Lognormal distribution and field specimens

Label	Measured Permeability (k) 10^{-5} cm/s	Distribution Parameters location μ	Distribution Parameters scale σ	Diameters x_{min}	Diameters x_{max}	$E(x^2)$ $\int x^2 f(x)dx$	Air voids n (%)	PSP $n[E(x^2)]$	Log (PSP) Log $n[E(x^2)]$	Calculated Log k
MS1 - 1	697	0.267	0.785	0.16	16.62	5.6	13.9	77.4	1.9	2.84
MS1 - 4	10	-0.358	0.572	0.32	13.08	0.9	6.6	6.2	0.8	1.00
MS1 - 6	37	-0.227	0.609	0.32	9.31	1.3	7.0	9.3	1.0	1.57
MS1 - 7	1	-0.393	0.568	0.32	8.61	0.9	4.4	3.8	0.6	0.00
MS2 - 7	49	-0.024	0.631	0.16	15.44	2.1	9.5	20.1	1.3	1.69
MS2 - 9	76	0.135	0.672	0.17	7.26	3.0	7.1	21.1	1.3	1.88
MS2 - 11	119	-0.065	0.969	0.16	13.35	4.5	6.9	31.3	1.5	2.08
MS4 - 11	54	-0.049	0.854	0.32	6.48	2.7	8.2	22.5	1.4	1.73
MS4 - 7	120	0.010	0.883	0.32	8.31	3.5	8.8	31.2	1.5	2.08
MS4 - 14	291	-0.072	0.928	0.16	12.97	4.1	9.0	36.5	1.6	2.46
MS5 - 1	3333	-0.022	0.782	0.22	16.51	3.2	7.4	23.5	1.4	3.52
MS5 - 3	30	0.113	0.806	0.22	16.88	4.4	5.4	23.8	1.4	1.48
MS5 - 4	348	0.031	0.810	0.22	12.45	3.7	8.5	31.2	1.5	2.54
MS5 - 11	4960	0.261	0.736	0.22	13.91	4.8	10.6	50.7	1.7	3.70
MS5 - 12	244	0.362	0.702	0.22	14.66	5.4	7.2	38.7	1.6	2.39
MS6 - 6	269	0.036	0.750	0.22	9.69	3.1	8.7	26.8	1.4	2.43
MS6 - 7	1386	-0.343	0.568	0.22	9.38	1.0	11.0	10.6	1.0	3.14
MS6 - 8	656	-0.314	0.615	0.22	12.43	1.1	9.6	10.9	1.0	2.82
MS6 - 13	1	-0.131	0.697	0.22	10.21	2.0	6.0	12.0	1.1	0.00
MS6 - 14	178	-0.515	0.899	0.22	10.05	1.6	7.5	12.2	1.1	2.25
MS7 - 6	28	-0.084	0.696	0.32	7.74	2.1	7.2	15.3	1.2	1.45
MS7 - 9	527	-0.092	0.892	0.32	11.74	3.5	10.6	37.2	1.6	2.72
MS8 - 10	13477	0.130	0.716	0.21	11.75	3.5	10.6	37.0	1.6	4.13
MS8 - 11	16307	0.318	0.745	0.21	11.25	5.2	9.6	50.0	1.7	4.21
MS8 - 12	1619	0.195	0.717	0.21	10.42	3.9	7.6	29.5	1.5	3.21
MS8 - 13	17789	0.276	0.730	0.21	11.78	4.7	12.6	59.6	1.8	4.25

TABLE 12 PSP calculation for Weibull distribution and field specimens

Label	Measured Permeability (k) 10^{-5} cm/s	Distribution Parameters scale α	Distribution Parameters shape β	Diameters x_{min}	Diameters x_{max}	$E(x^2)$ $\int x^2 f(x)dx$	Air voids n (%)	PSP $n[E(x^2)]$	Log (PSP) Log $n[E(x^2)]$	Calculated Log k
MS1 - 1	697	1.908	1.411	0.16	16.62	4.6	13.9	63.5	1.8	2.84
MS1 - 4	10	0.937	1.655	0.32	13.08	1.0	6.6	6.4	0.8	1.00
MS1 - 6	37	1.035	1.589	0.32	9.31	1.2	7.0	8.5	0.9	1.57
MS1 - 7	1	0.906	1.645	0.32	8.61	0.9	4.4	4.0	0.6	0.00
MS2 - 7	49	1.963	1.479	0.16	15.44	4.6	9.5	44.1	1.6	1.69
MS2 - 9	76	1.716	1.562	0.17	7.26	3.4	7.1	24.1	1.4	1.88
MS2 - 11	119	1.874	1.493	0.16	13.35	4.2	6.9	29.0	1.5	2.08
MS4 - 11	54	1.335	1.680	0.32	6.48	1.9	8.2	16.0	1.2	1.73
MS4 - 7	120	1.367	1.661	0.32	8.31	2.1	8.8	18.1	1.3	2.08
MS4 - 14	291	1.577	1.619	0.16	12.97	3.0	9.0	27.0	1.4	2.46
MS5 - 1	3333	1.516	1.102	0.22	16.51	3.9	7.4	28.9	1.5	3.52
MS5 - 3	30	1.556	1.233	0.22	16.88	3.5	5.4	19.0	1.3	1.48
MS5 - 4	348	1.447	1.287	0.22	12.45	2.9	8.5	24.6	1.4	2.54
MS5 - 11	4960	1.477	1.141	0.22	13.91	3.5	10.6	37.2	1.6	3.70
MS5 - 12	244	1.443	1.317	0.22	14.66	2.8	7.2	20.2	1.3	2.39
MS6 - 6	269	1.641	1.453	0.22	9.69	3.3	8.7	28.6	1.5	2.43
MS6 - 7	1386	1.523	1.402	0.22	9.38	2.9	11.0	32.2	1.5	3.14
MS6 - 8	656	1.842	1.549	0.22	12.43	3.9	9.6	37.8	1.6	2.82
MS6 - 13	1	2.003	1.655	0.22	10.21	4.4	6.0	26.6	1.4	0.00
MS6 - 14	178	1.483	1.522	0.22	10.05	2.6	7.5	19.4	1.3	2.25
MS7 - 6	28	1.003	1.539	0.32	7.74	1.2	7.2	8.4	0.9	1.45
MS7 - 9	527	1.255	1.393	0.32	11.74	2.0	10.6	21.2	1.3	2.72
MS8 - 10	13477	0.947	1.107	0.21	11.75	1.5	10.6	16.0	1.2	4.13
MS8 - 11	16307	0.940	1.082	0.21	11.25	1.5	9.6	14.8	1.2	4.21
MS8 - 12	1619	1.296	1.509	0.21	10.42	2.0	7.6	15.1	1.2	3.21
MS8 - 13	17789	1.423	1.178	0.21	11.78	3.1	12.6	39.3	1.6	4.25

Al-Omari et al. (1) reported that for these mixtures, the air void connectivity varies considerably in the field cores compared with the LKC specimens. Figures 12 and 13 are examples of flow paths that were captured on the LKC specimens and field cores. In addition, Masad et al. (15) showed that a number of field cores do not have connected flow paths across the full depth and, that the measured permeability was in some cases only due to the flow in a small part of the core near the surface. Therefore, it was decided to study the relationship between permeability and air void distribution only in the connected flow paths that contribute to permeability. Also, only cores that have connected flow paths were used in the analysis. A macro was developed to identify and analyze the connected voids while eliminating the stagnant regions and isolated air voids, etc.

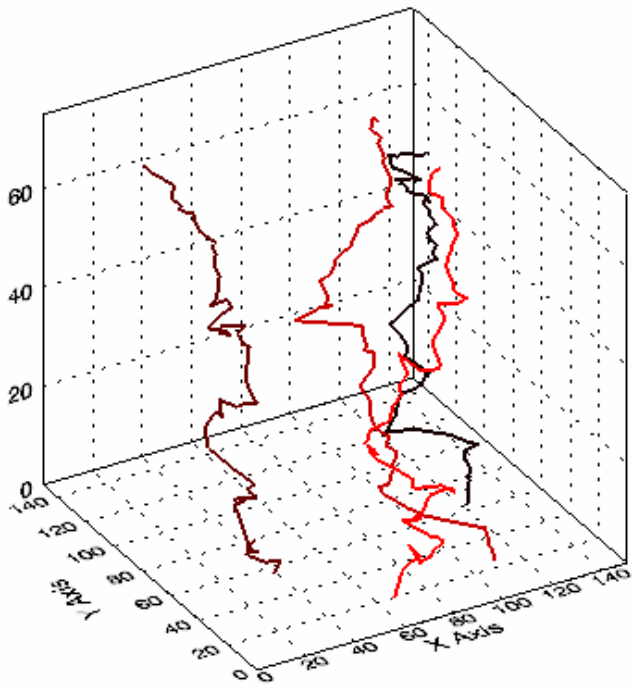

Figure 12 Flow paths in a LKC specimen.

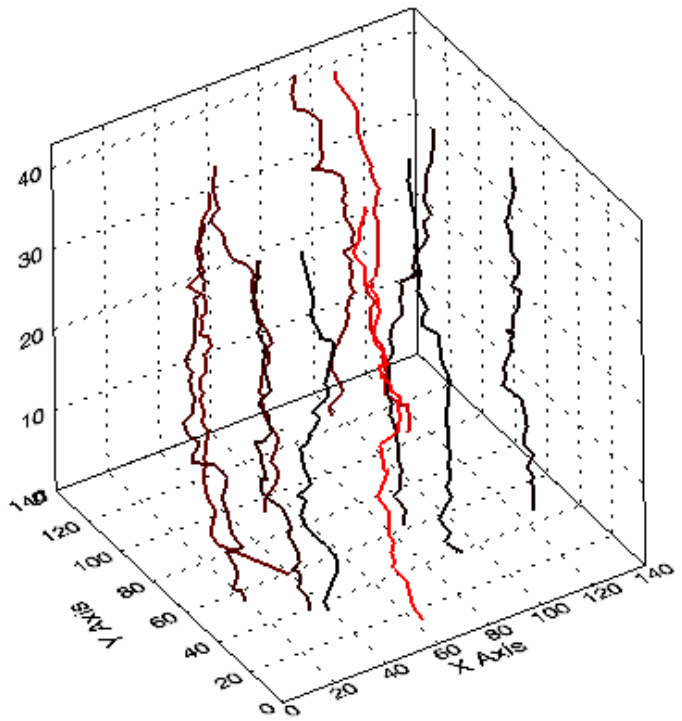

Figure 13 Flow paths in a field specimen.

The regression analysis results for Lognormal and Weibull distributions for both sets of specimens when taking into consideration only the connected flow paths are shown in Figures 14 to 17. The respective data is included in Tables 13 to 16.

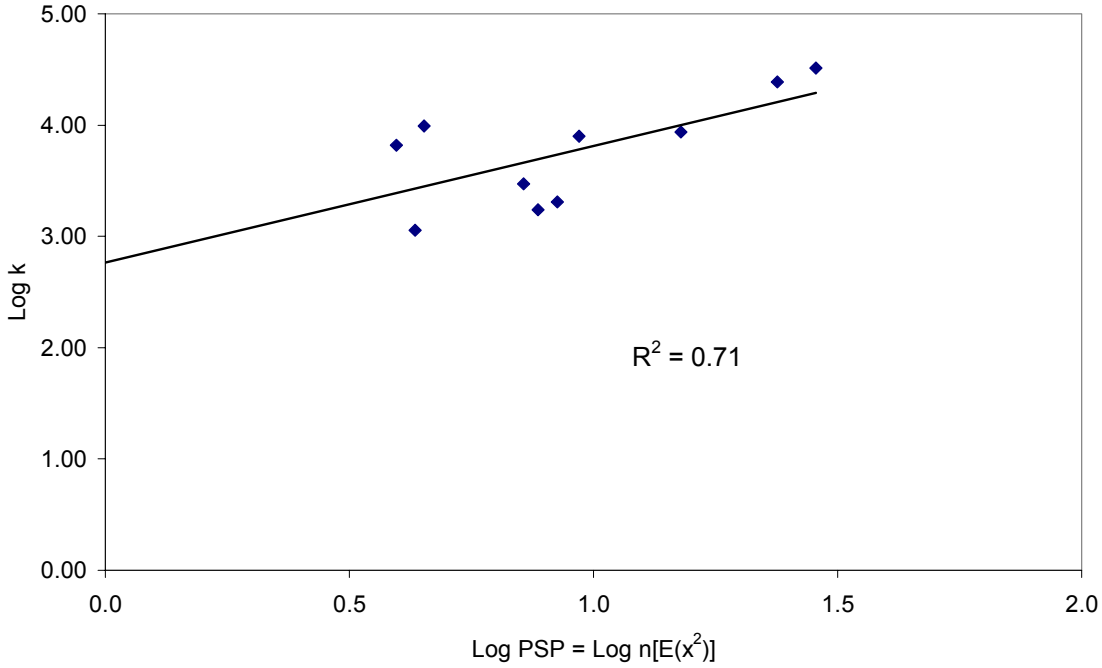

Figure 14 Permeability vs. PSP using Lognormal distribution for LKC flow paths.

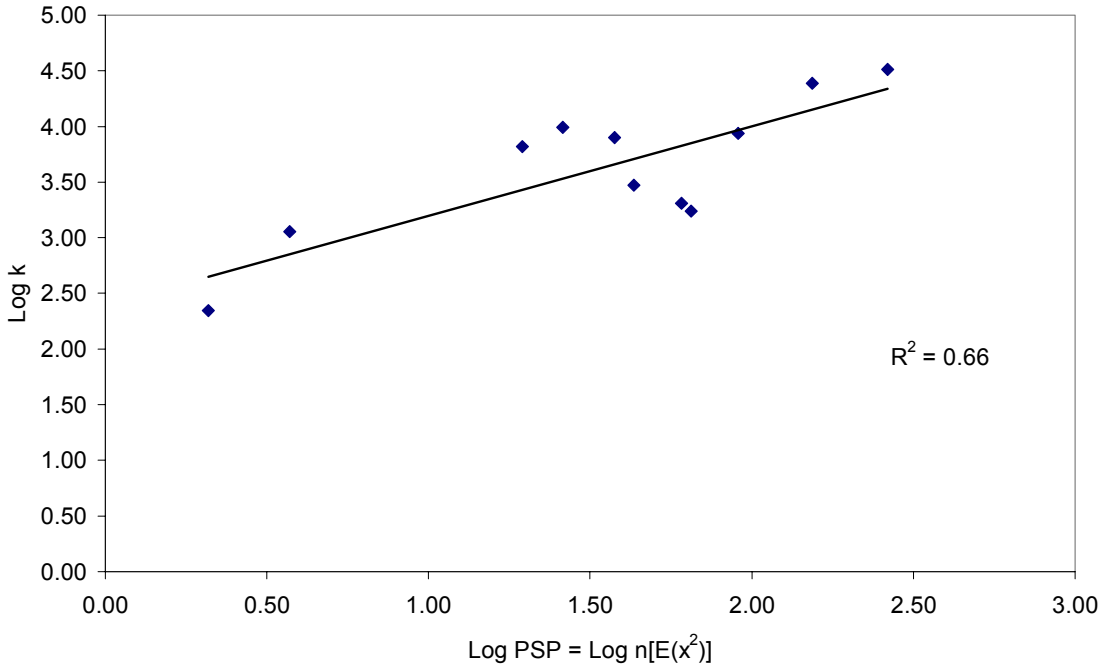

Figure 15 Permeability vs. PSP using Weibull distribution for LKC flow paths.

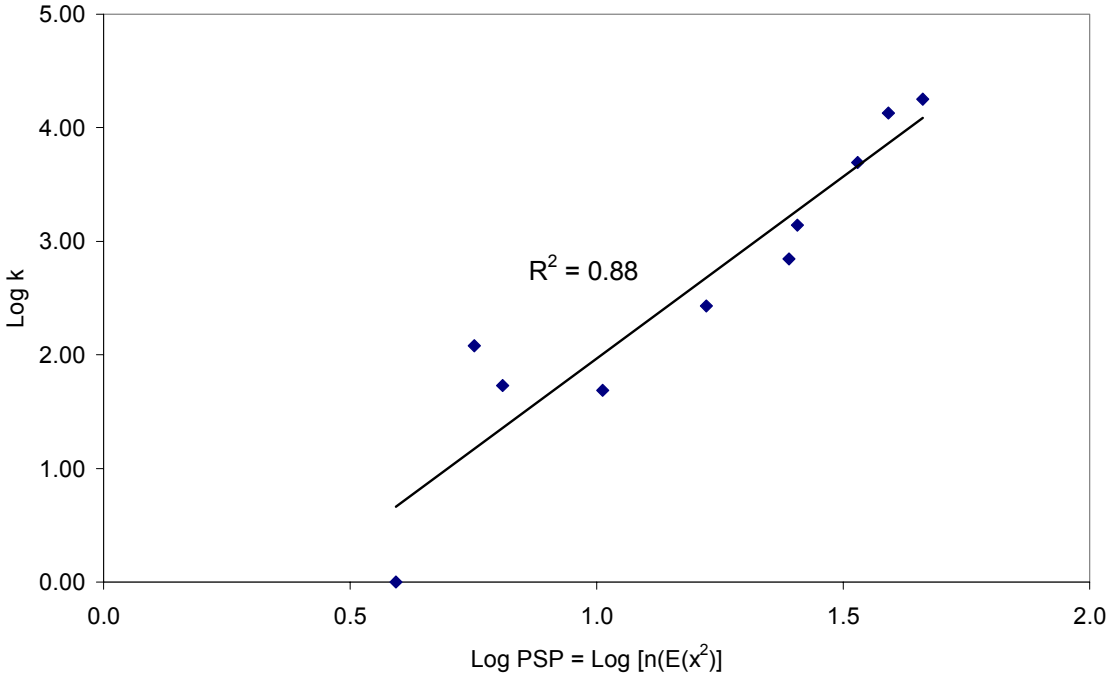

Figure 16 Permeability vs. PSP using Lognormal distribution for field flow paths.

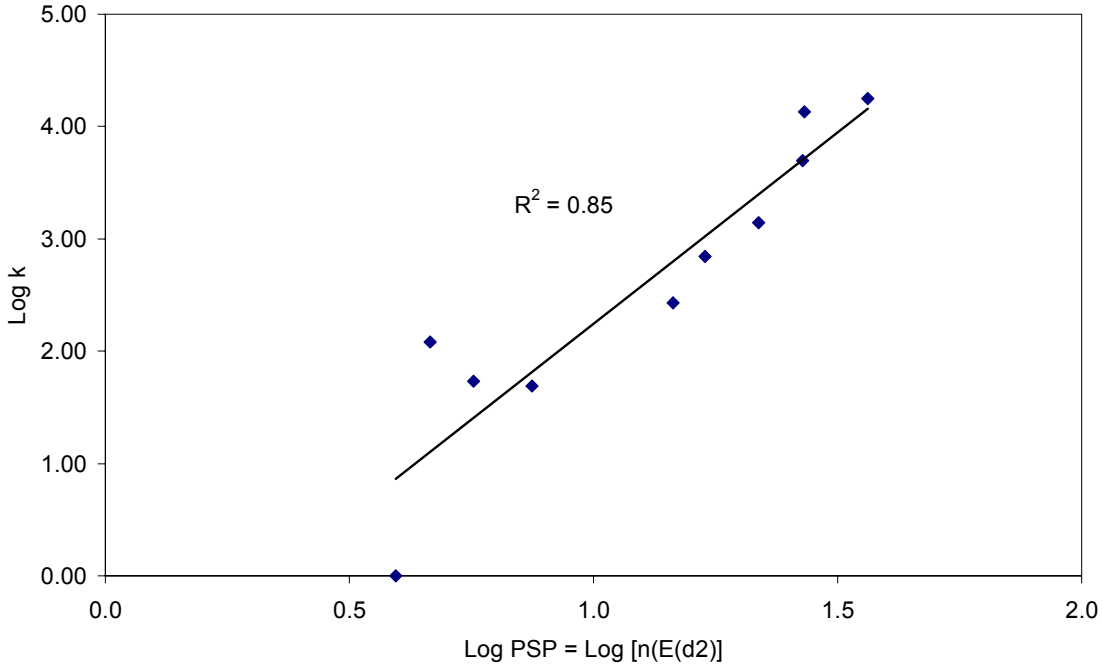

Figure 17 Permeability vs. PSP using Weibull distribution for field flow paths.

TABLE 13 PSP calculation for Lognormal distribution and flow paths of laboratory LKC specimens

Label	Measured Permeability (k) 10^{-5} cm/s	Distribution Parameters		Diameters		$E(x^2)$	Eff. Air voids	PSP	Log (PSP)	Calculated Log k
		location	scale	x_{min}	x_{max}	$\int x^2 f(x)dx$	n_{eff} (%)	$n[E(x^2)]$	Log $n[E(x^2)]$	
		μ	σ							
GV-12.5-76	223	0.227	0.295	0.17	11.07	1.9	0.2	0.4	-0.4	2.35
GV-12.5-79	2049	0.233	0.322	0.17	13.19	2.0	4.3	8.4	0.9	3.31
GV-12.5-81	6553	0.295	0.313	0.17	12.31	2.2	1.8	4.0	0.6	3.82
GV-12.5-84	9850	0.237	0.312	0.17	11.76	2.0	2.3	4.5	0.7	3.99
LS-12.5-79	2984	0.327	0.305	0.17	14.43	2.3	3.1	7.2	0.9	3.47
LS-12.5-81	1137	0.699	0.655	0.17	11.11	8.6	0.5	4.3	0.6	3.06
LS-12.5-90	24525	0.355	0.306	0.17	15.92	2.5	9.7	23.8	1.4	4.39
LS-12.5-83	7949	0.343	0.306	0.17	12.21	2.4	3.9	9.3	1.0	3.90
LS-25.0-79	1746	0.320	0.320	0.17	17.26	2.3	3.3	7.7	0.9	3.24
LS-25.0-84	8716	0.352	0.318	0.17	15.45	2.5	6.1	15.1	1.2	3.94
LS-25.0-91	32350	0.381	0.332	0.17	20.84	2.7	10.7	28.5	1.5	4.51

TABLE 14 PSP calculation for Weibull distribution and flow paths of laboratory specimens

Label	Measured Permeability (k) 10^{-5} cm/s	Distribution Paramet		Diameters		$E(x^2)$	Eff Air voids	PSP	Log (PSP)	Calculated Log k
		scale	shape	x_{min}	x_{max}	$\int x^2 f(x)dx$	n_{eff} (%)	$n[E(x^2)]$	Log $n[E(x^2)]$	
		α	β							
GV-12.5-76	223	2.29	1.88	0.17	11.07	10.4	0.2	2.1	0.3	2.35
GV-12.5-79	2049	2.38	1.74	0.17	13.19	14.1	4.3	60.7	1.8	3.31
GV-12.5-81	6553	2.73	1.77	0.17	12.31	10.8	1.8	19.5	1.3	3.82
GV-12.5-84	9850	2.38	1.79	0.17	11.76	11.3	2.3	26.0	1.4	3.99
LS-12.5-79	2984	2.92	1.81	0.17	14.43	13.9	3.1	43.1	1.6	3.47
LS-12.5-81	1137	2.71	1.94	0.17	11.11	7.4	0.5	3.7	0.6	3.06
LS-12.5-90	24525	3.11	1.82	0.17	15.92	15.9	9.7	154.1	2.2	4.39
LS-12.5-83	7949	3.03	1.81	0.17	12.21	9.7	3.9	37.7	1.6	3.90
LS-25.0-79	1746	2.91	1.74	0.17	17.26	19.7	3.3	65.0	1.8	3.24
LS-25.0-84	8716	3.13	1.74	0.17	15.45	14.8	6.1	90.6	2.0	3.94
LS-25.0-91	32350	3.38	1.69	0.17	20.84	24.6	10.7	262.9	2.4	4.51

TABLE 15 PSP calculation for Lognormal distribution and flow paths of field specimens

Label	Measured Permeability (k) 10^{-5} cm/s	Distribution Parameters		Diameters		$E(x^2)$	Eff. Air voids	PSP	Log (PSP)	Calculated Log k
		location	scale	x_{min}	x_{max}	$\int x^2 f(x)dx$	n_{eff} (%)	$n[E(x^2)]$	Log $n[E(x^2)]$	
		μ	σ							
MS 1-1	697	0.233	0.780	0.16	16.07	5.1	4.8	24.5	1.4	2.84
MS 2-7	49	0.293	0.739	0.16	15.06	5.1	2.0	10.3	1.0	1.69
MS 4-11	54	0.333	0.596	0.32	6.46	3.6	1.8	6.4	0.8	1.73
MS 4-7	120	0.319	0.616	0.32	8.29	3.9	1.5	5.6	0.8	2.08
MS 5-11	4960	0.595	0.855	0.22	13.91	10.6	3.2	33.8	1.5	3.70
MS 6-6	269	0.530	0.688	0.22	9.17	6.4	2.6	16.7	1.2	2.43
MS 6-7	1386	0.456	0.709	0.22	8.92	5.8	4.4	25.5	1.4	3.14
MS 6-13	1	0.561	0.604	0.22	6.41	5.2	0.7	3.9	0.6	0.00
MS 8-10	13477	0.154	0.910	0.21	11.75	5.4	7.2	39.1	1.6	4.13
MS 8-13	17789	0.452	0.832	0.21	11.69	7.6	6.1	45.8	1.7	4.25

TABLE 16 PSP calculation for Weibull distribution and flow paths of field specimens

Label	Measured	Distribution Parameters		Diameters		$E(x^2)$	Eff. Porosity	PSP	Log (PSP)	Calculated Log k
	Permeability (k)	scale	shape	x_{min}	x_{max}	$\int x^2 f(x)dx$	n_{eff} (%)	$n[E(x^2)]$	Log $n[E(x^2)]$	
	10^{-5} cm/s	α	β							
MS 1-1	697	1.787	1.663	0.16	16.07	3.5	4.8	16.9	1.2	2.84
MS 2-7	49	1.867	1.743	0.16	15.06	3.7	2.0	7.5	0.9	1.69
MS 4-11	54	1.819	2.176	0.32	6.46	3.2	1.8	5.7	0.8	1.73
MS 4-7	120	1.807	2.115	0.32	8.29	3.2	1.5	4.6	0.7	2.08
MS 5-11	4960	2.663	1.500	0.22	13.91	8.4	3.2	26.8	1.4	3.70
MS 6-6	269	2.320	1.852	0.22	9.17	5.6	2.6	14.5	1.2	2.43
MS 6-7	1386	2.172	1.804	0.22	8.92	5.0	4.4	21.8	1.3	3.14
MS 6-13	1	2.313	2.071	0.22	6.41	5.3	0.7	3.9	0.6	0.00
MS 8-10	13477	1.742	1.438	0.21	11.75	3.7	7.2	27.1	1.4	4.13
MS 8-13	17789	2.279	1.552	0.21	11.69	6.0	6.1	36.4	1.6	4.25

Figures 14-17 show that the correlation coefficient R^2 notably increased when analyzing solely the flow paths for the field samples for which the R^2 increased from 48% to 88% and from 22% to 85% using Lognormal and Weibull distributions respectively. On the other hand, the R^2 values were slightly decreased (74% to 71% and 75% to 66%) for the LKC specimens.

The analysis was performed for the SGC granite and limestone specimens by considering all voids regardless of their connectivity. The relationship between the pore size parameter and the permeability of these cores was done using two different permeability measurement procedures. The constant head method gave higher permeability values than the falling head method that was used in Florida. The saturation procedure that was followed in the Florida method was based on AASHTO T-283. Following this procedure, a target saturation of 65 to 80 percent has to be achieved by allowing vacuum saturation during 15 minutes. Next, the specimen is placed in water bath without vacuum for an additional 15 min. If the minimum saturation is not achieved, another cycle is done until the target is attained. Finally, the core is placed in a

water bath at 60C for 24 hours and is allowed to drain 36 hours; then the specimen is located on a dehumidify chamber for 48 hours prior to the permeability measurement. On the other hand, for measuring the permeability with the constant head method, the cores were saturated for 24 hours and then they were vacuum saturated during 10 minutes with a pressure of 28in Hg. The percentage of saturation varied from core to core as shown in Table 17 as well as the permeabilities measured with the two methods. The results for the relationships between the constant head and falling head permeabilities and the pore size parameter are shown in Figures 19 to 22, and the corresponding data is summarized in Tables 18 to 21. This was done taking into account all the air voids.

TABLE 17 Degree of saturation of SGC specimens

Specimen	Degree of Saturation, S%	Falling head permeability (10^{-5} cm/s)	Constant head permeability (10^{-5} cm/s)
GA-C1	89.8	67.50	228.13
GA-C2	78.3	59.00	271.18
GA-C3	76.5	56.00	93.00
GA-F1	97.4	25.33	76.66
GA-F2	78.1	9.33	74.35
GA-F3	74.7	34.25	172.91
WR-C1	82.4	72.37	301.98
WR-C2	85.2	64.24	367.49
WR-C3	97.7	29.39	379.60
WR-F1	98.4	69.63	226.41
WR-F2	92.2	17.81	177.69
WR-F3/C4	98.4	9.68	298.12

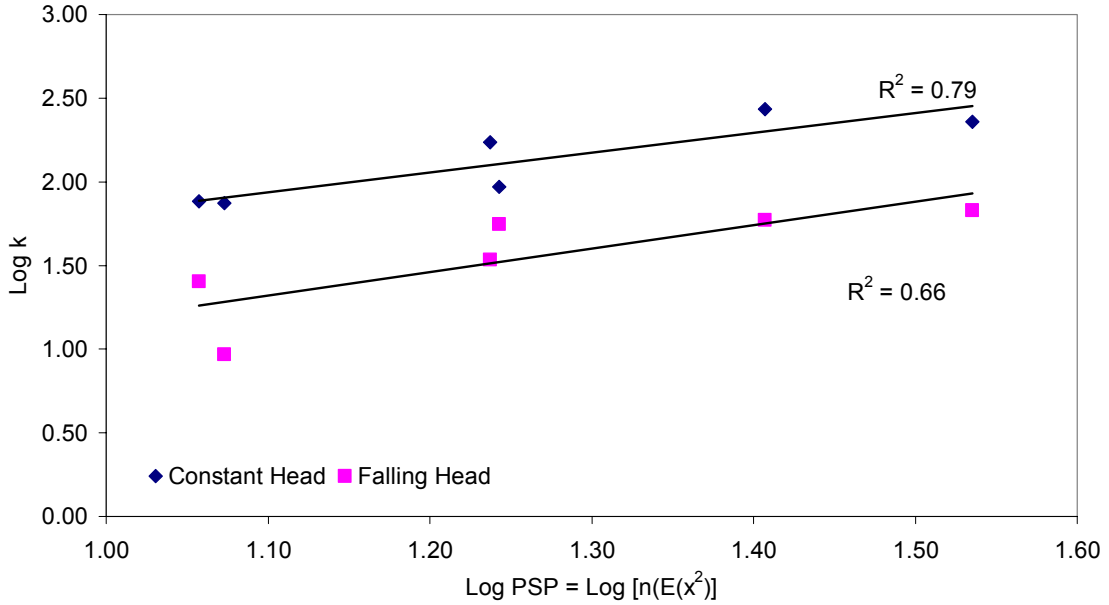

Figure 18 Permeability vs. PSP using Lognormal distribution for SGC granite cores.

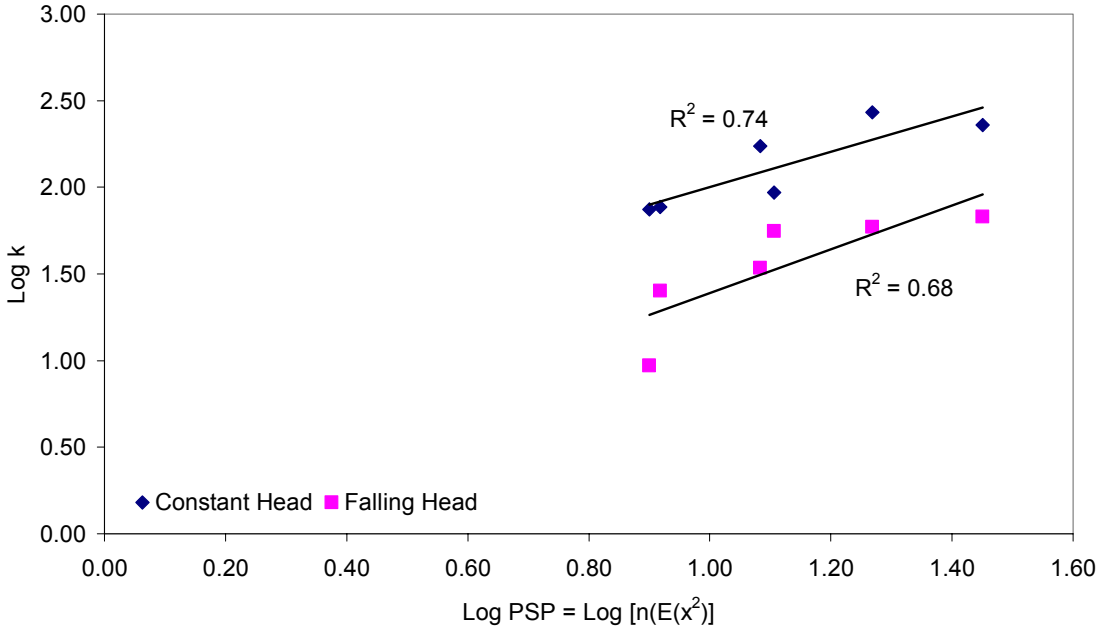

Figure 19 Permeability vs. PSP using Weibull distribution for SGC granite cores.

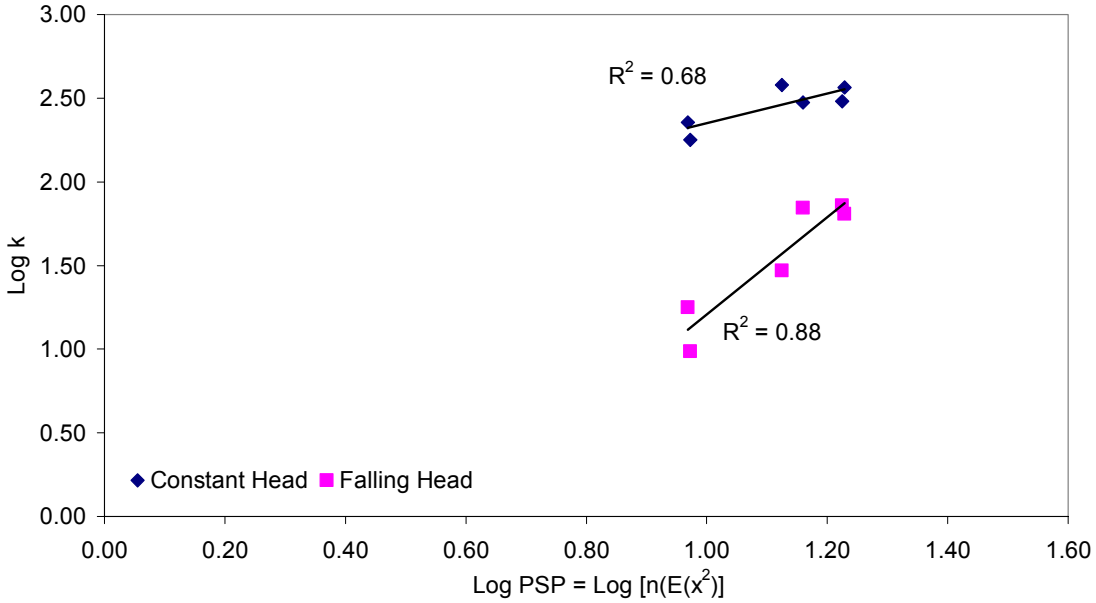

Figure 20 Permeability vs. PSP using Lognormal distribution for SGC limestone cores.

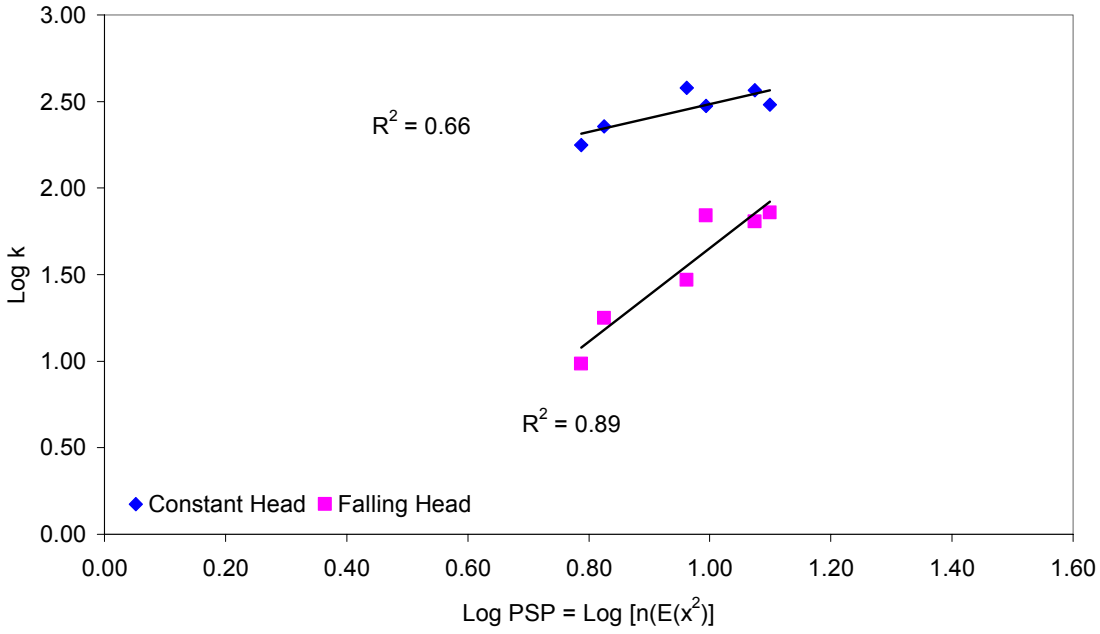

Figure 21 Permeability vs. PSP using Weibull distribution for SGC limestone cores.

TABLE 18 PSP calculation for Lognormal distribution and limestone specimens

Core	Constant Head Permeability (k) 10^{-5} cm/s	Distribution Parameters		Diameters		$E(x^2)$	Eff Air voids	PSP	Log (PSP)	Calculated Log k
		location	scale	x_{min}	x_{max}	$\int x^2 f(x)dx$	n_{eff} (%)	$n[E(x^2)]$	Log $n[E(x^2)]$	
		μ	σ							
WR-C1	301.98	-0.001	0.703	0.22	8.40	2.5	6.6	16.8	1.2	2.48
WR-C2	367.49	-0.046	0.730	0.22	11.21	2.6	6.6	16.9	1.2	2.57
WR-C3	379.60	-0.185	0.718	0.22	10.98	1.9	6.9	13.3	1.1	2.58
WR-F1	226.41	-0.324	0.691	0.22	8.67	1.3	7.0	9.3	1.0	2.35
WR-F2	177.69	-0.390	0.739	0.22	11.09	1.4	6.9	9.4	1.0	2.25
WR-F3/C4	298.12	-0.184	0.725	0.22	11.08	2.0	7.3	14.4	1.2	2.47

TABLE 19 PSP calculation for Weibull distribution and limestone specimens

Core	Constant Head Permeability (k) 10^{-5} cm/s	Distribution Parameters		Diameters		$E(x^2)$	Eff Air voids	PSP	Log (PSP)	Calculated Log k
		scale	shape	x_{min}	x_{max}	$\int x^2 f(x)dx$	n_{eff} (%)	$n[E(x^2)]$	Log $n[E(x^2)]$	
		α	β							
WR-C1	301.98	1.360	1.872	0.22	8.40	1.9	6.6	12.6	1.1	2.48
WR-C2	367.49	1.312	1.816	0.22	11.21	1.8	6.6	11.9	1.1	2.57
WR-C3	379.60	1.133	1.864	0.22	10.98	1.3	6.9	9.2	1.0	2.58
WR-F1	226.41	0.972	1.949	0.22	8.67	1.0	7.0	6.7	0.8	2.35
WR-F2	177.69	0.925	1.854	0.22	11.09	0.9	6.9	6.1	0.8	2.25
WR-F3/C4	298.12	1.137	1.845	0.22	11.08	1.3	7.3	9.8	1.0	2.47

TABLE 20 PSP calculation for Lognormal distribution and granite specimens

Core	Constant Head Permeability (k) 10^{-5} cm/s	Distribution Parameters		Diameters		$E(x^2)$	Eff Air voids	PSP	Log (PSP)	Calculated Log k
		location	scale	x_{min}	x_{max}	$\int x^2 f(x)dx$	n_{eff} (%)	$n[E(x^2)]$	Log $n[E(x^2)]$	
		μ	σ							
GA-C1	228.13	0.301	0.701	0.22	8.40	4.319	7.9	34.29	1.54	2.36
GA-C2	271.18	0.147	0.728	0.22	11.21	3.684	6.9	25.53	1.41	2.43
GA-C3	93.00	-0.021	0.696	0.22	10.98	2.478	7.1	17.50	1.24	1.97
GA-F1	76.66	-0.266	0.683	0.22	8.67	1.472	7.8	11.41	1.06	1.88
GA-F2	74.35	-0.295	0.732	0.22	11.09	1.594	7.4	11.83	1.07	1.87
GA-F3	172.91	-0.093	0.723	0.22	11.08	2.309	7.5	17.27	1.24	2.24

TABLE 21 PSP calculation for Weibull distribution and granite specimens

Core	Constant Head Permeability (k) 10^{-5} cm/s	Distribution Parameters		Diameters		$E(x^2)$	Eff Air voids	PSP	Log (PSP)	Calculated Log k
		scale	shape	x_{min}	x_{max}	$\int x^2 f(x)dx$	n_{eff} (%)	$n[E(x^2)]$	Log $n[E(x^2)]$	
		α	β							
GA-C1	228.13	1.849	1.840	0.22	8.40	3.6	7.9	28.2	1.5	2.36
GA-C2	271.18	1.596	1.799	0.22	11.21	2.7	6.9	18.6	1.3	2.43
GA-C3	93.00	1.329	1.892	0.22	10.98	1.8	7.1	12.8	1.1	1.97
GA-F1	76.66	1.029	1.957	0.22	8.67	1.1	7.8	8.3	0.9	1.88
GA-F2	74.35	1.017	1.851	0.22	11.09	1.1	7.4	7.9	0.9	1.87
GA-F3	172.91	1.247	1.838	0.22	11.08	1.6	7.5	12.1	1.1	2.24

According to the R^2 values, the distribution that most closely represents the relationship of permeability and air void size distribution is Lognormal. The derived equations for permeability obtained from the regression analysis, and their corresponding correlation coefficients are found in Table 22. These equations have the form of Equation 19. The transformations of these equations, to the form expressed in Equation 20 are included in Table 23. It was considered that the permeability measurements of the constant head method were more reliable, because this method is best suited for samples that contain no more than 10% particles passing the 75-μm (No. 200) sieve (22). The gradations of these specimens are included in appendix A.

TABLE 22 Regression equations for permeability

Specimen	Lognormal	Weibull
LKC (All voids)	Log k=2.5834 Log (PSP)-1.4228 R^2 = 0.74	Log k=2.6192 Log (PSP)-1.2912 R^2 = 0.75
LKC (Flow paths)	Log k=1.0489 Log (PSP)+2.7664 R^2 = 0.71	Log k=0.805 Log (PSP)+2.3931 R^2 = 0.66
MSD (All voids)	Log k=2.5002 Log (PSP)-1.0183 R^2 = 0.48	Log k=1.9664 Log (PSP)-0.2168 R^2 = 0.22
MSD (Flow paths)	Log k=3.1997 Log (PSP)-1.2298 R^2 = 0.88	Log k=3.4067 Log (PSP)-1.1618 R^2 = 0.85
SGC Granite (All voids), constant head method	Log k=1.1813 Log (PSP)+0.6386 R^2 = 0.78	Log k=1.0137 Log (PSP)+0.9891 R^2 = 0.74
SGC Limestone (All voids), constant head method	Log k=0.8901Log (PSP)+1.4598 R^2 = 0.68	Log k=0.8074Log (PSP)+1.6779 R^2 = 0.66

TABLE 23 Permeability equations with Lognormal distribution

Specimen	Permeability
LKC (All voids)	$k=0.04\ PSP^{2.5834}$
LKC (Flow paths)	$k=584\ PSP^{1.0489}$
Field Cores (All voids)	$k=0.10PSP^{2.5002}$
Field Cores (Flow paths)	$k=0.06\ PSP^{3.1997}$
SGC Granite (All voids), constant head method	$k=4.35PSP^{1.1813}$
SGC Limestone (All voids), constant head method	$k=28.83\ PSP^{0.8901}$

Summary

Several studies have demonstrated that HMA permeability is highly related to percent air voids. However, this relationship can not be generalized because the air void size distribution has significant influence on HMA permeability. X-ray CT made it possible to capture and analyze air void distribution in HMA.

Three sets of specimens were analyzed: LKC laboratory specimens, field cores, and SGC laboratory specimens. A relationship is developed between permeability and parameters that represent air void distribution. The probability density functions that best fit the size distribution were determined. This was done by using probability plots and relying on the Pearson correlation coefficient to judge the accuracy of the fitting. The Lognormal and the Weibull distribution were found as the most suitable probability distributions to fit the data, having coefficients of determination between 68% and 88%.

The capillary model established by Garcia-Bengochea was used to relate permeability to the pore size parameter (PSP) that was determined using probabilistic approach for the analysis of air voids. This PSP was calculated using the assumption that the probability of having two air voids on adjacent sections connected is totally correlated, since the distance between sections is very small.

The results obtained from the regression analyses were very good for the laboratory LKC and SGC specimens. However, this was not the case for the field cores when all voids were considered. An alternative approach was followed where only the connected voids in field cores were analyzed. Consequently, there was a significant improvement between the permeability and air void size distribution in the field cores.

CHAPTER IV

THE RELATIONSHIP BETWEEN AIR VOID DISTRIBUTION, MATERIAL SURFACE PROPERTIES AND MOISTURE DAMAGE

Introduction

The durability of a pavement throughout its design life can be achieved when the pavement is resistant to weathering, cracking, and traffic abrasion (23). Weathering consists of the effects provoked by oxidation or hardening of the asphalt, moisture damage and changes in the aggregate soundness due to freezing and thawing. Moisture can deteriorate asphalt dramatically by affecting the stiffness and the strength (loss of cohesion) of the asphalt film, and also by breaking the adhesive bond between aggregates and asphalt. Loss of adhesion can lead to stripping and raveling whereas loss of cohesion can lessen the load carrying capacity of the pavement leading to premature cracking.

This chapter documents the results of studying the relationship between moisture damage, air void distribution, material surface properties and pore pressure. The resistance to moisture damage is assessed by measuring the mechanical properties of HMA specimens before and after moisture conditioning. These mechanical properties were measured at the University of Florida and were made available to this study by Dr. Birgisson. The surface energy of the aggregates and asphalt binder were measured in order to assess the fracture and healing capabilities of the mixes with and without the presence of moisture.

Measurements of HMA Moisture Damage

Zhang et al (24) developed a viscoelastic fracture mechanics-based framework to describe the fracture properties of HMA. These researchers demonstrated that there are two fracture thresholds that define the type of damage that can take place in an asphalt mixture: micro-damage and macro-damage. Micro-damage is not related to crack initiation or crack growth and is totally healable after a resting period. On the other hand, macro-damage is associated with crack growth and the damage provoked is irreversible.

It was found that the dissipated creep strain energy (DCSE) and the fracture energy (FE) define the two threshold values under cyclic and continuously increasing loading, respectively. These limits can be determined from the stress-strain response of a tensile strength test and resilient modulus test using the SuperPave™ Indirect Tensile test (24). The DCSE corresponds to the area under the tensile strength/strain curve that is not recoverable and can be calculated as the total area under the curve (i.e. fracture energy), minus the area that corresponds to the elastic energy. The elastic energy (EE) is equal to the area under this curve limited by a line with slope equal to the resilient modulus, and a vertical line that crosses the x-axis at the strain at failure. A representation of the elastic energy (EE) and dissipated creep strain energy (DCSE) components of the fracture energy can be seen in Figure 22, (24). To determine the elastic energy at fracture the elastic modulus of the mix must be measured. Therefore, these limits account ultimately for the effects of strength, stiffness, strain to failure, and the viscoelastic response of the mixture.

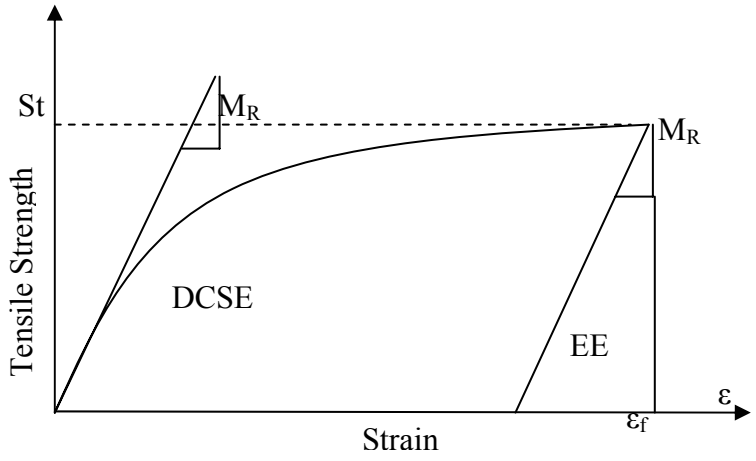

Figure 22 Determination of DCSE.

Based on Figure 22, the elastic energy can be calculated as:

$$EE = \frac{1}{2}\left(\varepsilon_f - \varepsilon_0\right)S_t \quad and \quad FE = EE + DCSE \tag{21}$$

Where the tensile strength S_t can be obtained from a tensile strength test and:

$$\varepsilon_0 = \frac{M_R\varepsilon_f - S_t}{M_R} \tag{22}$$

where

ε_0 = Strain intercept,

M_R = Resilient modulus,

ε_f = Strain at failure,

S_t = Tensile strength at failure,

FE = Fracture energy,

EE = Elastic energy,

DCSE = Dissipated creep strain energy

Birgisson, et al. (2) found that it was necessary to account for the effects that moisture damage causes to key mechanical properties. They demonstrated through the determination of the Superpave^{TM} Indirect Tension Test fracture parameters (i.e. creep, resilient modulus, and tensile strength, tests) on conditioned and unconditioned mixtures, that the effects of moisture damage on the multiple parameters associated with the fracture resistance of mixtures could be summarized into one single number. This number corresponded to the ratio between the number of cycles to failure for conditioned and unconditioned specimens. The calculation of the number of cycles is based on the crack growth law (2, 24), which is based on the dissipated creep strain energy threshold concept as well. This calculation is based on the determination of the stress distribution near the crack tip, as it evolves through the crack length and the damage that occurs while DCSE is building up. This accumulation takes place in small zones of the process zones in front of the crack tip.

The procedure consists of determining the DCSE per cycle and the accumulated DCSE on each zone due to the number of cycles N to fail the previous zone, and so forth until a determined crack size is formed. The accumulated DCSE can be calculated using creep compliance parameters for a specified type of load. For a harversine load that is applied during 0.1 seconds and 0.9 seconds of rest period, the DCSE per cycle is calculated as (2, 24):

$$DCSE/cycle = \int_0^{0.1} \sigma_{avg} \sin(10\pi t)\xi_{\max} \sin(10\pi t)dt \tag{23}$$

Where σ_{avg} is the average stress in the zone of interest, and ξ_{max} is the maximum creep strain rate. The damage rate of an asphalt mixture under constant loading is considered to correspond to its creep compliance. Under the DCSE threshold, this rate of damage is controlled by the creep properties of the mix. The creep compliance can be expressed with a power function of the form (2):

$$D(t) = D_0 + D_1 t^m \tag{24}$$

Where, *D(t)* is the creep compliance, D_o is the glassy compliance of the material, D_1 is the compliance coefficient of time, *m* is the compliance exponent, and *t* is the time of loading.

Also, the strain, and creep compliance are related as (2):

$$\varepsilon(t) = \sigma_{ave} D(t) \tag{25}$$

Therefore the creep strain rate can be formulated by deriving Equation 25 with respect to time, as follows:

$$\xi_{\max} = \frac{\varepsilon(t)}{dt} = \sigma_{ave} \frac{D(t)}{dt} = \sigma_{ave} D_1 \, m t^{m-1} \tag{26}$$

And by substitution of Equation 26 in Equation 23, the DCSE per cycle for a 100-second SuperPave™ IDT creep test is calculated as:

$$DCSE / cycle = \frac{1}{20} \sigma_{avg}^{\ 2} \ D_1 m (100)^{m-1} \tag{27}$$

From Equation 27 the number of cycles to fail zone i (N_{fi}), can be obtained. This equation is used for the rest of the zones that form the process zone until a crack of the

length of the process zone is formed. By doing so, the DCSE that is accumulated along the crack is calculated. Finally, when the DCSE limit is reached, the crack length that was originally specified is produced. As a result, the number of loads to propagate a determined crack length is predicted.

As a consequence, following the fracture mechanics threshold principles, the key parameters that appear to control cracking performance of HMA are: DCSE, m-value and D_1. The *m-value* is the parameter that controls the creep strain rate at low temperatures. A lower *m-value* is desirable because the lower the rate of accumulation of DCSE will be, hence the less fast the threshold value will be reached. Besides these parameters, the tensile stress governs the location and how fast a crack initiates and propagates depending on the pavement configuration. Therefore, it is reasonable to account for all these factors when determining the moisture damage of a mix, rather than solely focusing on one property (2, 17).

Birgisson, Roque, and Page (17) proposed the use of the "Energy Ratio" (ER), as a parameter to assess the mix resistance to moisture damage. Jajliardo (25) was able to determine a minimum DCSE for adequate cracking performance and also proposed a minimum required ER for different traffic levels. This ratio was developed based on forensic research of 36 field pavement sections of known cracking performance and is a function of the parameters that were previously mentioned:

$$ER = \frac{DCSE_f}{DCSE_{\min}} = \frac{a \cdot DCSE_f}{m^{2.98} \cdot D_1} \tag{28}$$

where

$DCSE_f$ = Dissipated creep strain energy to fracture (KJ/m^3),

$DCSE_{min}$= Minimum dissipated creep strain energy for adequate cracking performance (KJ/m^3),

D_1 and m = parameters obtained from creep test (1/psi),

$a = 0.0299\ \sigma^{-3.1}\ (6.36\text{-}S_t) + 2.46 \times 10^{-8}$,

σ = tensile stress of asphalt layer (psi),

S_t = tensile strength (MPa)

The rationale behind the HMA fracture mechanics framework for studying water damage is to account for different key mixture properties that are affected by moisture. Hence this framework demonstrates that moisture damage can not be assessed based only on one property such as the resilient modulus itself.

Relationship between Air Void Size, Pore Pressure Distribution and Moisture Damage

The air void distribution and pore pressure distribution were studied in order to determine their relationship to moisture damage. Moisture damage was assessed by the change in energy ratio (ER) and number of cycles to failure due to moisture conditioning.

Energy Ratio

As previously explained, the energy ratio can be used to determine the moisture sensitivity of asphalt mixes that is reflected in their cracking performance. Therefore, the energy ratio (ER) was calculated using Equation 28 with an average tensile stress of

the asphalt layer equal to 120 psi. This tensile stress is a common value obtained for Florida pavements which have a thin layer of HMA and a stiff base. Tables 24 and 25 show the calculated ratios.

TABLE 24 Mechanical data for conditioned and unconditioned granite SGC specimens, (17)

Label	m-value	D_1	DCSE (kJ/m^3)	ER	a
GA-C1 (C)	0.66	1.54E-06	2.75	0.50	8.08E-08
GA-C2 (C)	0.65	1.03E-06	2.60	0.67	7.31E-08
GA-C3 (C)	0.6	9.10E-07	1.93	0.62	7.38E-08
GA-C1 (U)	0.62	1.74E-06	5.80	1.07	7.73E-08
GA-C2 (U)	0.59	1.06E-06	4.77	1.57	7.13E-08
GA-C3 (U)	0.57	8.70E-07	3.60	1.55	7.14E-08
GA-F1 (C)	0.63	1.52E-06	2.62	0.53	7.57E-08
GA-F2 (C)	0.56	1.24E-06	2.11	0.70	7.18E-08
GA-F3 (C)	0.6	1.44E-06	1.91	0.42	7.40E-08
GA-F1 (U)	0.57	1.30E-06	3.48	1.06	7.21E-08
GA-F2 (U)	0.48	1.58E-06	3.29	1.22	6.58E-08
GA-F3 (U)	0.56	8.97E-07	2.57	1.16	6.98E-08

TABLE 25 Mechanical data for conditioned and unconditioned limestone SGC specimens, (2)

Label	m-value	D_1	DCSE (kJ/m^3)	ER	a
WR-C1 (C)	0.44	1.50E-06	2.07	1.25	7.9E-08
WR-C2 (C)	0.59	1.03E-06	1.79	0.65	7.9E-08
WR-C3 (C)	0.54	5.75E-07	1.47	1.19	7.5E-08
WR-C1 (U)	0.54	9.51E-07	2.35	1.18	7.6E-08
WR-C2 (U)	0.67	7.65E-07	1.81	0.62	7.9E-08
WR-C3 (U)	0.43	7.84E-07	1.83	2.09	7.2E-08
WR-F1 (C)	0.73	9.13E-07	4.00	0.85	7.6E-08
WR-F2 (C)	0.67	9.49E-07	2.88	0.77	7.6E-08
WR-F3 (C)	0.69	4.08E-07	1.73	0.97	7.4E-08
WR-F1 (U)	0.60	1.16E-06	4.00	1.20	7.6E-08
WR-F2 (U)	0.54	1.01E-06	2.90	1.31	7.3E-08
WR-F3/C4 (U)	0.53	7.08E-07	2.50	1.65	7.2E-08

Figures 23 and 24 show the differences between the ER of the conditioned and unconditioned SGC specimens. As pointed out by Birgisson et al (2), it can be inferred from these graphs that the change in the ER from a wet to a dry stage is more dramatic for the granite than for the limestone. Even though the ER of gradation C2 for the granite was better than for the limestone in a dried condition, it turned to be worse when conditioned because it decreases dramatically while the ER of the limestone remains about the same.

According to the ER ratio of the conditioned ER to the unconditioned ER overall, the granite is more susceptible to moisture damage than the limestone is, as it can be seen in Figure 25.

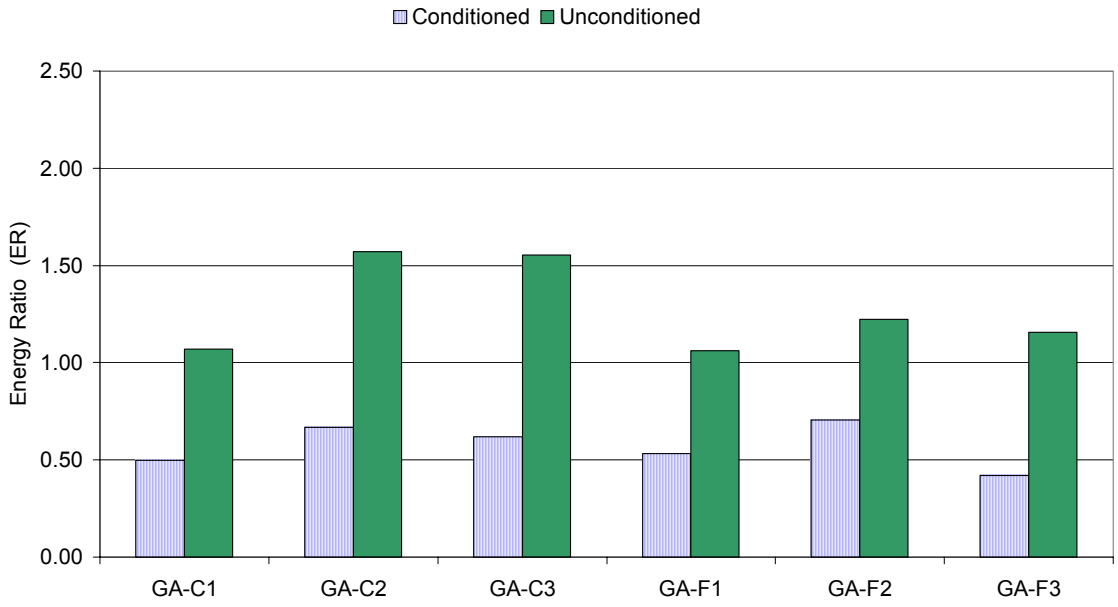

Figure 23 Conditioned vs. unconditioned energy ratios (ER) for granite SGC mixes (17).

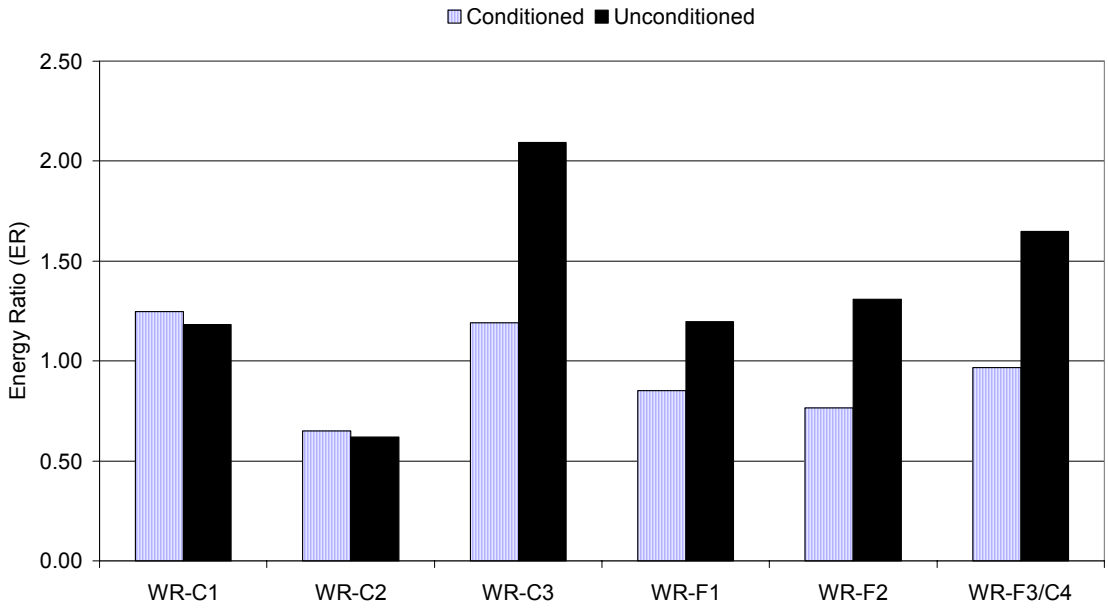

Figure 24 Conditioned vs. unconditioned energy ratios (ER) for limestone SGC mixes (2).

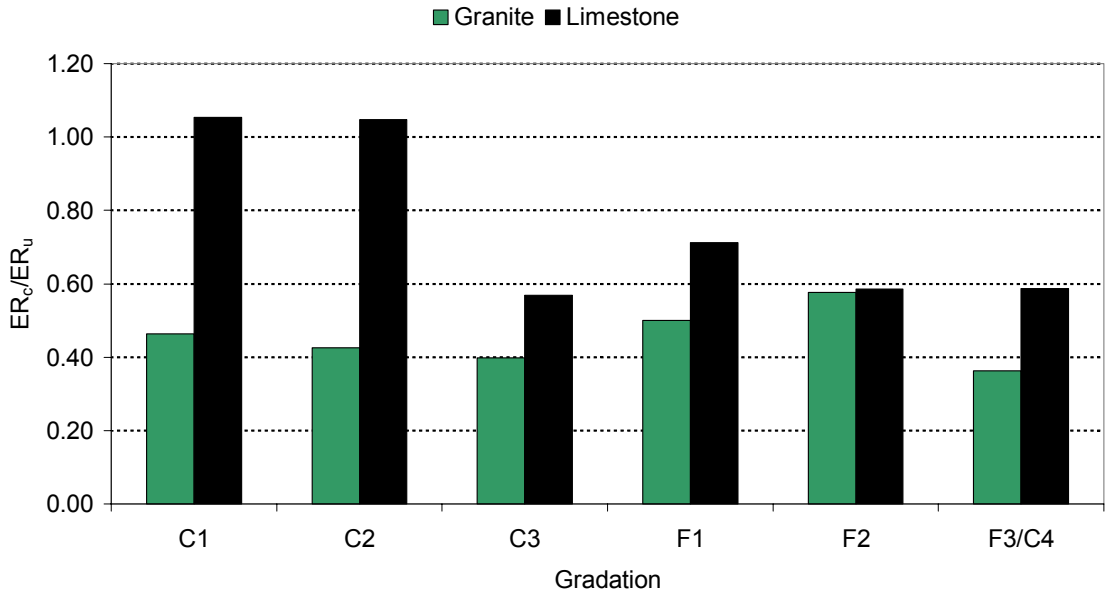

Figure 25 Comparison between SGC granite and limestone ER ratios.

Number of Load Cycles to Failure Ratio

As previously explained, the ratio of conditioned to unconditioned number of load cycles to failure can be used to assess moisture damage. Figure 26 shows the change in this ratio for the specimens that were studied. As can be seen, most of the limestone mixes exhibit a larger N ratio compared to the granite mixes. Also for those in which the N ratio is larger for the granite mixes, the difference is small compared to those for the limestone mixtures.

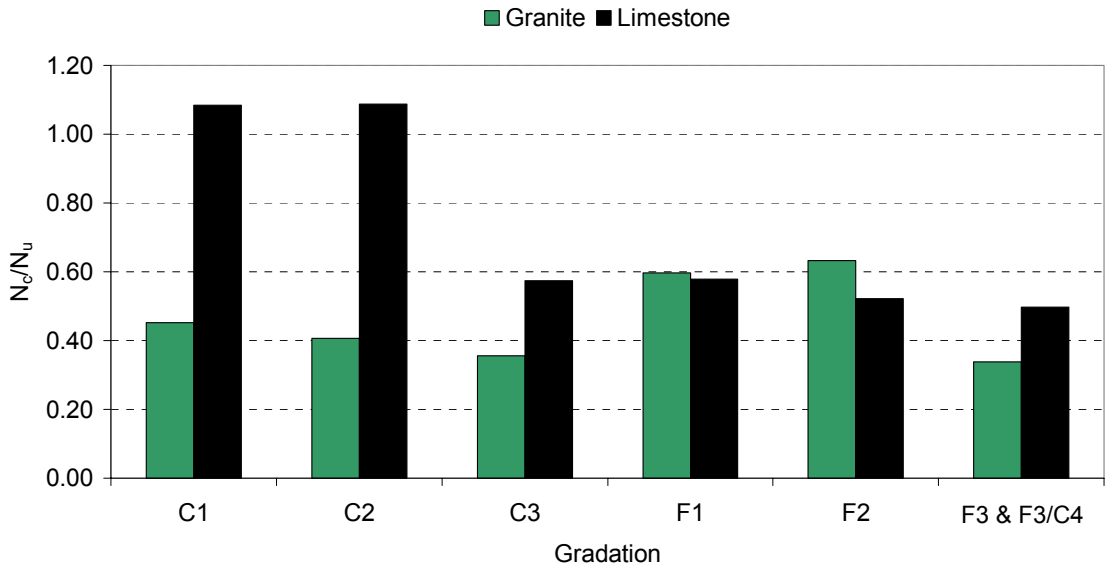

Figure 26 Comparison between SGC granite and limestone N ratios (2).

Air Void Analysis

The air void distribution for the granite and limestone specimens were determined from square images that were extracted from the original circular section which had a diameter of 100 mm. These square sections were obtained by using a macro that cuts most of the area of the specimen that could be covered. The resulting images had a side of 70.3 mm but its resolution was kept as the original image so that better results could be obtained.

Even though the mix design of the mixtures was the same, the air void distribution shows that there is a significant difference among the corresponding specimens when analyzing the quartiles. The differences in the quartiles of each pair of

analogous gradations of the SGC granite and limestone specimens (Granite air void Size – Limestone Air Void Size) are shown in Figure 27. The difference is always positive indicating larger voids in the granite mixes. It can be inferred from this figure that even though the corresponding coarse and fine gradations are approximately the same, their air void distribution is not identical. This is especially true for the coarse gradations.

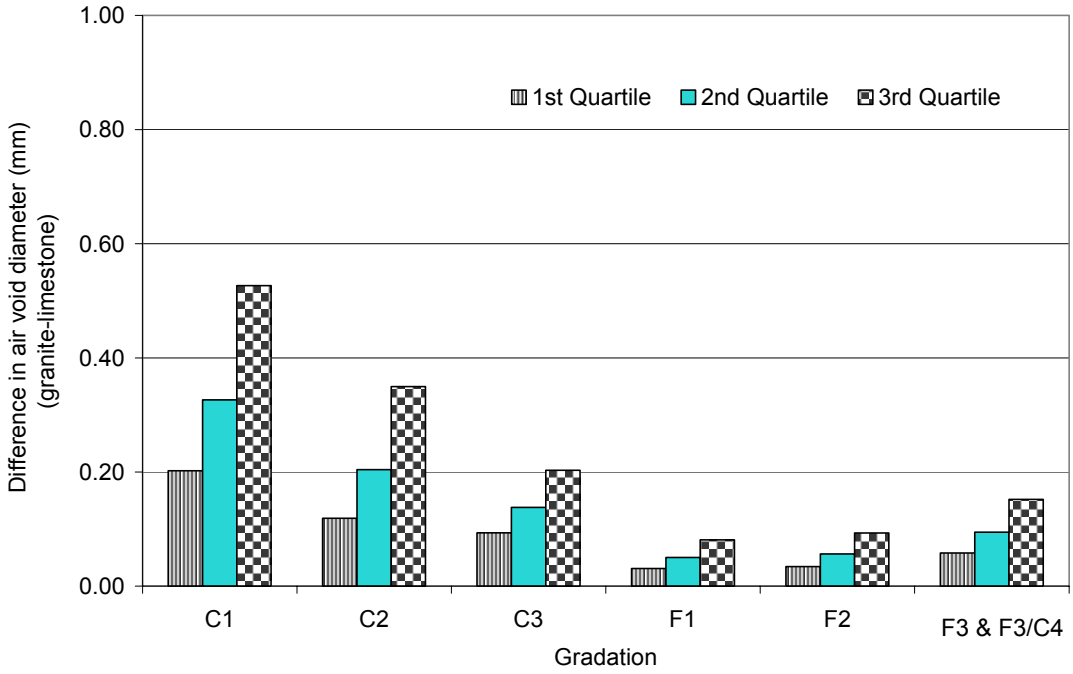

Figure 27 Air void quartile difference between granite and limestone gradations.

Figure 28 shows how the three dimensional air voids differ for the SGC granite and limestone specimen that have similar gradations (i.e. GA-C1 and WR-C1). Consequently an additional analysis was done using the AIMS software to study the angularity of particles that passed sieve #4 and that were retained in sieve #8. This

software analyses the angularity on black and white images of aggregate particles using two methods: the gradient method and the radius method (26). The results from the gradient method were considered in this study due to the fact that it captures a wider range of measurements in comparison to the radius method. The principle behind the gradient method consists on measuring the gradient vector direction for adjacent points on the outline of the particles. The gradient values for all the corners is determined and accumulated in order to calculate the angularity gradient for the particle. More details about this method are given by Chandan et al (27).

Three measurements were done for each aggregate. The average results are included in Table 26. It can be inferred from these measurements that the limestone has less rounded particles than the granite does. Hence, the interlocking of the limestone particles is greater, leading to form air voids that are smaller than the voids that are formed with the granite. Angularity could be therefore, a good explanation for having larger air voids for all the SGC granite specimens than for the SGC limestone specimens even though both were prepared with the same gradation.

TABLE 26 Aggregate angularity measurements

Particles	Granite	Limestone
Mean	3493.38	3736.82
% Rounded Particles	19.63	11.22
% Sub-Rounded Particles	47.61	48.81
% Sub-Angular Particles	20.40	26.48
% Angular Particles	12.37	13.48

It is also apparent that the granite mixture has larger air voids. Figure 29 shows three dimensional cubical sections from two granite specimens that have a coarse gradation and a fine gradation. The air voids of the coarse gradation are larger than those of the fine gradation.

According to the Pearson correlation coefficient, the air void distribution can be described with a Lognormal distribution; the histograms of these data are shown in Figures 30 and 31 respectively. The distribution is shifted more towards the right in coarse mixes compared with fine mixes. This indicates that a specimen with a coarse gradation has larger voids than fine graded mixes.

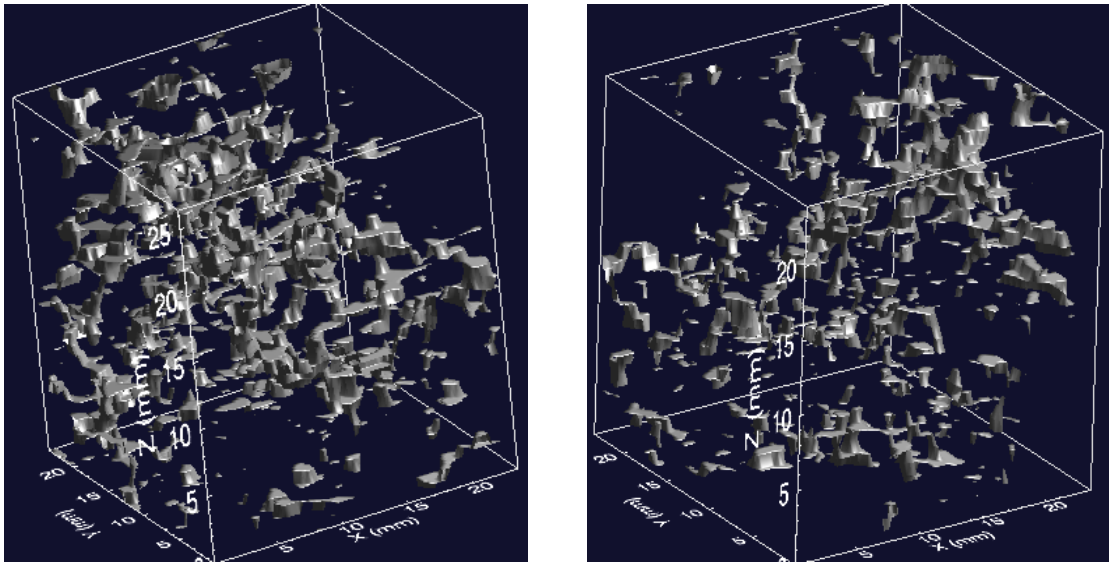

(a) **(b)**

Figure 28 Three dimensional air voids of SGC specimen section for mixtures: (a) GA-C1, and (b) WR-C1.

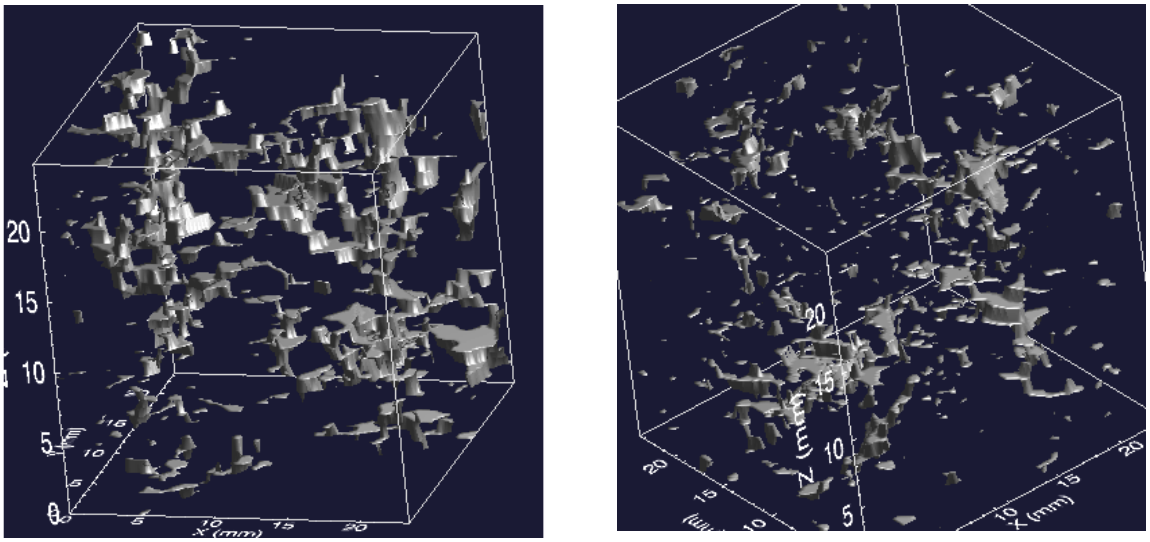

(a) **(b)**

Figure 29 Three dimensional air void of SGC specimen section for mixtures: (a) GA-C2, (b) GA-F2.

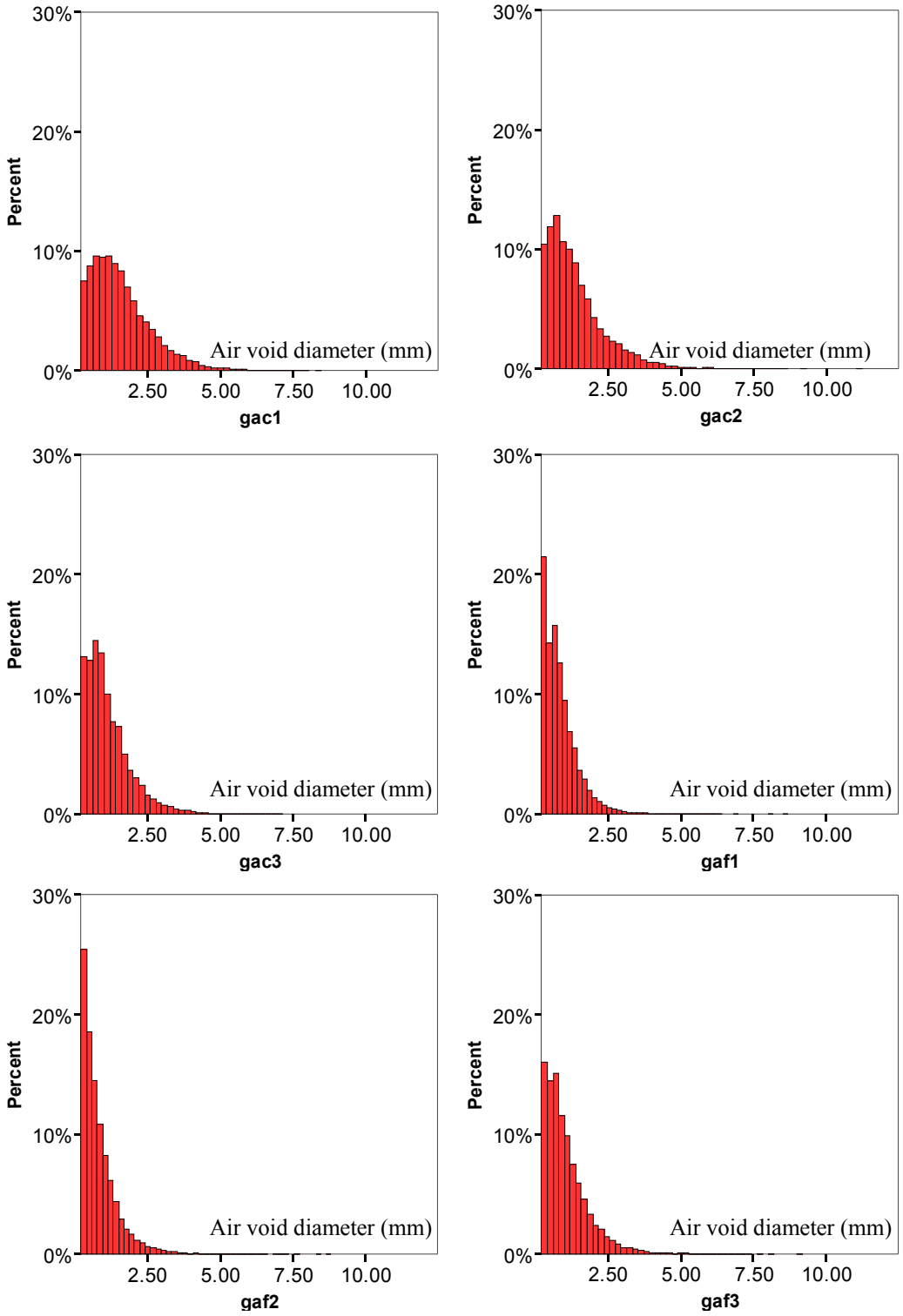

FIGURE 30 Air Void distribution for SGC granite specimens.

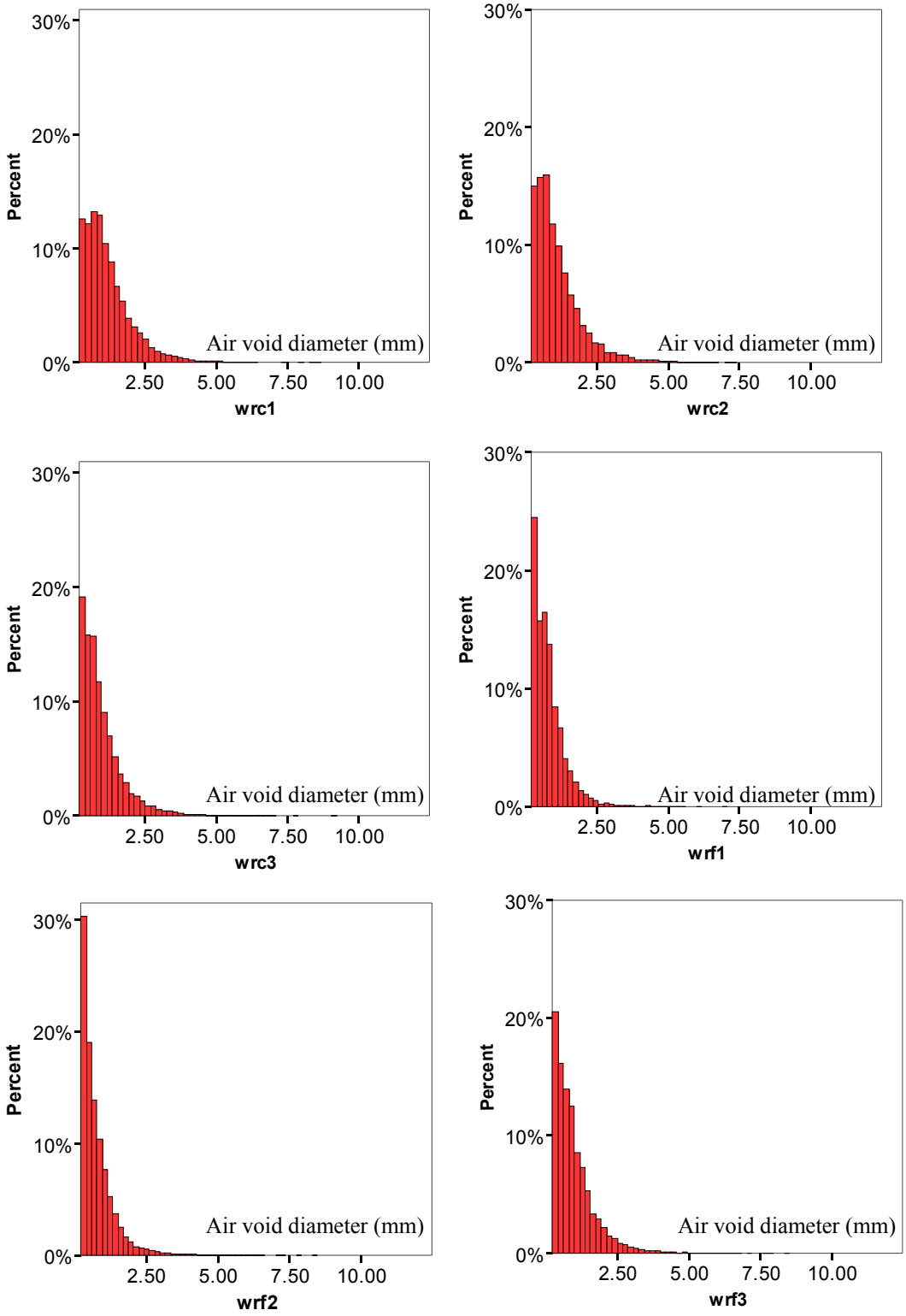

Figure 31 Air void distributions for SGC limestone specimens.

In order to relate the air void distribution to moisture damage, the mean diameter size was compared to ratios of the number of cycles to failure and energy ratios of the conditioned to the unconditioned specimen. A polynomial regression trend line was used to fit the data because it gave a better correlation coefficient than other regression types. The relationships found between the average air void diameter and ER and N ratios, for the granite SGC specimens are shown in Figures 32 and 33. For the granite specimens, the N and ER ratios decrease with an increase in void size until they reach a "pessimum" point after which these ratios start to increase with an increase in void size.

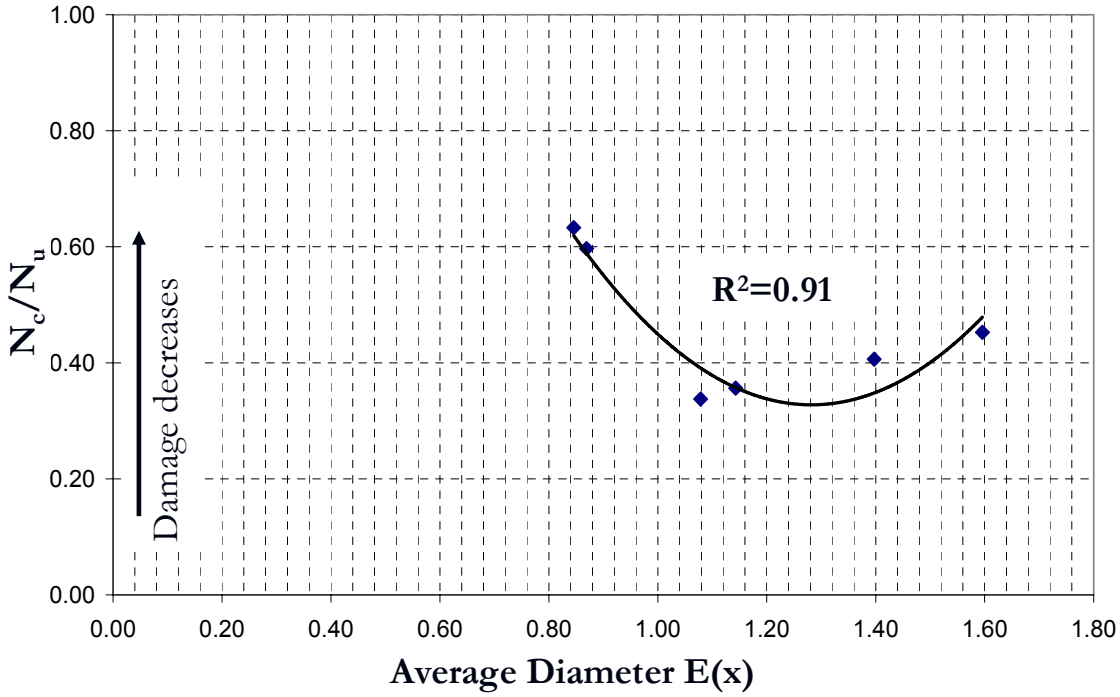

Figure 32 Average diameter vs. N ratio for SGC granite specimens.

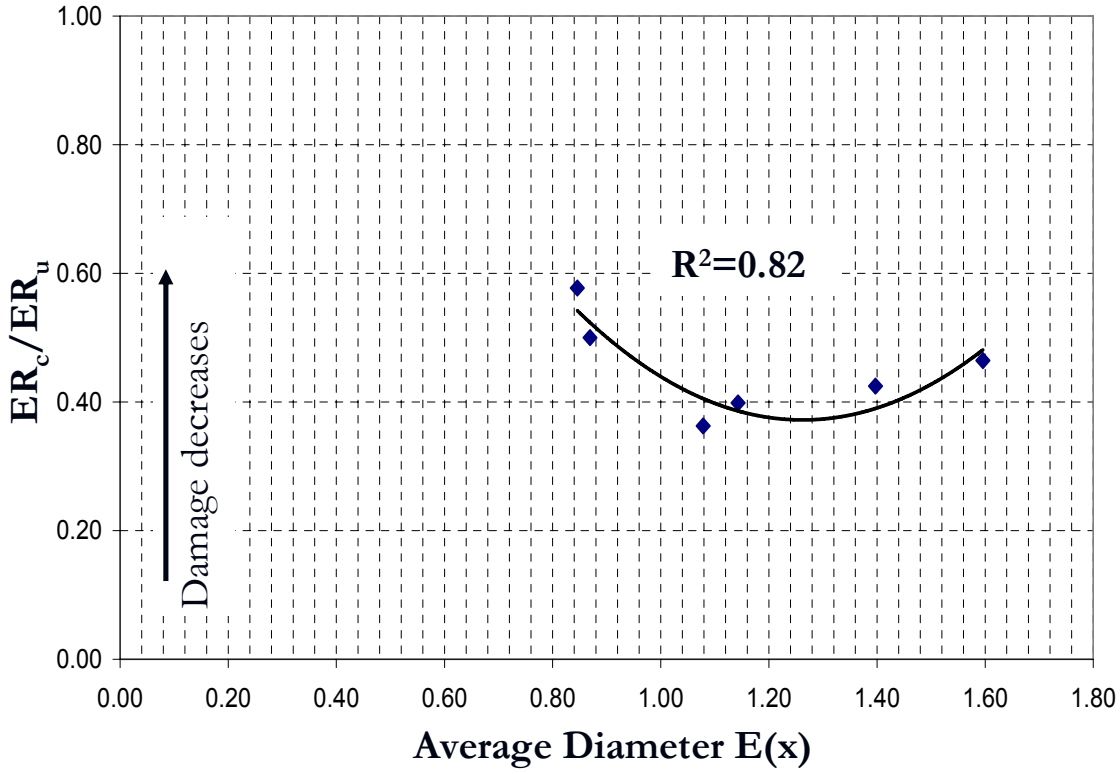

Figure 33 Average diameter vs. ER ratio for SGC granite specimens.

The relationships between the N and ER ratios and the air void size for SGC limestone mixes are shown in Figures 34 and 35. The relationship has the same form, as the SGC granite mixes, but, it is not as clear as distinct as the granite mixes.

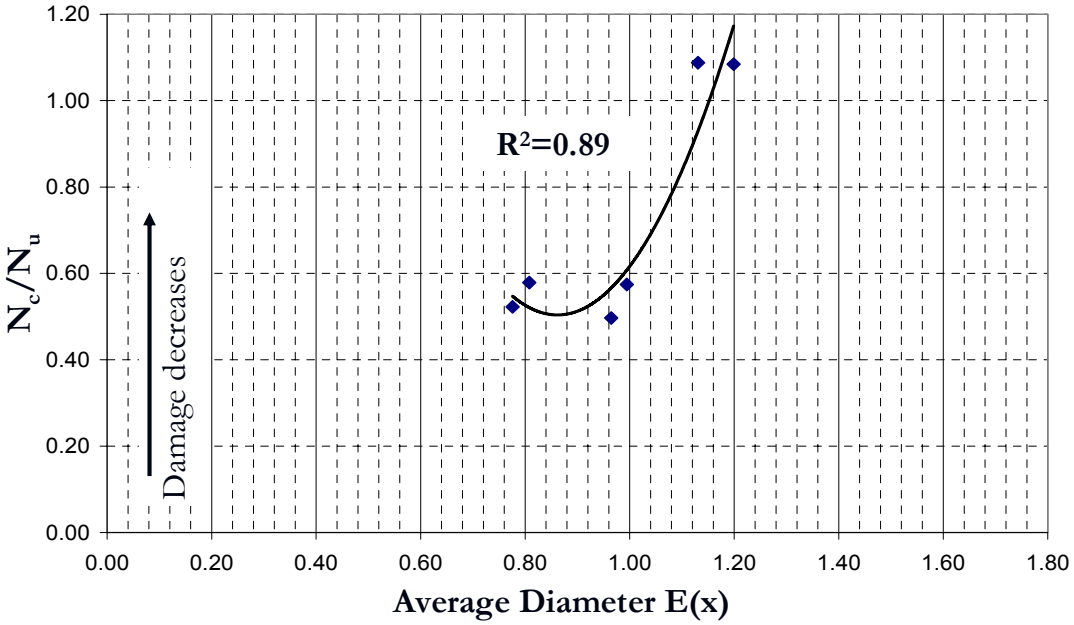

Figure 34 Average diameter vs. N ratio for SGC limestone specimens.

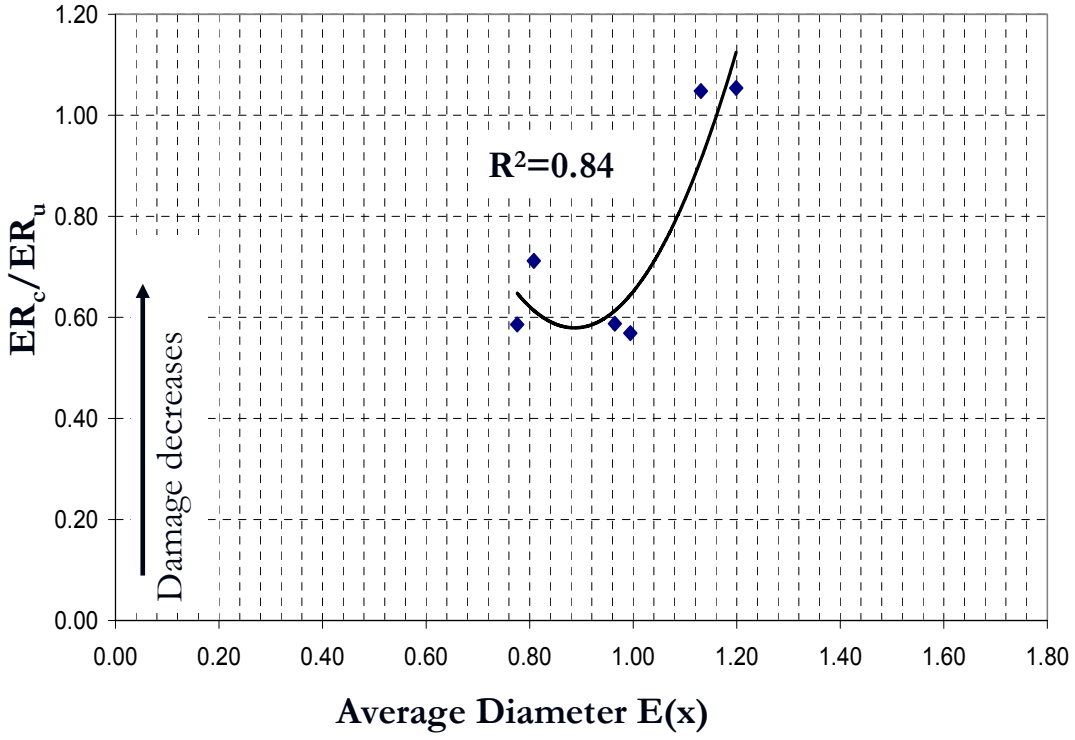

Figure 35 Average diameter vs. ER ratio for SGC limestone specimens.

From these patterns it can be inferred that there is an average diameter size that becomes critical in terms of moisture damage. This idea was first established by Terrel et al. (28, 29). These authors found that there are three air void content ranges that affect the strength of a mixture differently. These ranges correspond to a low (impermeable), "pessimum" (intermediate), and high (free drainage) air void contents as shown in Figure 36. Based on the results in Figures 32, 33, 34 and 35, this concept can be applied to the average size of air void at a given percent air voids.

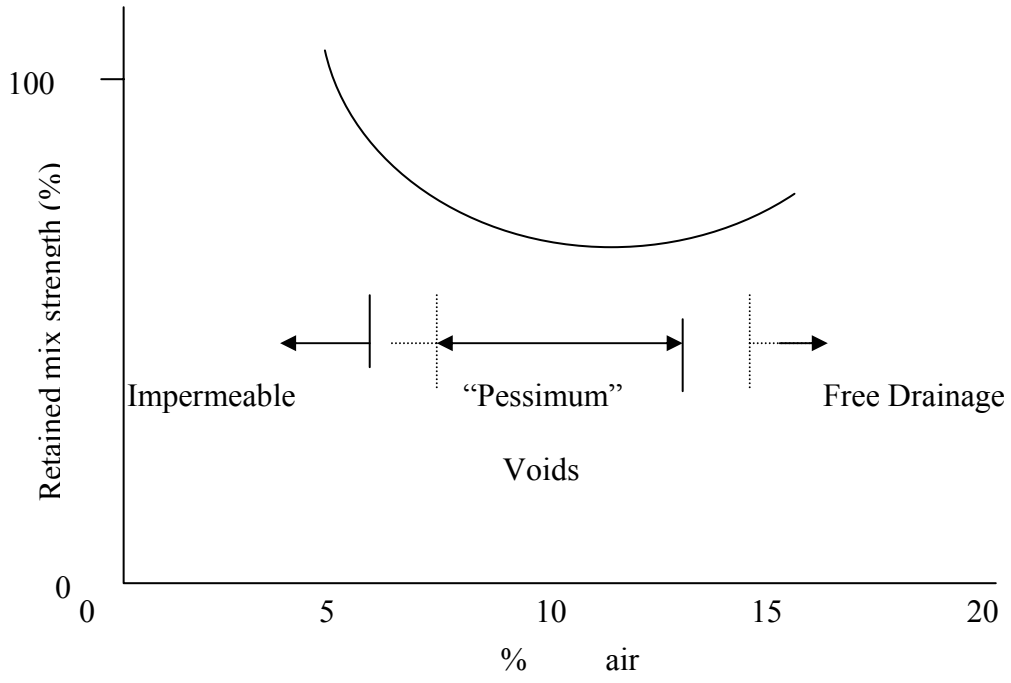

Figure 36 Dependence of relative strength of mixtures on access to water in void system (28).

Following this concept and based on the results shown in the previous graphs, the granite cores show a better behavior in regard to the ER and N ratios for air void

sizes that are outside the range between 1.2 and 1.4 mm; whereas for the limestone cores, the performance improves when the average diameter of the voids is away from the range between 0.8 and 1.0 mm.

Pressure Distribution

Pore fluid plays an important role in the failure of porous media. If fluid is not present, the medium will fail like a solid when the acting stress exceeds a certain limit. However, due to the presence of interstitial fluid, the mode of failure that can happen has been recognized by Terzaghi as "splitting" failure. This type of failure originates the tensile breakdown of the medium, due to the effect of the fluid pressure (4).

Furthermore, one of mechanisms theorized for stripping suggests that pore pressure causes the asphalt film to strip from the aggregate because during the initial densification of the pavement structure due to traffic loading, the percolating water can get trapped in impermeable voids. Hence, stripping can be generated due to high pore water pressure that may develop as a consequence of further loading and environmental cycling.

The pressure distribution was determined through the use of a three dimensional fluid flow model developed by Al-Omari and Masad (10). The main purpose of this model is to determine the fluid flow characteristics and permeability when a fixed stress is applied to the specimen in a particular direction under saturated condition. Furthermore, it records the pressure at each point of the microstructure where water percolates. This model runs in a Fortran code that uses as input the bitmap from the image analysis of square sections that are taken from the original images, because it

works with a finite difference numerical scheme in which the control volume is chosen to have square images (10). Also, a hydraulic gradient is introduced so that water could flow from the inlet to the outlet of the microstructure.

The statistical analysis of the pore pressure distribution showed that there is difference in the developed pressure distribution among specimens as shown in Figures 37 and 38. However, there was apparent no relationship between the calculated N and ER ratios and pressure distribution. This is not surprising given that the measurements associated with the calculation of these ratios were conducted after pore pressure was released, (2).

Nonetheless, the results show that different pore pressure distributions can result due to the difference in mixes in terms of aggregate size distribution and aggregate type. As a matter of fact, it was reported that the limestone mixes took a long time to release the pore water. This was found by determining the time lapsed for the conditioned modulus to recover 95 percent of the unconditioned small strain modulus which usually increases when the saturation level decreases (2).

As can be seen in Figure 39, the difference between the average air void pressures among corresponding gradations was always greater for the limestone cores than for the granite cores, except for the mix F1. Therefore, generally more pressure is associated with longer time of retention of the interstitial water.

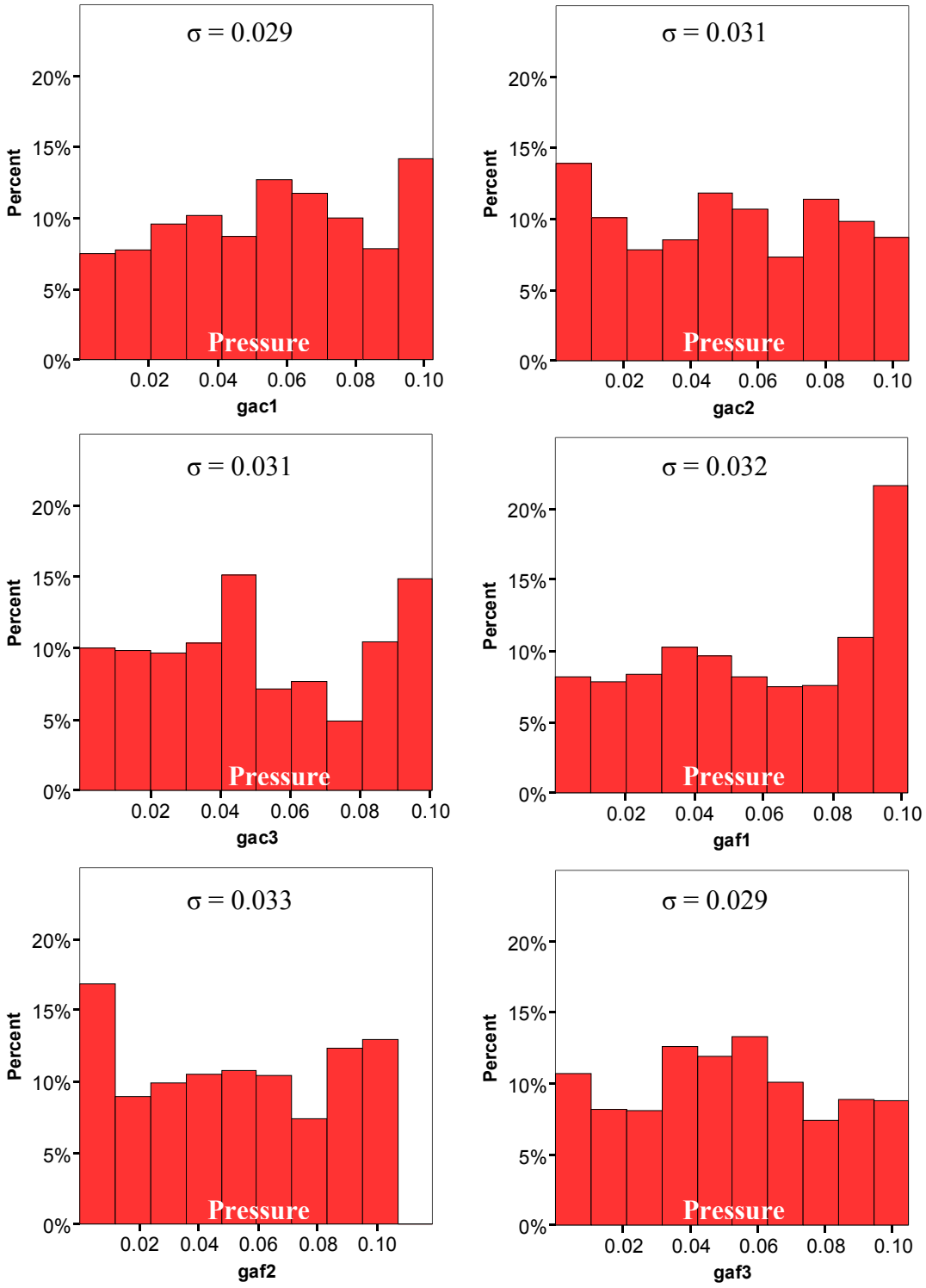

Figure 37 Pressure distributions for SGC granite specimens.

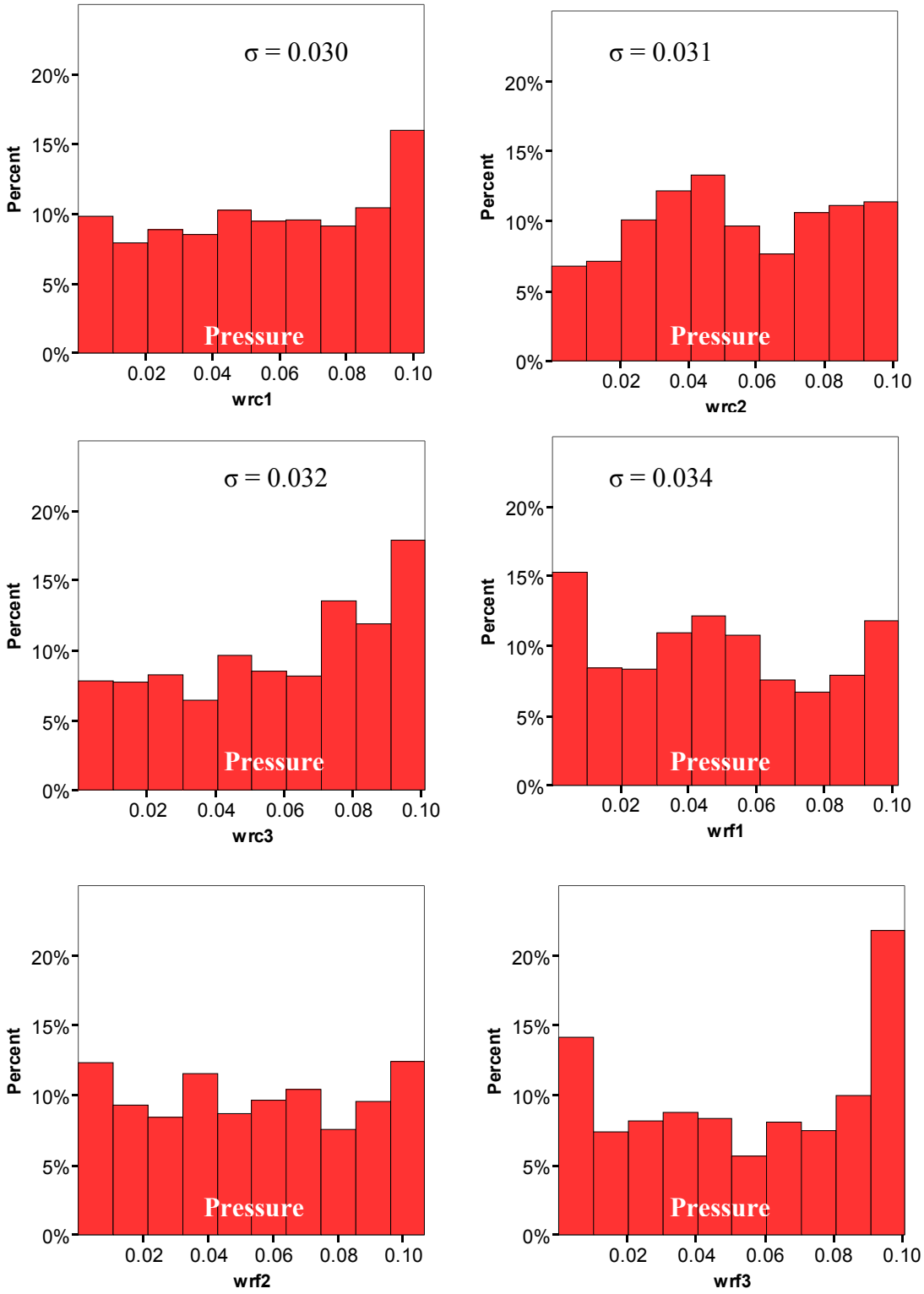

Figure 38 Pressure distributions for SGC limestone specimens.

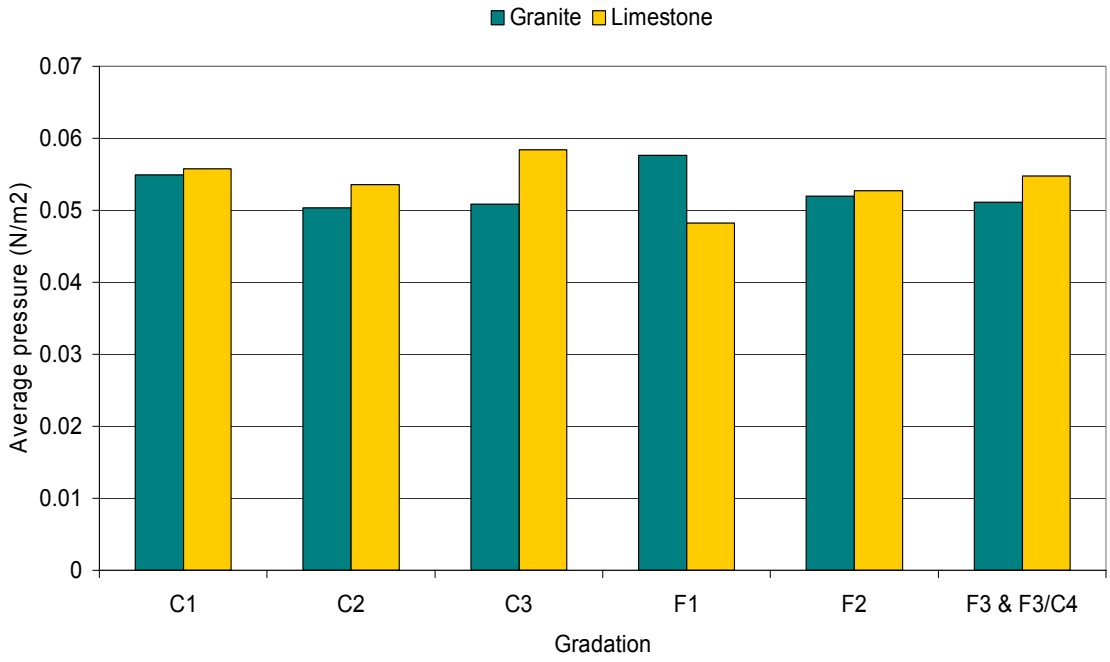

Figure 39 Comparison of average air void pressure between SGC specimens with different aggregates.

Surface Energy and Bond Strength

The surface energy can be defined as the energy that is required to create a new unit area of surface of the same material under a vacuum (13). In summary, it requires surface energy to initiate and propagate a microcrack through the HMA structure. If the energy needed to cause that fatigue damage is relatively high, then the HMA is considerably resistant to fracture. Conversely, if the HMA does not have much energy to heal then it can be said, that the HMA does not have sufficient potential to self heal.

Schapery's fundamental law of fracture explains this surface energy as a balance between the strain energy that is released when a crack propagates and the energy that is necessary to surmount the viscous resistance of the material where the energy is released

(13). Additionally, the surface energy of a material is always formed by two components regardless if its fracture is adhesive or cohesive: an apolar component (Lifshitz-van der Waals component) and a polar component (acid-base component). Therefore, the total surface energy that governs the fracture of the material can be expressed as (13):

$$\Delta G = \Delta G^{LW} + \Delta G^{AB} \tag{29}$$

where

ΔG= total surface free energy of the asphalt or aggregate,

ΔG^{LW}= Lifshitz-van der Waals apolar component of the total surface free energy,

ΔG^{AB}= Acid-base polar component of the total surface free energy

For *adhesion* and *without the presence of water*, the LW component is calculated as:

$$\Delta G^{LW} = -\Gamma_{ij}^{LW} + \Gamma_i^{LW} + \Gamma_j^{LW} \tag{30}$$

Where,

$$\Gamma_{ij}^{LW} = \left(\sqrt{\Gamma_i^{LW}} - \sqrt{\Gamma_j^{LW}}\right)^2 \tag{31}$$

with

Γ^{LW}_i= Lifshitz-van der Waals component of Gibbs free energy of the asphalt

Γ^{LW}_j= Lifshitz-van der Waals component of Gibbs free energy of the aggregate

And the acid-basic component is calculated as follows:

$$\Delta G^{AB} = -\Gamma_{ij}^{AB} + \Gamma_i^{AB} + \Gamma_j^{AB} \tag{32}$$

$$\Gamma_{ij}^{AB} = 2\left(\sqrt{\Gamma_i^+} - \sqrt{\Gamma_j^+}\right)\left(\sqrt{\Gamma_i^-} - \sqrt{\Gamma_j^-}\right) \tag{33}$$

Additionally the acid-basic component of the material *i* and *j*, Γ_i^{AB} and Γ_j^{AB} are expressed as:

$$\Gamma_i^{AB} = 2\sqrt{\Gamma_i^+\Gamma_i^-} \quad and \quad \Gamma_j^{AB} = 2\sqrt{\Gamma_j^+\Gamma_j^-} \tag{34}$$

Where, Γ^+ is the acid component and Γ^- the basic component. The sub indices *i* and *j* stand for asphalt and aggregate respectively.

The *cohesive* surface energy of the asphalt, when no water is present is expressed as (13):

$$\Delta G_i = \Delta G_i^{LW} + \Delta G_i^{AB} \tag{35}$$

where

$$\Delta G_i^{LW} = 2\Gamma_i^{LW} \tag{36}$$

$$\Delta G_i^{AB} = 2\Gamma_i^{AB} \tag{37}$$

When water (*k*) is present between the interface of asphalt and aggregate, the apolar and polar components of the *adhesive* surface energy on the interface can be calculated as (13):

$$\Delta G^{LW}_{ikj} = 2\Gamma_k^{LW} + 2\sqrt{\Gamma_i^{LW}\Gamma_j^{LW}} - 2\sqrt{\Gamma_i^{LW}\Gamma_k^{LW}} - 2\sqrt{\Gamma_j^{LW}\Gamma_k^{LW}} \tag{38}$$

$$\Delta G^{AB}_{ikj} = 4\sqrt{\Gamma_k^-\Gamma_k^+} - 2\sqrt{\Gamma_k^-}\left(\sqrt{\Gamma_i^+} + \sqrt{\Gamma_j^+}\right) - 2\sqrt{\Gamma_k^+}\left(\sqrt{\Gamma_i^-} + \sqrt{\Gamma_j^-}\right) + 2\sqrt{\Gamma_i^-\Gamma_j^+} + 2\sqrt{\Gamma_i^+\Gamma_j^-} \tag{39}$$

Therefore the total Gibbs adhesive bond strength is (13):

$$\Delta G_{ikj} = \Delta G_{ikj}^{LW} + \Delta G_{ikj}^{AB} \quad (40)$$

Additionally, the *cohesive* surface energy on the interface when water is present can be calculated as expressed in Equations 38 and 39 by replacing Γ_j for Γ_i.

The Wilhelmy plate method is used to measure the contact angles that a film of asphalt forms with three different solvents (30). On the other hand, the surface energy of the aggregate are indirectly measured with the Universal Sorption Device (USD) method that is based on the equilibrium spreading pressure of the adsorbed vapor, on the aggregate surface (30). From these procedures it is possible to calculate the energy components, Γ^{LW}, Γ^{+}, and Γ^{-} of the asphalt and the aggregate. These two procedures will be described in the following sections.

Every material has two different sets of surface energy components, depending on the process. The wetting energy predicts the healing capacity of the material while the dewetting energy predicts fracture. These energy components can be calculated applying the theory of surface energies and contact angles developed by Good and van Oss (1991) for both, adhesive and/or cohesive fractures. Present research by Little et al. (30), demonstrated that the acid base components of surface energy affect healing in a positive way, meaning that the higher this component is, the more healable the material is. On the other hand, the Lifshitz-van der Waals component affects healing negatively.

The surface free energies of the Georgia granite, the Florida limestone, and the asphalt used to prepare the mixtures, were measured to better understand the damage that the mixtures experience due to the presence of water.

Asphalt

The asphalt used to prepare both types of mixes was a PG 67-22. The Wilhelmy Plate method was used to measure the dynamic contact angles between a film of asphalt and four different solvents of known surface energy components: diiodomethane, distilled water, formamide, and glycerol. These solvents were chosen because of their fairly large surface energies, immiscibility with asphalt, and different surface energy components.

Young-Dupre's equation (Equation 41) can be used in order to calculate the surface free energy of the asphalt from the dynamic contact angles, under the assumption that the equilibrium film pressure can be neglected for asphalt (26):

$$\Gamma_s(1+\cos\theta_i) = 2\sqrt{\Gamma_i^{LW}\Gamma_s^{LW}} + 2\sqrt{\Gamma_i^-\Gamma_s^+} + 2\sqrt{\Gamma_i^+\Gamma_s^-} \tag{41}$$

In this equation, θ_i is the contact angle that is formed between the asphalt and the solvent, *s*. θ_i, is related to two different sets of surface energy processes, (i.e. wetting and dewetting) which are used to predict healing and fracture respectively. When the asphalt film is introduced into the solvent, the advancing angle is measured and the wetting surface energy can be calculated. On the other hand, the dewetting surface energy is associated with the receding angle that the asphalt film forms with the solvent when it is withdrawn. Figure 40 shows a schematic of the Wilhemy plate method.

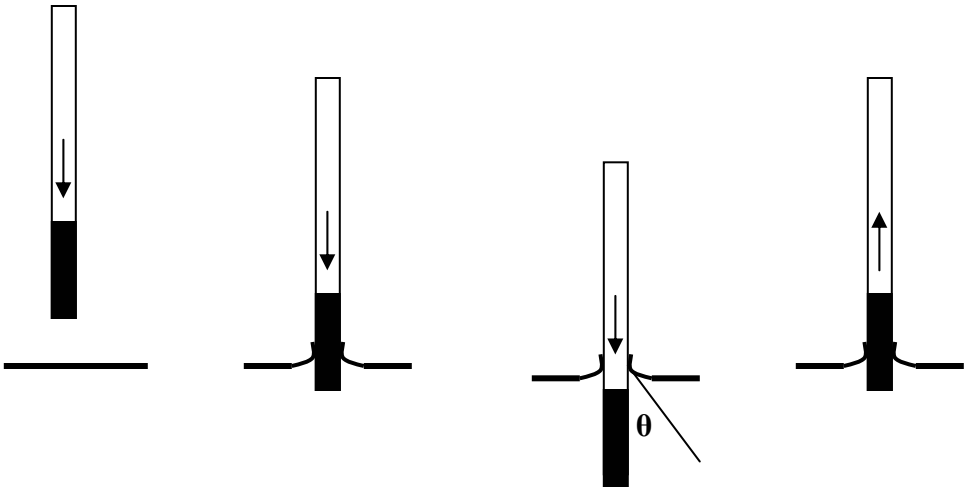

Figure 40 Wilhelmy Plate method procedure.

As can be seen in Equation 41, there are three unknowns (i.e. Γ^{LW}, Γ^{+}, and Γ^{-}). Therefore at least three different solvents of known surface energies must be used so that the different components of the asphalt surface energy can be determined from solving the linear system of equations. This can be more clearly represented through a matrix as shown below:

$$\begin{bmatrix} a_{11} & a_{12} & a_{13} \\ a_{21} & a_{22} & a_{23} \\ a_{31} & a_{32} & a_{33} \end{bmatrix} \begin{bmatrix} x_1 \\ x_2 \\ x_3 \end{bmatrix} = \begin{bmatrix} Y_1 \\ Y_2 \\ Y_3 \end{bmatrix} \tag{42}$$

where

$$a_{1i} = 2\frac{\sqrt{\Gamma_s^{LW}}}{\Gamma_s},\ a_{2i} = 2\frac{\sqrt{\Gamma_s^{+}}}{\Gamma_s},\ a_{3i} = 2\frac{\sqrt{\Gamma_s^{-}}}{\Gamma_s} \tag{43}$$

$$x_1 = \sqrt{\Gamma_a{}^{LW}},\ x_2 = \sqrt{\Gamma_a{}^{+}},\ x_3 = \sqrt{\Gamma_a{}^{-}} \tag{44}$$

$$Y_i(x) = 1 + Cos\,\theta_i \tag{45}$$

with

a_{ni} = Known surface energy components of the solvent *i,*

x_i = Unknown surface energy components of the asphalt,

$Y_i(x)$= Known Function of the measured contact angles (θ_i), between asphalt and solvent *i*.

From the four solvents that were initially used to measure the contact angles, only three were chosen because they gave the least variation in the surface energy of the asphalt. These were diiodomethane, distilled water and glycerol. The surface energy components of the solvents that were used are summarized in Table 27.

TABLE 27 Surface free energy components of solvent liquids (ergs/cm^2)

Solvent	Γ^{LW}	Γ^{+}	Γ^{-}	Γ
Diidomethane	50.8	0	0	50.8
Glycerol	34	3.92	57.4	64
Distilled Water	21.8	25.5	25.5	72.8

As seen in Table 28, the accuracy of the measurements taken with the Wilhelmy Plate is very good based on the standard deviation calculated from three measurements. Also, the coefficient of variation demonstrates that the assurance on the measurements is good for a 95 percent level of confidence.

TABLE 28 Advancing and receding contact angles measured with the Wilhelmy Plate method

	WATER		GLYCEROL		methylene iodide	
	Advancing Angle	Receding Angle	Advancing Angle	Receding Angle	Advancing Angle	Receding Angle
Average	95.32	68.66	88.53	59.83	72.14	35.05
Standard Deviation	2.13	1.16	2.14	2.02	2.97	2.17
Coefficient of variation	0.02	0.02	0.02	0.03	0.04	0.06

The calculation of the linear system of equations was done by using a program developed by Della Volpe and Siboni (31) that uses the original scale with variable errors of contact angles, developed by van Oss, Chaudury and Good. These values are included in Table 29 and are displayed in Figure 41.

.

TABLE 29 Healing and fracture energy components of the asphalt

Component	Wetting		Dewetting	
	(ergs/cm^2)	S.D.	(ergs/cm^2)	S.D.
Γ^{LW}	21.68	0.65	42.01	0.91
Γ^{+}	0.05	0.07	0.23	0.16
Γ^{-}	4.05	0.44	11.28	0.73
Γ^{AB}	0.9		3.22	
Γ	22.58	2.05	45.23	3.29

From these energy components, it can be inferred that the non polar (LW) component is much larger than the polar component (acid-base). The high value of the non polar component can be explained by aging of the asphalt. However, there is no information about this effect.

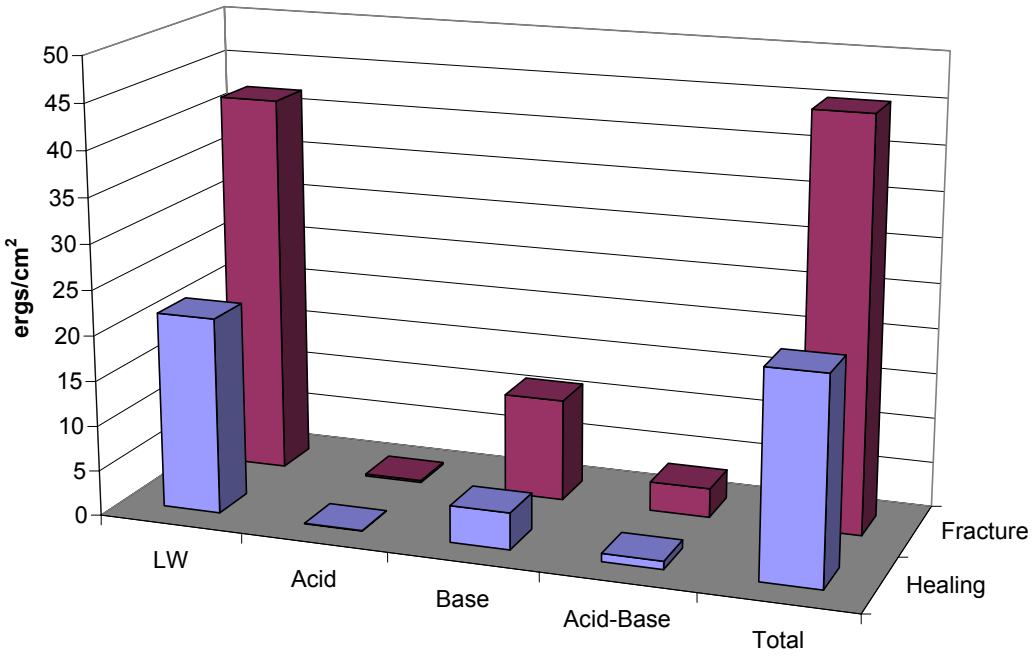

Figure 41 Surface energy components of asphalt PG67-22.

It is noted that the acidic component Γ^{+} is practically zero given that standard deviation. It is important to recall that it is not appropriate to directly compare the acidic and basic components of asphalt. Each acidic or basic component should be compared to the reference solvent or with other asphalt's acidic or basic components because the scale of measurement is relative, not absolute. In fact, there is no absolute scale.

Aggregates

The universal sorption device (USD) was used to quantify the surface energy of the aggregates. This method consists of measuring the absorption of a particular gas solvent of known surface energy components through the surface of an aggregate. The aggregate size that is tested consists of particles that pass sieve No. 4 (4.75 mm) but are

retained on sieve No. 8 (2.36 mm). Three different types of gas solvents of known surface energy components must be used to measure the surface energy of the aggregates: n-Hexane (apolar), the monopolar Methyl Propyl Ketone (MPK), and distilled water (bipolar). The surface energies of these gas solvents are included in Table 30.

TABLE 30 Surface energy components of gas solvents

Solvent	Γ^{LW}	Γ^{+}	Γ^{-}	Γ^{AB}	Γ
n-hexane	18.4	0	0	0	18.4
MPK	24.7	0	19.6	0	24.7
Distilled Water	21.8	25.5	25.5	51	72.8

The Brunauer, Emmett and Teller theory (BET) is applied to calculate the specific surface area of the aggregate that corresponds to the surface area per unit mass of absorbent (30). Following this, the spreading pressure at saturation vapor pressure, π_e, is measured for each solvent. Having π_e plus the surface energies of the three gas solvents, the following equations can be solved in the following order to obtain the surface energy components of the aggregate (30):

$$\Gamma_s^{LW} = \frac{\left(\Pi_e + 2 \cdot \Gamma_l\right)^2}{4\Gamma_l^{LW}} \tag{46}$$

$$\Gamma_s^{+} = \frac{\left(\Pi_e + 2\Gamma_{lm} - \sqrt{\Gamma_s^{LW}\Gamma_{lm}^{LW}}\right)^2}{4\Gamma_{lm}^{-}} \tag{47}$$

$$\Gamma_s^{+} = \frac{\left(\Pi_e + 2\Gamma_{lb} - 2\sqrt{\Gamma_s^{LW}\Gamma_{lb}^{LW}} - 2\sqrt{\Gamma_s^{+}\Gamma_{lb}^{-}}\right)^2}{4\Gamma_{lb}^{+}} \tag{48}$$

$$\Gamma_s = \Gamma_x^{LW} + 2\sqrt{\Gamma^{+}\Gamma^{-}} \tag{49}$$

where

Γ_l = Surface energy of the apolar liquid (n-hexane),

Γ_{lm} = Surface energy of the monopolar liquid (MPK),

Γ_{lb} = Surface energy of the bipolar liquid (distilled water),

Γ_s = Total surface energy of the aggregate

The spreading pressures for the granite and the limestone and the specific surface areas that were obtained using the USD are presented in Tables 31 and 32 respectively.

TABLE 31 Spreading pressures and specific surface areas for SGC granite samples

Granite Sample #	n-hexane		MPK		water	
	Πe	SSA	Πe	SSA	Πe	SSA
1	30.25	0.12	39.42	0.47	125.34	0.88

TABLE 32 Spreading pressures and specific surface areas for SGC limestone samples

Limestone Sample #	n-hexane		MPK		water	
	Πe	SSA	Πe	SSA	Πe	SSA
1	43.89	0.2975	40.9	0.76	132.5	0.72
2			41.9	0.86	129.8	0.56
average :	43.89	0.2975	41.4	0.81	131.15	0.64

With these measurements the surface energy components of the aggregates are calculated as it was previously described and the results are shown in Table 33.

TABLE 33 Surface energy components of aggregates

AGGREGATE	Γ	Γ^{LW}	Γ^{AB}	Γ^{+}	Γ^{-}
Georgia Granite	218.63	61.08	157.55	31.86	194.78
Florida Limestone	223.77	88.46	135.30	24.76	184.87

Adhesive and Cohesive Bond Energies

The fatigue of HMA can be characterized by loss of adhesive bond strength or loss of cohesive bond strength. An adhesive fracture is characterized by loss of attraction between the molecules at the interface between the asphalt and the aggregate. When the fracture is cohesive, the cracks take place within the asphalt mastic itself. By knowing these cohesion and adhesion characteristics of the mix, it is possible to evaluate water susceptibility in terms of healing and fatigue cracking properties.

The adhesive surface energy corresponds to the creation of a unit crack area at the interface between the asphalt and the aggregate under a vacuum condition (13). In addition, the cohesive bond surface energy consists of the formation of a cohesive unit area formed by the combination of two asphalt pieces under a vacuum condition (13).
It is important to point out that an asphalt-aggregate combination is compatible when no water is present if the cohesive or the adhesive surface energies are positive; hence the lower magnitude of these two governs the mode of fracture. Therefore the ideal situation is to have a mix with high adhesive and cohesive surface energies. However, as mentioned previously, the adhesive surface energy should preferably have a larger acid-base component rather than with a large LW component because this improves healing in the presence of water.

The cohesive bond strength of the asphalt with and without the presence of water was calculated using Equations 35 and 40 respectively; Tables 34 and 35 include the calculated values. Figure 42 shows the difference between these two conditions. As can be seen, water increases the asphalt ability to heal (higher acid base component) and

reduces its resistance to fracture. This is because the hydrogen atoms in the water have good interaction or affinity with those of the AB component of the asphalt; hence, water makes the hydrogen bonds stronger and enhances the healing capability. This reinforces the fact that, it is beneficial to have a greater AB component and a low LW component. However, the bonding of these hydrogen atoms, takes time and therefore it is associated with the long term healing of the asphalt.

TABLE 34 Cohesive bond strength of asphalt without water

ASPHALT TYPE	Healing		Fracture
	ΔG_h^{LW}	ΔG_h^{AB}	ΔG_f
PG 67-22	43.36	1.80	90.5

TABLE 35 Cohesive bond strength of asphalt with water

ASPHALT TYPE	Healing		Fracture
	ΔG_h^{LW}	ΔG_h^{AB}	ΔG_f
PG 67-22	0.00	58.63	37.49

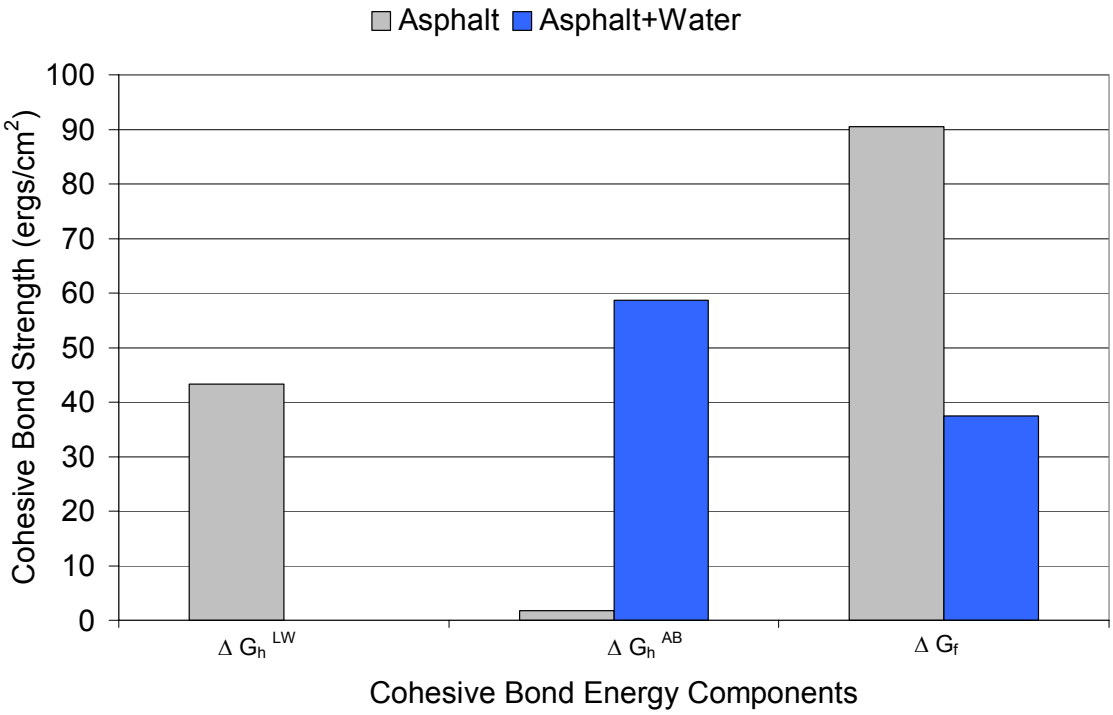

Figure 42 Cohesive bond strength of asphalt with and without water.

The calculated bond energies (ΔG) for fracture and healing in an adhesive fracture with and without the presence of water are summarized in Tables 36 and 37. These values were calculated using Equations 30 and 40 respectively.

TABLE 36 Adhesive bond strength without water (ergs/cm^2)

	Healing		Fracture
AGGREGATE/ASPHALT	ΔG_h^{LW}	ΔG_h^{AB}	ΔG_f
Granite & PG67-22	72.8	29.0	152.6
Limestone & PG67-22	87.6	26.1	168.4

TABLE 37 Adhesive bond strength with water (ergs/cm^2)

	Healing		Fracture
AGGREGATE/ASPHALT	ΔG_h^{LW}	ΔG_h^{AB}	ΔG_f
Granite & PG67-22	-0.08	-89.58	-72.0
Limestone & PG67-22	-0.12	-82.05	-60.7

Limestone has better resistance to fracture than granite under dry conditions as indicated by the higher fracture energy in Table 36. Also, it can be inferred from the bond strength energies that the limestone has better resistance to fracture when water is present because its energy components are less negative compared to the granite. On the other hand, when water is in the interface, the limestone has a better capability to heal because its acid-base component is less negative, thus there is less detachment of the asphalt from the aggregate, as it can be seen in Table 37.

These results are in accordance to the observations that were carried out on the specimens by Birgisson et al (2). When opening the core, they found that even though the limestone specimens did not exhibit much stripping, they were susceptible to moisture damage due to a reduced cohesion.

Summary

The moisture damage parameters that were selected to relate pore size distribution and pressure distribution were the energy ratio (ER) and the number of cycles to failure (N). These parameters were studied as a ratio that reflected the change from a wet to a dry condition. Therefore, the higher these ratios are the lesser damage takes place.

The specimens analyzed in this chapter consisted of limestone and granite specimens from the SGC mixtures that were prepared using corresponding gradations.

The air void distribution was calculated from the image analysis that registered the size of all pores within the specimens. The pore pressure distribution was calculated from a three dimensional fluid flow model for HMA under saturated conditions.

When comparing the granite and the limestone cores based on the ER, it was evident that the change in this parameter from a wet condition to a dry condition for granite mixtures was larger than for the limestone mixtures. This indicates that the granite mixes are more vulnerable to moisture damage than the limestone mixes. This ratio encompasses key mechanical properties (i.e. DCSE, tensile stress, creep compliance, m-value) that change with moisture. The trend was similar when the limestone and granite mixes were compared based on the N ratio.

The N and ER ratios showed that there is a "pessimum" air void size range for which the damage is higher. A similar idea of this qualification was first declared by Terrel et al. (28, 29) who found that there is a "pessimum" air void content for which the strength of a mix is worse than otherwise would be. The limestone cores displayed this same pattern of minimum performance. However, the ranges differ, being approximately from 1.2 to 1.4 mm for the granite cores, and from 0.8 to 1.0 mm for the limestone cores.

The pressure distribution was different within the specimens of each type of aggregate and between mixes with similar gradations but different types of aggregates. There was no meaningful relationship between the pressure distribution and these parameters. This was not surprising because the measurements associated with the determination of N and ER were conducted after pore pressure was released.

The universal sorption device (USD) and the Wilhelmy plate methods were used to measure the surface energies of the aggregates and the asphalt respectively. From these measurements the cohesive and adhesive bond strengths without and in the presence of water were calculated. According to the measurements and calculations, this asphalt has a better healing ability when water is present; however, its fracture energy is lower under this condition. Also, the granite is more susceptible to moisture damage as it has less ability to heal and is more prone to fracture than the limestone under wet conditions.

CHAPTER V

CONCLUSIONS

Conclusions

The current design methods of HMA include permanent deformation, low temperature cracking, and fatigue cracking. Moisture sensitivity is only considered to determine if the final design mixture is susceptible to damage due to the action of water. Moisture damage is directly related to permeability. In spite of the influence of moisture damage on stripping, excessive deflection, cracking and reduction of load carrying capacity, the mix microstructure characteristics and material properties that affect moisture damage are not directly considered.

X-ray CT was used to capture the microstructure and image analysis techniques were utilized to analyze the air void distribution. The use of X-ray CT image is considered a major improvement over previous studies that attempted to link the air void distribution of granular materials to permeability. X-ray CT enhanced the ability of obtaining continuous data about the air void distribution at the microstructure level. This was done in the past by analyzing discrete data using mercury intrusion techniques which might cause disturbance to the microstructure.

This study established the relationship between the air void size distribution and HMA permeability through the analysis of three sets of HMA specimens. These sets included laboratory specimens compacted using the linear kneading compactor,

laboratory specimens compacted using the Superpave™ gyratory compactor, and field cores. The influence of air void size distribution on permeability was established using the assumption that the probability of having two voids connected to each other on adjacent slices (X-ray CT images) is completely correlated. This assumption was adopted due to the small HMA slice thicknesses. The air void size distribution was considered to be Lognormal based on the Pearson correlation coefficient and probability plots that showed linearity between the data and the tested distribution.

There was a strong correlation between the air void size distribution and permeability for laboratory compacted specimens. However, weak correlation was found between air void distribution in field cores and permeability field measurements. This was attributed to the fact that in field permeability measurements, fluid tends to flow in the top one inch of a core due to the high percent of air voids in the top compared with the rest of the core. In other words, the measured field permeability is not associated with all air voids in the pavement. In fact, some field permeability measurements can be high while X-ray CT shows that there is no air void connectivity across the core. Therefore, it was decided to only include the cores that have connected voids in studying the correlation between air void distribution and field permeability. This step lead to significant improvement in correlation between air void distribution in field cores and permeability field measurements.

This study also related moisture damage to air void distribution and pore pressure distribution in HMA microstructure. The air void distribution was calculated from the image analysis that registered the size of all the air voids within the specimens.

The pore pressure distribution was calculated from a three dimensional fluid flow model for HMA under saturated conditions. The resistance of HMA to moisture damage was evaluated using two parameters that were derived based on fracture mechanics principles. These parameters are energy ratio (ER) and the number of cycles to failure (N). The ratio of the parameter determined under dry conditions to the same parameter under wet conditions was taken as indication of resistance to moisture damage. Therefore, the higher these ratios are the lesser damage takes place.

The moisture damage was assessed for limestone and granite specimens that were prepared using similar gradations. However, the gradation within each mix type was varied to obtain different air void distributions. The granite mixes had larger air voids than their limestone counterparts even though they were designed to have similar gradations.

When comparing the granite and the limestone cores based on the ER and N ratios, it was evident that the change in this parameter from a dry condition to a wet condition was larger for granite specimens than for the limestone specimens.

The N and ER ratios showed that there is a "pessimum" air void size range, for each of the granite and limestone mixes, where moisture damage is at maximum. However, the ranges differ, being approximately from 1.2 to 1.4 mm for the granite cores, and from 0.8 to 1.0 mm for the limestone cores. A similar idea of this qualification was first declared by Terrel et al. (28, 29), who found that there is a "pessimum" air void content for which the resistance to moisture damage is worst than

otherwise would be. The limestone cores displayed this same pattern of minimum performance.

The pressure distribution was different within specimens from each type of mix, and between mixes with similar gradations but different types of aggregates. There was no meaningful relationship between the pressure distribution and the moisture damage parameters. This was not surprising because after all, the measurements associated with the determination of N and ER, were conducted after pore pressure was released.

The moisture damage was also related to the chemical properties aggregates and binder. The universal sorption device (USD) and the Wilhelmy plate methods were used to measure the surface energies of the aggregates and the asphalt, respectively. From these measurements, the cohesive and adhesive bond strengths without and in the presence of water were calculated. According to the measurements and calculations, this asphalt has a better healing ability when water is present; however, its fracture energy is lower under this condition. Also, the granite is more susceptible to moisture damage as it has less ability to heal and is more prone to fracture than the limestone under wet conditions. The current asphalt mix design methods need to account for the cohesive and adhesive properties of asphalt mixtures that are highly affected by moisture.

REFERENCES

1. Al-Omari, A., L. Tashman, E. Masad, A. Cooley, and T. Harman. Proposed Methodology for Predicting HMA Permeability. *Journal of the Association of Asphalt Paving Technologists*, Vol. 71, 2002, pp. 30-58.

2. Birgisson, B., R. Roque, and G. Page. Evaluation of Water Damage Using Hot Mix Asphalt Fracture Mechanics. *Journal of the Association of Asphalt Paving Technologists*, Vol. 72, 2003, pp. 424-462.

3. Garcia-Bengochea, I. *The Relation between Permeability and Pore Size Distribution of Compacted Clayey Silts*. M.S. thesis. Purdue University, Lafayette, IN, 1978.

4. Terzaghi, K., R. Peck, and G. Mesri. *Soil Mechanics in Engineering Practice*. John Wiley & Sons, New York, 1996.

5. Bear, J. *Dynamics of Fluids in Porous Media*, American Elsevier Publishing Co., New York, 1972.

6. Scheidegger, A.E. *The Physics of Flow Through Porous Media,* University of Toronto Press, Toronto, Canada, 1957.

7. Childs, E.C., and N. Collis-George. The Permeability of Porous Materials. *Proc. Roy. Soc. Lond*., Vol. A201, 1950, pp. 392-405.

8. Marshall, T.J. A Relation between Permeability and Size Distribution of Pores. *J. Soil Sci.,* Vol. 9, No. 1, 1958, pp. 1-8.

9. Juang, C.H., and R.D. Holtz. A Probabilistic Permeability Model and the Pore Size Density Function. *International Journal for Numerical and Analytical Methods in Geomechanics*, Vol. 10, 1986, pp. 543-553.

10. Al-Omari, A., and E. Masad. Three Dimensional Simulation of Fluid Flow in X-ray CT Images of Porous Media. *International Journal for Numerical and Analytical Methods in Geomechanics*, Vol. 28, Issue 13, 2004, pp. 1327-1360.

11. Roberts, F., P. Kandhal, E. Brown, D. Lee, and T. Kennedy. *Hot Mix Asphalt Materials, Mixture Design and Construction*. NAPA Educational Foundation, Lanham, Maryland, 1996.

12. Barksdale, R. *The Aggregate Handbook*. National Stone, Sand and Gravel Association, Arlington, VA., 2001.

13. Lytton, R. "Adhesive Fracture in Asphalt Concrete Mixtures", 2004. http://ceprofs.tamu.edu/lytton/ADHESIVE%20FRACTURE%20IN%20ASPHALT%20CONCRETE%20MIXTURES.doc.

14. E.W. Washburn. Note on a Method of Determining the Distribution of Pore Sizes in a Porous Material, *Proc.Nat.Acad.Sci.*, Vol. 7, 1921, pp. 115-116.

15. Masad, E., V. K. Jandhyala, J. Dasgupta, N. Somadevan, and N. Shashidhar. Characterization of Air Void Distribution in Asphalt Mixes Using X-Ray CT. *Journal of Materials in Civil Engineering*, ASCE, Vol. 14, No. 2, 2002, pp. 122-129.

16. ASTM D 5084-00 Standard Test Methods for Measurement of Hydraulic Conductivity of Saturated Porous Materials Using a Flexible Wall Permeameter. ASTM International, West Conshohocken, PA, 2002.

17. Birgisson, B., R. Roque, and G. Page. The Use of a Performance-Based Fracture Criterion for the Evaluation of Moisture Susceptibility in Hot Mix Asphalt. *Presented at*

the 83rd Annual Meeting of the Transportation Research Board, Washington, DC, Jan. 11-15, 2004, [available on CD].

18. *Image Pro Plus*, Version, 4.1, Media Cybernetics, L.P, Georgia, MD (1999).

19. *SPSS for Windows - Release 10.0.7.* SPSS Inc. Business Intelligence Division, Chicago, IL, 2002.

20. *Minitab Release 13.1.* BCIS Lab, St. Cloud, MN, 2000.

21. *Maple 9.01.* Waterloo Maple Inc., Waterloo, Canada, 2003.

22. ASTM D 2434-68 Standard Test Method for Permeability of Granular Soils (Constant Head) ASTM International. West Conshohocken, PA, 2000.

23. Lavin, P. *Asphalt Pavements.* Spon Press, New York, 2003.

24. Zhang, Z., R. Roque, B. Birgisson, and B. Sangpetngam. Identification and Verification of a Suitable Crack Growth Law for Asphalt Mixtures. *Journal of the Association of Asphalt Paving Technologists (Symposium),* Vol. 70, 2001, pp. 206-241.

25. Jajliardo, A. *Development of Specification Criteria to Mitigate Top-Down Cracking*. M.S. thesis. University of Florida, Gainesville, 2003.

26. Masad, E., S. Saadeh, T. Al-Rousan, E. Garboczi, and D. Little. Computations Of Particle Surface Characteristics Using Optical and X-Ray CT Images. *Journal of Computational Geosciences*, 2004, (in press).

27. Chandan, C., K. Sivakumar, T. Fletcher, and E. Masad. Geometry Analysis of Aggregate Particles Using Imaging Techniques. *Journal of Computing in Civil Engineering, ASCE*. Vol. 18, No. 1, 2002, pp. 75-82.

28. Terrel, R. and S. Al-Swailmi. Role of Pessimum Voids Concept in Understanding Moisture Damage to Asphalt Concrete Mixtures. In *Transportation Research Record 1386,* TRB, National Research Council, Washington, DC, 1993, pp.31-37.

29. Terrel, R., and S. Al-Sqailmi. Evaluation of Water Damage of Asphalt Concrete Mixtures Using the Environmental Conditioning System (ECS). *Journal of the Association of Asphalt Paving Technologists (Symposium)*, Vol. 61, 1992, pp. 405-445.

30. Cheng, D., D. Little, R. Lytton, and J. Holste. Use of Surface Free Energy Properties of the Asphalt- Aggregate System to Predict Moisture Damage Potential. *Journal of the Association of Asphalt Paving Technologists*. Vol. 71, 2002, pp. 59-88

31. Della Volpe, C., and S. Siboni. Calculations of Acid-Base Surface Tension Components. Trento, Italy. http://devilmac.ing.unitn.it:8080/

APPENDIX A

TABLE 38 Gradation of granite mixes

Sieve Size	Granite Specimens: Percent Passing					
	GA-C1	GA-C2	GA-C3	GA-F1	GA-F2	GA-F3
19 mm (3/4)	100.0	100.0	100.0	100.0	100.0	100.0
12.5 mm (1/2)	97.4	90.9	97.3	94.7	90.5	94.6
9.5 mm (3/8)	89.0	72.9	89.5	84.0	77.4	85.1
4.75 mm (#4)	55.5	45.9	55.4	66.4	60.3	65.1
2.36 mm (#8)	29.6	28.1	33.9	49.2	43.2	34.8
1.18 mm (#16)	19.2	18.9	23.0	32.7	34.0	26.0
600 mm (#30)	13.3	13.2	16.0	21.0	23.0	18.1
300 mm (#30)	9.3	9.2	11.2	12.9	15.3	12.5
150 mm (#100)	5.4	5.6	6.8	5.9	8.7	7.7
75 mm (#200)	3.5	3.9	4.7	3.3	5.4	5.8

TABLE 39 Gradation of limestone mixes

Sieve Size	Limestone Specimens: Percent Passing					
	WR-C1	WR-C2	WR-C3	WR-F1	WR-F2	WR-F3/C4
19 mm (3/4)	100.0	100.0	100.0	100.0	100.0	100.0
12.5 mm (1/2)	97.0	91.0	98.0	96.0	91.0	95.0
9.5 mm (3/8)	90.0	74.0	89.0	85.0	78.0	85.0
4.75 mm (#4)	60.0	47.0	57.0	69.0	61.0	67.0
2.36 mm (#8)	33.0	30.0	36.0	53.0	44.0	37.0
1.18 mm (#16)	20.0	20.0	24.0	34.0	35.0	26.0
600 mm (#30)	15.0	14.0	18.0	23.0	24.0	20.0
300 mm (#30)	11.0	10.0	13.0	15.0	16.0	14.0
150 mm (#100)	7.6	6.7	9.2	9.6	9.1	8.6
75 mm (#200)	4.8	4.8	6.3	4.8	6.3	5.8

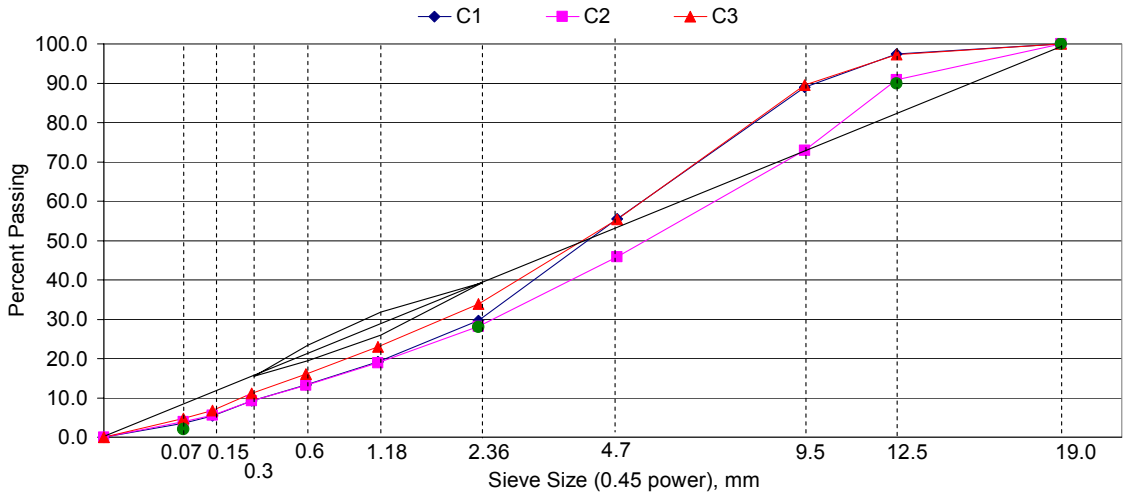

Figure 43 Granite Coarse Gradation Mixes, NMAS=12.5 mm.

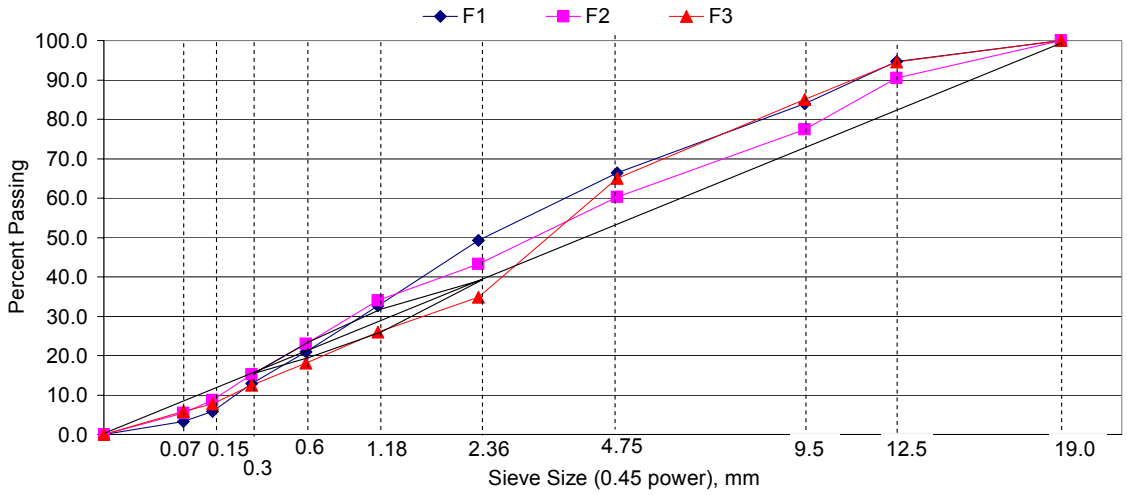

Figure 44 Granite fine gradation mixes, NMAS=12.5 mm.

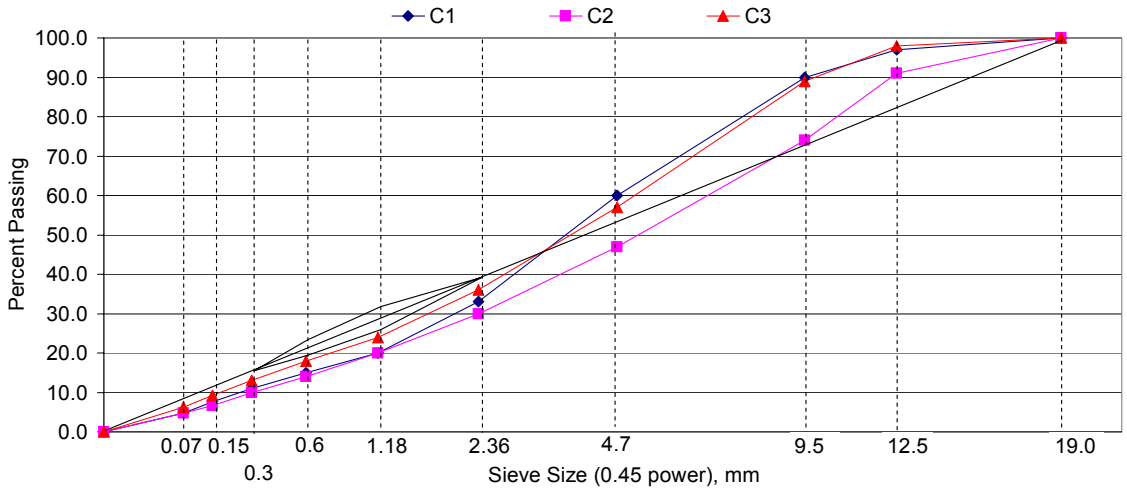

Figure 45 Limestone coarse gradation mixes, NMAS=12.5 mm.

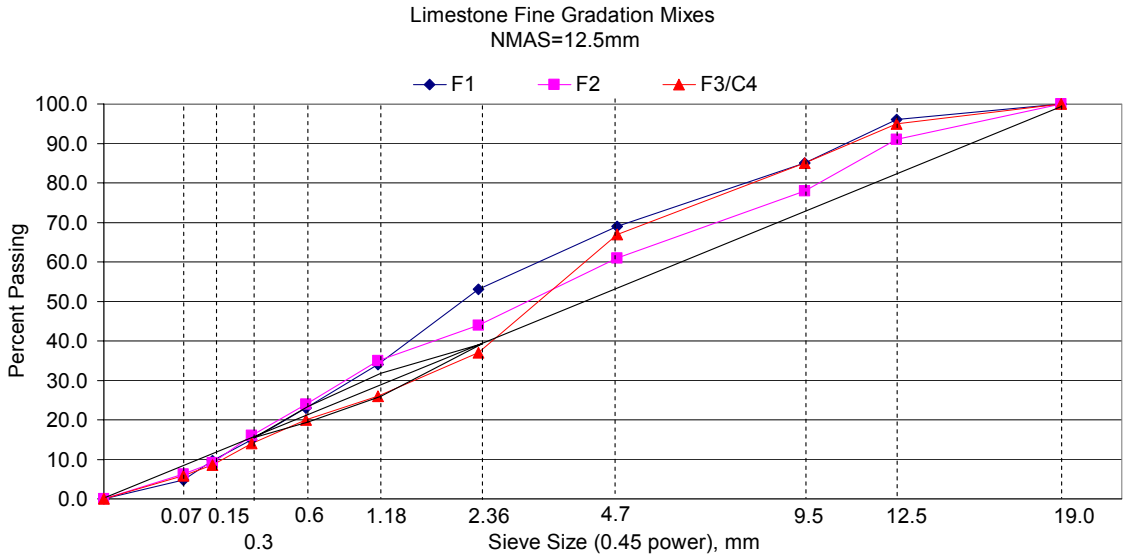

Figure 46 Limestone fine gradation mixes, NMAS=12.5 mm.

VITA

Adhara Castelblanco Torres was born in Bogotá, Colombia, in 1977. She received her Bachelor of Science degree in civil engineering from Universidad Nacional de Colombia in April 2002. In the fall of 2002, she started her master's degree at Texas A&M University, and she graduated in December 2004, with a Master of Science in civil engineering. She can be contacted at the following address:

8708 Duncanson Dr.

Bakersfield, CA 93309